

Magnetic particles at fluid-fluid interfaces : microrheology, interaction and wetting

Citation for published version (APA):

Cappelli, S. (2016). *Magnetic particles at fluid-fluid interfaces : microrheology, interaction and wetting*. [Phd Thesis 1 (Research TU/e / Graduation TU/e), Biomedical Engineering]. Technische Universiteit Eindhoven.

Document status and date:

Published: 28/09/2016

Document Version:

Publisher's PDF, also known as Version of Record (includes final page, issue and volume numbers)

Please check the document version of this publication:

- A submitted manuscript is the version of the article upon submission and before peer-review. There can be important differences between the submitted version and the official published version of record. People interested in the research are advised to contact the author for the final version of the publication, or visit the DOI to the publisher's website.
- The final author version and the galley proof are versions of the publication after peer review.
- The final published version features the final layout of the paper including the volume, issue and page numbers.

[Link to publication](#)

General rights

Copyright and moral rights for the publications made accessible in the public portal are retained by the authors and/or other copyright owners and it is a condition of accessing publications that users recognise and abide by the legal requirements associated with these rights.

- Users may download and print one copy of any publication from the public portal for the purpose of private study or research.
- You may not further distribute the material or use it for any profit-making activity or commercial gain
- You may freely distribute the URL identifying the publication in the public portal.

If the publication is distributed under the terms of Article 25fa of the Dutch Copyright Act, indicated by the "Taverne" license above, please follow below link for the End User Agreement:

www.tue.nl/taverne

Take down policy

If you believe that this document breaches copyright please contact us at:

openaccess@tue.nl

providing details and we will investigate your claim.

Magnetic particles at fluid-fluid interfaces: microrheology, interaction and wetting

PROEFSCHRIFT

ter verkrijging van de graad van doctor aan de Technische Universiteit Eindhoven, op gezag van de rector magnificus prof.dr.ir. F.P.T. Baaijens, voor een commissie aangewezen door het College voor Promoties, in het openbaar te verdedigen op woensdag 28 september 2016 om 16:00 uur

door

Stefano Cappelli

geboren te Ravenna, Italië

Dit proefschrift is goedgekeurd door de promotoren en de samenstelling van de promotiecommissie is als volgt:

voorzitter: prof.dr.ir. G.M.W. Kroesen
promotor: prof.dr.ir. M.W.J. Prins
copromotor(en): dr.ir. A.M. de Jong
 prof.dr. J.D.R. Harting
leden: prof.dr.ir. J. van der Gucht (Wageningen Universiteit)
 dr. J. Baudry (ESPCI ParisTech)
 dr.ir. I.K. Voets

Het onderzoek of ontwerp dat in dit proefschrift wordt beschreven is uitgevoerd in overeenstemming met de TU/e Gedragscode Wetenschapsbeoefening.

The work described in this thesis was performed in the Faculty of Applied Physics of the Eindhoven University of Technology and was financially supported by the European Commission's Seventh Framework Programme (FP7/2007-2013) under the grant agreement BIOMAX (project n° 264737).



© Stefano Cappelli, 2016

Magnetic particles at fluid-fluid interfaces: microrheology, interaction and wetting
Author: Stefano Cappelli - Eindhoven University of Technology, 2016.

A catalogue record is available from the Eindhoven University of Technology Library
ISBN: 978-90-386-4134-8

Typeset using \LaTeX , printed by Gildeprint, Enschede, The Netherlands.



Summary

Magnetic particles at fluid-fluid interfaces: microrheology, interaction and wetting

The interaction between particles and fluid-fluid interfaces is important for the field of lab-on-a-chip biosensing, where particles are used for their large surface-to-volume ratio, flexible bio-functionalization, stability, and for their actuation and detection properties. In addition, the strong adsorption of colloidal particles to fluid-fluid interfaces is being used in a wide range of applications, including food technology, energy and material science. Therefore, it is important to understand and to control the physics that governs these interactions.

The focus of this PhD thesis is on the study of the interaction of particles with fluid-fluid interfaces, with the general goal to develop new methodologies for interface characterization. In particular, we focus on the use of magnetic tweezers experiments to study the microrheology of interfaces, the interactions between particles adsorbed at the interface, and the dynamic wetting of single particles.

In Chapter one, we highlight the role of fluid-fluid interfaces across disciplines, providing relevant examples and focusing on the current technological and fundamental open challenges. In Chapter two, we describe the physics, we review the current techniques to study the adsorption and the equilibrium contact angle of particles at fluid interfaces, and we review the available experimental and numerical techniques to study dynamic wetting on single particles.

In Chapter three, we describe a new interfacial rheometry technique based on pairs of micrometer-sized magnetic particles at a fluid-fluid interface. The particles are repeatedly attracted and repelled by well-controlled magnetic dipole-dipole forces, so-called interfacial rheometry by Intra-Pair Magnetophoresis (IPM). We apply IPM to study the time-dependent adsorption of an oil-soluble amino-modified silicone polymer at a water-oil interface using carboxylated magnetic particles. Results show an increase of interfacial drag of particles over several orders of magnitude, which is highly sensitive to the polymer concentration and to the ionic strength of the aqueous phase. The fast measurement time over very long timescales make IPM a versatile method to study interfacial viscosity in a wide variety of soft-matter materials systems.

In Chapter four, we study the capillary attraction of micrometer-sized particles at a water-oil interface. Capillary attractions originate from the overlap of local deformations

of the interface due to the pinning of the three-phase contact line to local heterogeneities on the surface of the particles. We studied the time-dependence of the capillary attraction in a system with very strong interfacial aging, namely a system wherein a polymer adsorbs to a water-oil interface and modulates the interfacial viscosity by several orders of magnitude. We demonstrate that the capillary attraction varies strongly per particle pair, but for a given particle pair, interestingly the capillary attraction does not depend on time or on the magnitude of the interfacial viscosity. This leads to the conclusion that although the polymer has a very strong influence on the interfacial viscosity, the polymer does not modify the capillary attraction of particles at the oil-water interface.

In Chapter five, we address the problem of dynamic wetting and we propose a new method where magnetic particles trapped at a fluid interface are interrogated with different magnetic torques. We demonstrate that particles trapped at an aqueous two-phase interface show different wetting patterns as a result of the interaction of the three-phase contact line with the particle surface. Finally, we conclude with a summary of the scientific and technological achievements described in this thesis and we put our methodology into the perspective of answering still open questions. We foresee that the methods developed in this thesis will help scientists and engineers from diverse disciplines to tackle problems and develop new applications.

Contents

Summary	iii
1 Introduction	1
1.1 Particles at fluid-fluid interfaces	2
1.1.1 Wetting in nature and technology	2
1.1.2 Colloidal particles	4
1.2 Overview of technological & fundamental challenges	8
1.2.1 Interfacial microrheology	8
1.2.2 Capillary interactions	9
1.2.3 Dynamic wetting	10
1.3 This thesis	10
2 Basic concepts of particles at fluid-fluid interfaces	13
2.1 Introduction	14
2.2 Contact angle on planar substrates	16
2.2.1 Static contact angle	16
2.2.2 Experimental techniques	17
2.2.3 Numerical techniques	18
2.2.4 Contact angle hysteresis	18
2.2.5 Dynamic contact angle	18
2.2.6 Hydrodynamic theory	20
2.2.7 Molecular kinetic theory	20
2.2.8 Comparison with experiments	20
2.3 Interaction of particles with fluid-fluid interfaces	21
2.3.1 Diffusion of a particle in proximity of a fluid interface	21
2.3.2 Electrostatic interaction	22
2.3.3 Interfacial forces	23
2.3.4 Inter-particle interactions	24
2.4 Particles at fluid-fluid interfaces: static contact angle	26
2.4.1 Experimental techniques for measuring the contact angle of particles at fluid interfaces	27
2.4.2 Numerical techniques to simulate particles in the vicinity of fluid interfaces	29

2.5	Particles at fluid-fluid interfaces: dynamic wetting	30
2.5.1	Experimental techniques	30
2.5.2	Numerical techniques	33
2.6	Conclusions	34
3	Interfacial rheometry of polymer at a water-oil interface by intra-pair magnetophoresis	37
3.1	Introduction	38
3.2	Materials and methods	39
3.2.1	Materials	39
3.2.2	Positioning of the particles at the interface	41
3.2.3	Particle tracking	41
3.2.4	Interfacial rheometry by Intra-Pair Magnetophoresis (IPM)	41
3.2.5	Interfacial rheometry by Mean-Squared Displacement (MSD)	43
3.3	Results	43
3.3.1	Drag measurements in water	43
3.3.2	Particle position as a function of polymer concentration	44
3.3.3	Drag measurements at a water-oil interface	45
	Low and high polymer concentrations.	45
	Intermediate polymer concentrations – high ionic strength.	45
	Intermediate polymer concentrations – low ionic strength.	47
3.4	Discussion	48
3.4.1	Rheometry by Intra-Pair Magnetophoresis	48
3.4.2	Particle position as a function of polymer concentration	51
3.4.3	Adsorption of polymers to the interface	52
3.5	Conclusions	54
	Appendices	55
3.A	Design of the fluid cell	55
3.B	Comparison between attraction and repulsion curves of Intra-Pair Magnetophoresis experiments	55
3.C	Comparison between Intra-Pair Magnetophoresis and Brownian motion experiments	56
3.D	Interfacial concentration of polymers at a water-oil interface	59
3.E	Interface ageing	61
4	Inter-particle capillary forces at a fluid-fluid interface with strong polymer-induced ageing	63
4.1	Introduction	64
4.2	Materials and methods	65
4.2.1	Materials	65
4.2.2	Quantification of particle drag coefficients and attractive capillary interactions at a water-oil interface	67
4.2.3	Numerical methods	68

4.3	Results	69
4.3.1	Measurements of colloidal attractive interactions	69
4.3.2	Brownian dynamics (BD) simulations of capillary attraction	70
4.3.3	Ageing of the interface due to the presence of polymer	72
4.3.4	Quantification of colloidal attractive force	73
4.4	Discussion	73
4.4.1	Interpretation of capillary attraction curves	74
4.4.2	Capillary attraction as a function of interface ageing	75
4.5	Conclusions	77
Appendices		79
4.A	Validation of Brownian Dynamics (BD) simulations	79
4.B	Analysis of BD simulations of particle attraction trajectories	80
4.C	Quantification of drag coefficient in the presence of attractive capillary interaction	84
4.D	Iterative quantification of f and F_0	86
4.E	Contact angle measurement of particles using z-stack of images	86
5	Dynamic wetting of single particles at fluid-fluid interfaces	91
5.1	Introduction	92
5.2	Materials and methods	94
5.2.1	Preparation of fluid-fluid interfaces	94
5.2.2	Particle functionalization	94
5.2.3	Out-of-plane rotation of particles	95
5.2.4	Experiments	97
5.3	Results	98
5.3.1	Water-decane interface	98
5.3.2	Aqueous two-phase system	99
5.4	Discussion	100
5.4.1	Torque required to deform a fluid-fluid interface	102
5.4.2	Dissipative contributions to the rotation of a particle at a fluid-fluid interface	103
5.4.3	Interpretation and discussion	106
5.5	Conclusions	108
6	Conclusions and Outlook	111
6.1	Introduction	111
6.2	Phenomena investigated using magnetic particles at fluid-fluid interfaces	112
6.2.1	Interfacial micro-rheometry	112
6.2.2	Inter-particle capillary interactions	113
6.2.3	Dynamic wetting of single particles	114
6.3	Future work	115
Bibliography		117

Publications	131
Curriculum Vitae	133
Acknowledgements	135



1

Introduction

Fluid-fluid interfaces and wetting phenomena are of great theoretical interest and play an important role in many technologies. The model description of such systems requires the knowledge from several disciplines, such as chemistry, physics, and engineering. From the seminal work of Thomas Young in 1805 several theories and experimental methods have been developed. However, an understanding of the fundamental processes at the molecular level is still lacking. An attractive alternative is to study particles at fluid-fluid interfaces, where small scale effects are dominant and quantitatively observable. In this Chapter we begin a journey across fluid-fluid interfaces by discussing the relevance of wetting phenomena and colloidal particles at fluid-fluid interfaces across disciplines. In the second part of this Chapter we focus our discussion on three aspects that are of technological and fundamental importance: microrheology, capillary interactions and dynamic wetting, with emphasis on still open challenges. Finally, we formulate the main research question and introduce the chapters of this thesis.

1.1 Particles at fluid-fluid interfaces

1.1.1 Wetting in nature and technology

Wetting phenomena are ubiquitous in nature and play a fundamental role in everyone's life. Plants use capillary action to bring water from the soil up the roots and stems to the rest of the plant. Lotus leaves have a *self-cleaning* ability that allows water droplets to roll off from their surface, so to prevent them to interfere with photosynthesis.¹ Desert beetles use their bumpy back to gather and condense water from fog.² These natural phenomena have inspired scientists to study and develop new technological processes based on wetting effects, such as for oil recovery, impregnation of textiles, drainage of water from highways, inkjet printing,^{3,4} cleaning, painting, detergency, lubrication,^{2,5} food technology,⁶⁻⁹ cosmetics and personal care,¹⁰ lithography technologies,¹¹ microfluidics and biomedical applications,¹² to cite a few.

Wetting can be defined as the ability of a liquid to maintain contact with a solid substrate.^{13,14} The degree of wetting and wettability is determined by the force balance of the intermolecular interactions between the fluid and the substrate. Molecules in a fluid are held together by cohesive forces, such as hydrogen bonds between polar molecules (e.g. water) or van der Waals forces between non-polar molecules (e.g. most oils). The cohesion energy per molecule in bulk fluid is U , while at a surface a molecule finds itself shortly of roughly $U/2$. The surface tension is a direct measure of this energy shortfall per unit surface area, which results in an inward force that holds the fluid molecules together.¹⁵ The balance between the cohesive and adhesive forces between the molecules of the fluids and the molecules of the surface was described for the first time in 1805 by Thomas Young,¹⁶ who related the surface tension of the three phases – water, air, solid – to the angle of contact at the boundary conditions (Fig. 1.1a). After more than two hundred years, the contact angle is still the first method to characterize the wettability of surfaces.^{3,14,15}

There are several strategies to modify the contact angle between a fluid and a surface. A first strategy involves the modification of the topological structure of the surface at the micro- or nano-scale (Fig. 1.1b). This strategy was inspired by naturally occurring micro-structures found in plants and animals^{1,13,19} and was used to create both superhydrophobic substrates for self-cleaning applications,⁵ as well as extreme wetting surfaces for biomedical applications.² A second strategy involves a chemical modification of the substrate or the deposition of low energy materials (Fig. 1.1c). A method to increase the surface energy of a substrate – hence increase its hydrophilicity – is to create polar groups at the surface, e.g. by using a plasma treatment in air or oxygen.¹⁷ Methods to decrease the surface energy of a substrate – hence increase its hydrophobicity – involves the silanization of a glass substrate, or the deposition of low surface tension materials such as polydimethylsiloxane (PDMS) or Teflon®.⁵ A third strategy involves the modification of the interface composition, such as with the addition of amphiphilic molecules (Fig. 1.1d).¹⁸

Amphiphilic molecules are characterized by a hydrophilic part and a hydrophobic part.¹⁸ The hydrophilic part, or the "headgroup", is water soluble and can carry a charge,

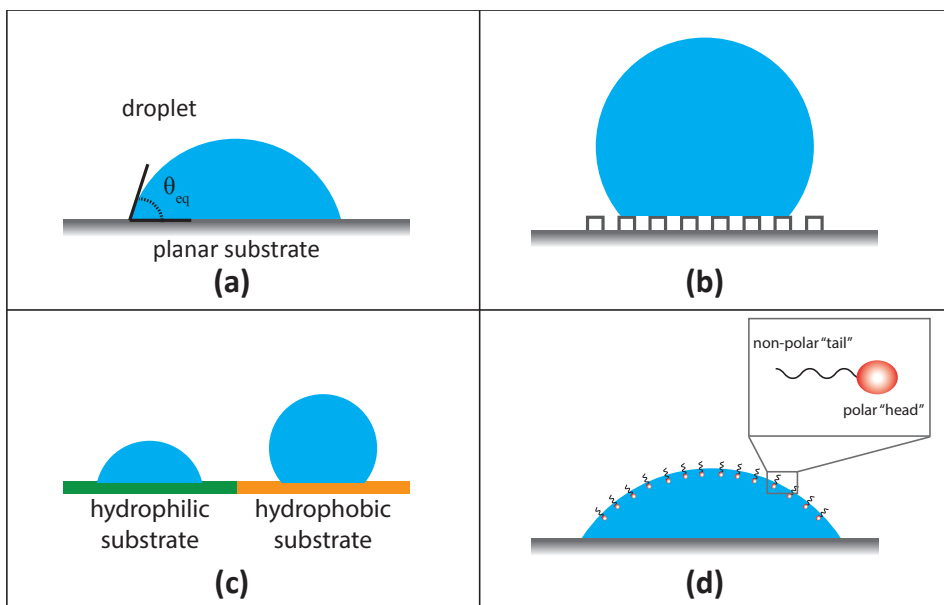


Figure 1.1: (a) A fluid droplet on a planar substrate is characterized by the contact angle θ_{eq} .¹⁶ The contact angle can be modified by changing (b) the substrate topography,^{2,5} (c) the surface chemistry,^{5,17} or (d) by adding amphiphilic molecules, e.g. surfactants, at the interface.¹⁸

as for ionic surfactants and phospholipids, or can be neutral, as for non-ionic surfactants. The hydrophobic part, or "tail", usually consists of one or two hydrocarbon chain(s).¹⁸ Due to the amphiphilic nature of these molecules, the adsorption to a fluid interface results in a gain of free energy, as the molecule orients itself to expose the hydrophilic part to the polar phase (e.g. water) and the hydrophobic part to the non-polar phase (e.g. air or oil) (see Fig. 1.1d). Amphiphilic molecules are essential in many industrial processes and find applications in cleaning, detergency,³ as emulsifiers for creams in the cosmetic and pharmaceutical industry,^{4,10} coating technologies,²⁰ and food technologies.⁹ As an example, emulsions can be in the form of oil drops in water or water drops in oil, and can be created when mechanical work is put into the system to create the extra surface (see Chapter 2). To prevent the inverse process, i.e. coalescing, the drops need to be stabilized. A strategy is to use surfactants which in turn decrease the surface tension and increase the steric hindrances and/or the electrostatic repulsion between the droplets.⁹ Most of these applications require the use of biodegradable and bio-compatible materials. Surfactants are very reactive species and may damage water quality when released into the natural environment, or may be toxic when in contact with humans.²¹ Therefore, their use is becoming more and more restricted (e.g. see the European Regulation (EC) No 648/2004 on detergents) and alternatives are strongly encouraged. Alternatives include the use of proteins,²² bio-compatible polymers²³ and colloidal particles.^{18,24} The latter approach is of particular interest. The use of colloidal particles at fluid-fluid interfaces helped scientists to overcome several technological challenges in a broad range of disciplines, and also has

led to an important field of research focused on the fundamental problems of soft matter. In the next section, we will outline the relevance and the broad applicability of colloidal particles at fluid-fluid interfaces.^{24–26}

1.1.2 Colloidal particles

The use of colloidal particles at fluid-fluid interfaces was pioneered in the early 20th century by the work of Ramsden²⁷ and Pickering.²⁸ The authors independently demonstrated that colloidal particles can be used to stabilize emulsions. The particles adsorb to the fluid interface and create a mechanical barrier that prevents the emulsion droplets to coalesce. Although Pickering acknowledged Ramsden in his seminal work, this kind of emulsions have been named after Pickering. The scientific and technological interest towards Pickering emulsions has increased since then, particularly for food and cosmetic technologies. Rayner *et al.* performed a search among the scientific literature using the query "Pickering emulsion" and "particle stabilized emulsions", which resulted in more than 5500 items with most of the results included in the last two decades.²² Part of this success

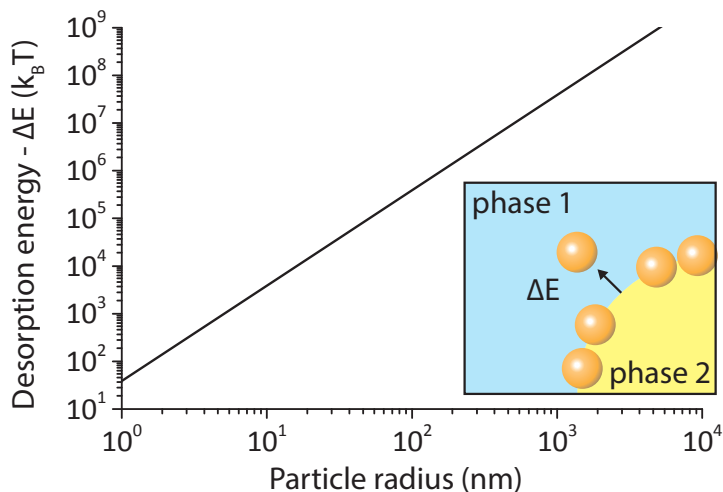


Figure 1.2: Energy required to remove a single spherical particle from a fluid-fluid interface. Calculations are performed according to eqn (2.19) of Chapter 2 as a function of particle radius and using a contact angle $\theta = 90^\circ$ and interfacial tension $\gamma = 50$ mN/m (e.g. water-decane interface). (Figure after²²).

originates from the *strong affinity of colloidal particles to fluid-fluid interfaces*.^{18,24,29} In 1980 Pieranski³⁰ described the thermodynamics of adsorption of a spherical particle to a fluid-fluid interface, with the adsorption energy depending on the surface tension of the interface, the particle radius and the particle wettability by the fluids. For a 10 nm particle the depth of the potential well is already several orders of magnitude greater than the thermal energy $k_B T$, so that particle adsorption is considered to be irreversible (see Fig. 1.2). This explains the high effectiveness of colloidal particles to stabilize emulsions as compared to the use of low molecular weight surfactants.

The use of colloidal particles in combination with fluid-fluid interfaces is not limited to food and cosmetic technologies. Applications have been developed in a broad range of fields including material science,^{11,31,32} renewable energies,³³ and biomedicine.^{12,34,35}

The strong confinement of the particle motion in the plane of the interface can be exploited for the production of materials with novel optical, thermal, electrical and/or mechanical properties. The interface represents an ideal plane where micro- and nanoparticles can laterally diffuse and self-organize into 2D ordered structures,^{31,36} where the properties on macroscopic length scales depend on the materials, the shape, and the spatial dimensions between the particles. The resulting assembly is the direct result of inter-particle interactions and it can then be deposited on solid substrates for surface patterning.¹¹ The presence of the interface creates an asymmetric distribution of charges on the particle surface, which is not fully captured by common theories of colloidal stability, like the Derjaguin-Landau-Verwey-Overbeek (DLVO) theory.³⁷ The resulting electric dipole is responsible for long ranged electrostatic forces extending over tens of micrometers, thus allowing to assemble particles on a large scale.^{29,36,38–40} Another class of interactions that can be used to change the structure of the particle self-assembly are capillary interactions, which originates from the superposition of deformations of the fluid interface. As an example, the lattice structure of the particle assembly can be tuned by tailoring the curvature of the interface, as shown in Fig. 1.3a.⁴¹ Another strategy is to use external fields, such as electric or magnetic fields.⁴² In Fig. 1.3b we show our results of an assembly of superparamagnetic particles at a water-oil interface in the presence of an external magnetic field. The field is oriented normally to the plane of the interface and modulates the magnetic dipole-dipole interaction between the particles, hence the inter-particle spacing. In the absence of the field, particles self-assemble with an irregular pattern as the result of capillary interactions. This will be further discussed in Chapter 4.

The interaction between particles and fluid interfaces is also important for the field of lab-on-a-chip biosensing.¹² A biosensor is a device that is able to detect molecular biomarkers from body fluids, such as blood, saliva and urine, and to generate a readable signal which is then used as indicator of the presence or severity of a disease (see Fig. 1.4a). Magnetic particles are well-suited for the capture of biomarkers from biological samples due to their large surface-to-volume ratio, the availability of many bio-functionalization options, and stability. Moreover, magnetic particles can be conveniently manipulated with external magnetic fields without interfering with organic biological materials, thereby simplifying extraction and buffer replacement steps. In order to be suited for point-of-care testing, a biosensor needs to perform a series of complex operations, involving binding, washing and eluting steps (see Fig. 1.4b), in which microfluidics plays an important role.

As a relevant example for this thesis, we present the microfluidic device developed by den Dulk *et al.*,⁴³ where magnetic particles are transported through stationary fluids by using magnetic forces (see Fig. 1.4b,c). Fluids are confined between two planar surfaces by capillary forces using a specific pattern of hydrophilic and hydrophobic regions. The chambers are separated by a medium that does not mix with the aqueous fluids, for example a non-polar fluid or a gas. Magnetic particles are dispersed in the first chamber and magnetic forces are used to pull the particles out of the fluid through the interface

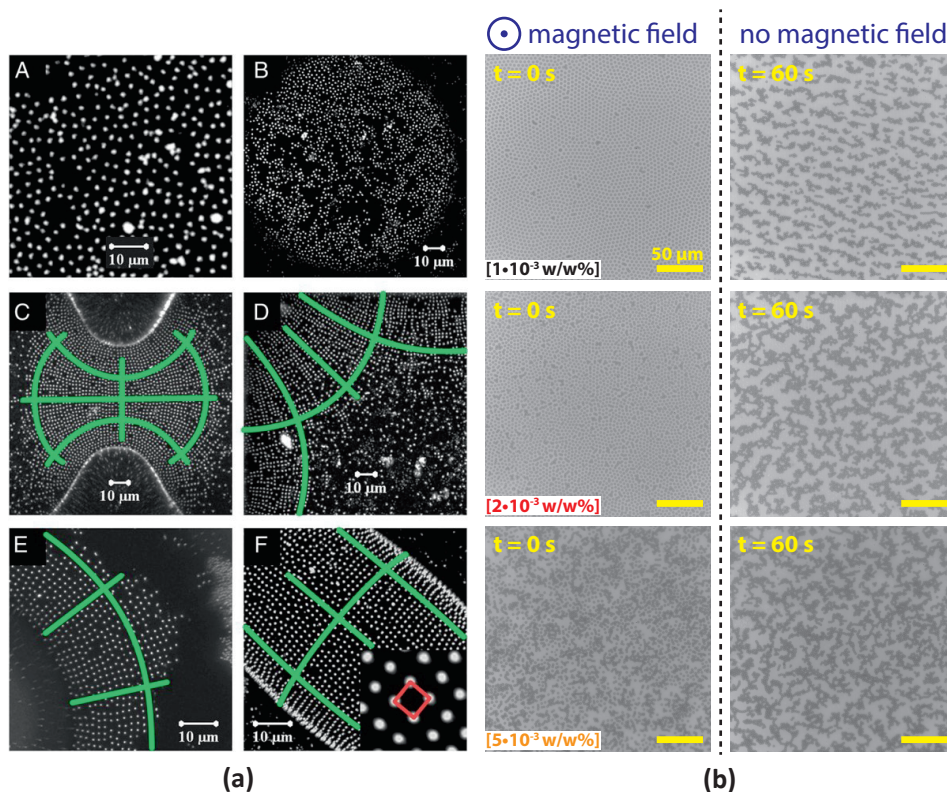


Figure 1.3: Examples of particle self-assembly at fluid-fluid interfaces. (a) The lattice structure can be controlled by introducing curvature gradients of the interface.⁴¹ (b) self assembly of superparamagnetic particles at a water-oil interface with and without an external magnetic field. This model system is described in Chapter 4. (a) reprinted from ref.,⁴¹ with permission from the Proceedings of the National Academy of Science of the United States of America.

of the fluid and the medium; thereafter, the particles are pulled into the second chamber through the interface of the medium and the fluid. This mechanism can be referred to as Magneto-Capillary Particle Transfer (MCPT)¹² and has been successfully applied for the purification and enrichment of nucleic acids and proteins.⁴³ During the process of particle extraction, several wetting phenomena occur (see Fig. 1.4 (i), (ii), (iii)). In the following we outline three aspects that are both of technological and fundamental relevance.

(i) *Adsorption of macromolecules to fluid-fluid interfaces.* The fluids used for biosensing applications are usually a mixture of buffers and biological fluids, and many surface active macromolecules – e.g. surfactants, polyelectrolytes and proteins – are present. Due to their amphiphilic nature, these macromolecules have a tendency to populate the interface. The time-dependent interfacial concentration depends on several factors, such as charge, molecular structure, bulk concentration, and the amount of already adsorbed species at the interface.⁴⁴ Moreover, upon adsorption macromolecules might change their

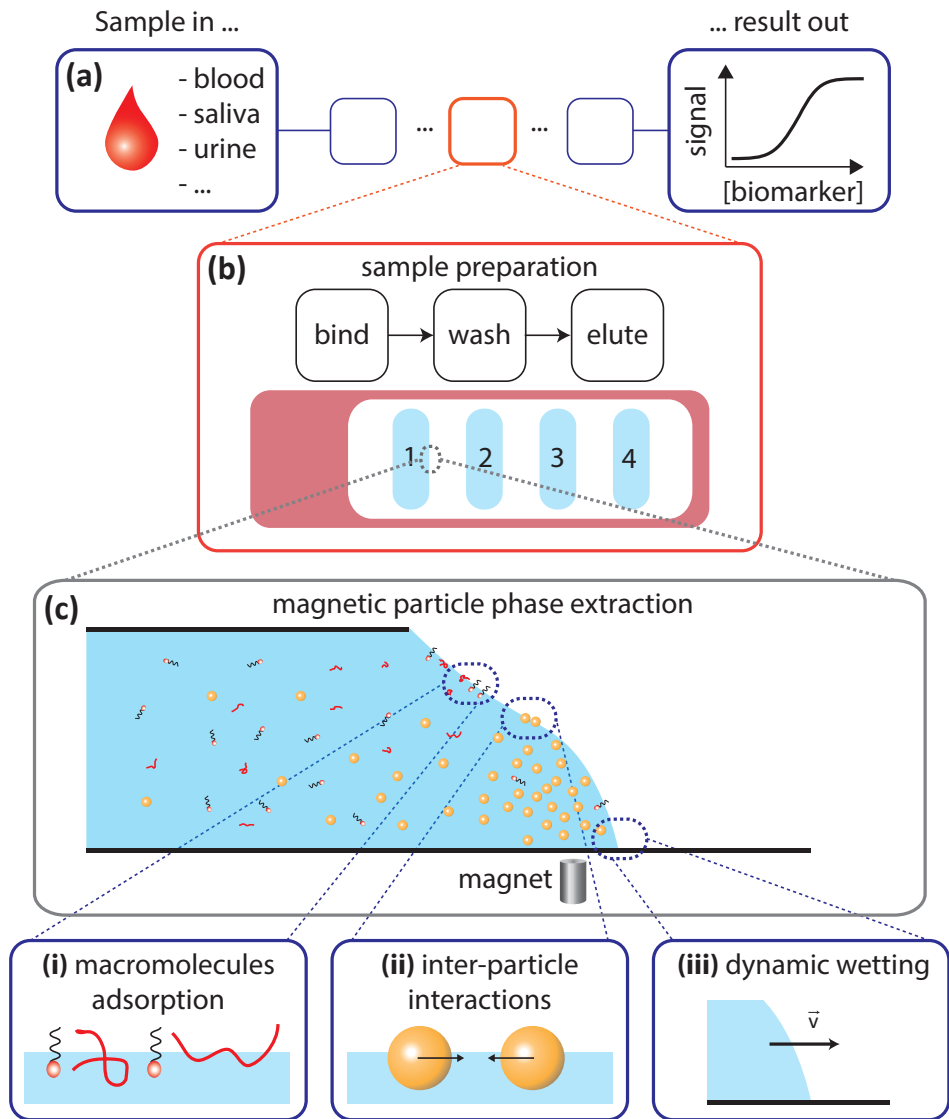


Figure 1.4: Example of the use of magnetic colloids for sample preparation in lab-on-a-chip biosensing. **(a)** Principles of biosensing: the presence of a biomarker in a biological fluid is quantified and translated into a readable signal. **(b)** Sketch of the Magneto-Capillary Particle Transport (MCPT) technology (top-view) used for sample preparation as developed in Ref.⁴³ and reviewed in Ref.¹² **(c)** Zoom-in (cross-sectional view) of the particles extraction process (drawing not to scale) **(i)-(iii)** We highlight some of the fundamental processes that are relevant for this thesis: **(i)** will be discussed in Chapter 3, **(ii)** will be discussed in Chapter 4, and **(iii)** will be discussed in Chapter 5. Figures **(b)** and **(c)** after den Dulk *et al.*⁴³

conformation. As an example, flexible polymers show relaxation kinetics within the layer that is severely retarded,^{45,46} leading to non-equilibrium layers, whose structure and dynamics depend on their adsorption kinetics and layer ageing. Proteins may change considerably at hydrophobic surfaces, as the inner hydrophobic structure of the protein exposes to the non-polar phase to an extent that might depend on the interface used (e.g. water-air or water-oil).⁷ Overall, the adsorbed layer will change the surface tension and the mechanical properties – i.e. the rheology – of the fluid interface. This phenomenon is known as *interface ageing*. For the MCPT technology, a change of the interfacial properties might affect fluid confinement and particle crossing.

(ii) *Inter-particle interactions*. Colloidal particles tend to adsorb to fluid interfaces due to their partial affinity to both phases. The rheological properties of the interface depends on the microstructure of the adsorbed particle layer.^{25,47,48} Electrostatic interactions and interfacial deformations are known to contribute to the inter-particle interactions (see Fig. 1.3a). Moreover, the local micro-environment of the particle might introduce deformations of the interface, which results in long-ranged forces and torques between particles, known as *capillary interactions*.³⁹ The presence of anisotropic interactions between particles at the interface (such as the one shown in Fig. 1.3b) may be problematic for applications where interfacial stability is required.

(iii) *Dynamic wetting*. On a macroscopic scale, the displacement of a fluid over a substrate can be described by the difference between the contact angle of the advancing part and the receding part of the moving fluid, so called contact angle hysteresis. In microfluidic devices the wetting properties of the surfaces determine the magnitude of capillary forces (Laplace pressure), which are of utmost importance at the micrometer scale.⁴⁹ On a microscopic scale, the dynamic wetting is determined by the molecular interactions of the fluid molecules with the atoms of the substrate.⁵⁰ This plays a dominant role in the adsorption process of particles at fluid-fluid interfaces, where the timescale for relaxation to equilibrium may range from a few seconds to several hours.^{51,52} However, the precise mechanism of dynamic wetting at the micro- and nano-scale remains only partially understood.

1.2 Overview of technological & fundamental challenges

The understanding of the physical mechanisms of wetting phenomena is of fundamental and practical importance for many applications, as highlighted by the examples drawn from the MCPT technology. In this section we briefly outline the technological and fundamental challenges related to each of these aspects, namely the study of the rheology of fluid-fluid interfaces, capillary interactions and dynamic wetting.

1.2.1 Interfacial microrheology

When two immiscible and pure fluids are in contact, the resulting fluid-fluid interface can be characterized by a single value of the surface tension. However, in most technological applications amphiphilic molecules populate the interface. The resulting microstructure determines the mechanical response of the interface upon external perturbations. The microstructure can both store and dissipate the deformation energy in a frequency-

dependent manner, reflecting visco-elasticity,^{53,54} or it may show a time-independent non-Newtonian behaviour, where the interfacial viscosity depends on the shear rate or shear rate history, characterized by shear-thinning or shear-thickening.^{55,56}

Traditional rheometers apply perturbations to the interface using probes with a typical size of a few millimeters or larger,²⁵ so called macro-rheology. As an example, oscillatory shear rheometers (e.g. knife-edge viscometer, plate surface viscometer, or magnetic needle rheometers) measure the frequency-dependent linear viscoelastic modulus of the interface. The phase difference between the applied stress and the response of the probe is used to determine the component of the interfacial shear modulus associated with the storage modulus (i.e. elasticity) and the loss modulus (i.e. viscosity).⁷ However, the macroscopic size of the probes limits the accuracy of the rheological measurements, where the velocity gradients of the surrounding bulk fluids dominate over interfacial contributions. This limits the applicability of macro-rheology techniques in biomedical research, where the relevant scales are well below the millimeter scale and the amounts of material are generally limited.^{26,56–58}

Microrheology refers to the use of micrometer-sized objects directly embedded in the fluid interface to measure interfacial shear viscosities on small length scales ($\sim \mu\text{m}$), small sample volumes ($\sim \mu\text{L}$), and with a high sensitivity.^{25,26,48,57–60} The simplest approach is to follow the microscopic Brownian motion of a probe in time using video-microscopy, which is referred as passive microrheology. The trajectory of the particle is then related to its frequency-dependent diffusivity using a mean-squared displacement (MSD) analysis.^{25,26,54,56,59,61} Passive microrheology ensures to probe the linear viscoelastic response of the interface. However, its use is limited to the measurement of low values of interfacial viscosities, as for higher values usually longer measurement times are required and artifacts may be present.²⁶

Another approach is to use external forces to control the motion of the probes, so called active microrheology. These forces allow one to measure higher interfacial viscosities, to reduce the number of probes required, and to reduce the measurement time to a few seconds, ideal to study time-dependent phenomena. Most of the reported studies are based on optical tweezers and magnetic tweezers experiments.^{62–67} From a fundamental perspective, the forced motion of a probe allows one to bring the system out of equilibrium and to explore many interesting and important material properties. However, the geometry of the probe and the dynamics of the actuation play an important role, and the interpretation of the data relies on the assumptions of the hydrodynamic model used.^{26,55,68,69}

1.2.2 Capillary interactions

The adsorption of particles to a fluid-fluid interface may be accompanied by an irregular shape of the particle meniscus due to the presence of surface roughness and/or chemical inhomogeneities.⁷⁰ The boundary conditions at the three-phase contact line (particle, phase 1 and 2) requires the interface to deform, resulting in long-ranged interactions between particles. Interfacial deformations may be also induced by gravity,^{71,72} by particles with shape anisotropy (e.g. ellipsoidal),^{73–75} or by the presence of external fields, such as electric and magnetic (see Fig. 1.3b).^{42,76} Danov *et al.* considered the convex and

concave local deviations of the meniscus shape from planarity as positive and negative capillary charges, in analogy with electrostatics, and derived a theoretical expression to describe the interaction between two particles of arbitrary multipole order.⁷⁷

Although the theoretical modeling and numerical techniques have advanced in the recent years, most of the reported literature of experimental approaches are based on – passive – video-microscopy.^{73,74,78,79} Direct methods have been mainly limited to optical tweezers experiments.^{40,80–82} The small size of the particles, the optical discontinuity between the two fluid phases, and the requirement that an actuation method should be able to control the positions and/or the forces on the particles makes the direct measurement of inter-particle interactions challenging.

1.2.3 Dynamic wetting

Wetting phenomena have been the center of many studies over decades and several experimental techniques have been developed. Static and dynamic wetting can be described at different temporal and spatial scales. On a macroscopic level, the motion of a fluid on a planar substrate can be described with observables such as viscosity, surface tension, wetting speed and dynamic contact angle. These observables are related to the interaction of the fluid molecules with the substrates at the micro- and nano-scale. However, despite much research over many years, the precise mechanism on how a liquid front advances across a solid remains only partially understood and leaves still many questions unanswered about the underlying physical mechanisms of contact line motion.^{3,14,50,83–86}

Recently, studies of particle adsorption to fluid-fluid interfaces have shown adsorption times that cannot be fully captured with a description based on capillary forces and hydrodynamic friction.^{51,52} These observations call for the development of methods to quantify and model dynamic wetting effects at the micro- and nano-scale.

1.3 This thesis

The aim of this dissertation thesis is to develop new methodologies using magnetic particles at fluid-fluid interfaces for the study of microrheology, capillary interactions and dynamic particle wetting. The use of magnetic particles has several advantages. Nowadays particles are available with a wide range of sizes, material and optical properties. Together with their ease of surface functionalization, magnetic particles can be used to study a wide range of material systems. The motion trajectories of micro-particles can be imaged with conventional microscopic techniques, with an accuracy in determining their translational position of a few nanometers.⁸⁷ Moreover, magnetic particles can be conveniently manipulated by external fields with 6 degree of freedom (3 translational and 3 rotational), with very low interference to organic materials. Their rotational motion can be resolved by coupling optical features, such as fluorescent nanoparticles, on the surface of the particles.^{88,89}

In Chapter 2 we provide a theoretical framework for this thesis. We describe the fundamental aspects of wetting on planar substrates and the physics describing the interaction of colloidal particles with fluid-fluid interfaces. Furthermore we discuss and review the status of experimental and numerical techniques to characterize the static and dynamic

wetting of single particles at fluid-fluid interfaces.

In Chapter 3 we introduce a new interfacial rheometry technique to quantify the drag of particles adsorbed to a fluid-fluid interface. Pairs of magnetic particles are repeatedly attracted and repelled by alternating the orientation of an external magnetic field, so-called interfacial rheometry by Intra-Pair Magnetophoresis (IPM). We apply IPM to study the time-dependent adsorption of polymer at a water-oil interface with a wide dynamic range of the particle drag coefficient and timescales.

In Chapter 4 we expand the use of the IPM technique to quantify capillary attractive interactions in a system with strong interface ageing. Particles are initially separated magnetically and then repeated motion trajectories are recorded in the absence of the field. The experiment gives an independent quantification of the interfacial drag coefficient and can reveal correlations with non-viscous attractive inter-particle forces in the system.

In Chapter 5 we propose a new method to study dynamic wetting on single colloidal particles at fluid-fluid interfaces. Magnetic particles are interrogated with external magnetic torques. The rotational motion trajectories reveal different wetting patterns that depend on the three-phase contact line friction on the particle surface and on interfacial deformations.

In Chapter 6 we conclude by summarizing the general insight acquired and propose future prospects.



2

Basic concepts of particles at fluid-fluid interfaces

The use of particles at fluid-fluid interfaces is interesting to study wetting phenomena, because in particle-based experiments small scale effects are dominant and quantitatively observable. In this Chapter we describe the fundamental aspects of wetting on planar substrates and the physics describing the interaction of colloidal particles with fluid-fluid interfaces. Furthermore we discuss and review the status of experimental and numerical techniques to characterize the static and dynamic wetting of single particles at fluid-fluid interfaces.^a

^aParts of this Chapter have been published as a review: S. Cappelli, Q. Xie, J. Harting, A.M. de Jong, and M.W.J. Prins, Dynamic wetting: status and prospective of single particle based experiments and simulations. *New Biotechnology*, 32(5):420-432, 2015.

2.1 Introduction

In the early 20th century the pioneering work of Ramsden and Pickering^{27,28} demonstrated that colloidal particles can be used to stabilize emulsions by adsorption at liquid interfaces. In 1980 Pieranski³⁰ described the adsorption energy in terms of the surface tension of the fluid-fluid interface and the particle wettability by the fluids, showing that for micrometer-sized particles the depth of the potential well is several orders of magnitude greater than the thermal energy. The strong adsorption of colloidal particles at fluid interfaces is being used in a wide range of applications. In froth flotation for example, the adsorption of particles is exploited for mineral extraction.⁴ More recently particle assembly at fluid interfaces has been studied as a platform for the design of novel colloid-based materials.^{11,24,36,38,76,90–93} In addition, the interaction between particles and fluid interfaces is important for the field of lab-on-a-chip biosensing, where particles are used for their large surface-to-volume ratio, flexible bio-functionalization, stability, and for their actuation and detection properties (see e.g. ref.¹²).

Wetting phenomena are ubiquitous in nature and technology. The description of these phenomena requires knowledge from several disciplines, such as chemistry, physics, and engineering.³ The study of wetting on planar surfaces dates back to 1805 when Young described the interaction of fluids with planar substrates.¹⁶ The surface wetting is characterized by the interfacial tensions and the resulting equilibrium contact angle, see Fig. 2.1a. The static contact angle refers to the equilibrium state. The contact angle changes in an out-of-equilibrium situation and is often described by a dynamic contact angle that has a directional and time-dependent character, with values for advancing and receding states, contact angle hysteresis, and contact angle relaxation, see Fig. 2.1b. Wetting happens at different temporal and spatial scales, but mostly only macroscopic observables, such as viscosity, surface tension, wetting speed and dynamic contact angle, are accessible. Static and dynamic wetting have been the center of many studies over decades and there are several experimental techniques available. Nonetheless, the micro- and molecular-scale origin of wetting phenomena complicates the development of model descriptions and leaves still many questions unanswered about the underlying physical mechanisms of contact line motion.^{3,14,50,83–86}

Colloidal particles at fluid-fluid interfaces are characterized by the three-phase contact angle formed between the two fluids and the solid particle,²⁴ see Fig. 2.1c. The small size of the particles (from a few nanometers to several micrometers) and the optical discontinuity between the two fluid phases makes the direct measurement of the contact angle challenging. Several approaches have been reported in the literature to measure static contact angles on particles, in the form of an ensemble measurement that records an average contact angle over many particles^{95–100} or a measurement that yields the contact angle of individual particles.^{101–109} These techniques measure a static value for the contact angle and neglect dynamic effects.

Recently it has been shown that the relaxation process of particles adsorbing to fluid-fluid interfaces can have a very long tail with contact line speeds as low as $10^{-1} \mu\text{m/s}$.^{51,52,110} A description based on capillary forces and hydrodynamic friction predicts initial speeds in the order of a few m/s and relaxation times in the order of μs .^{15,51} These observations

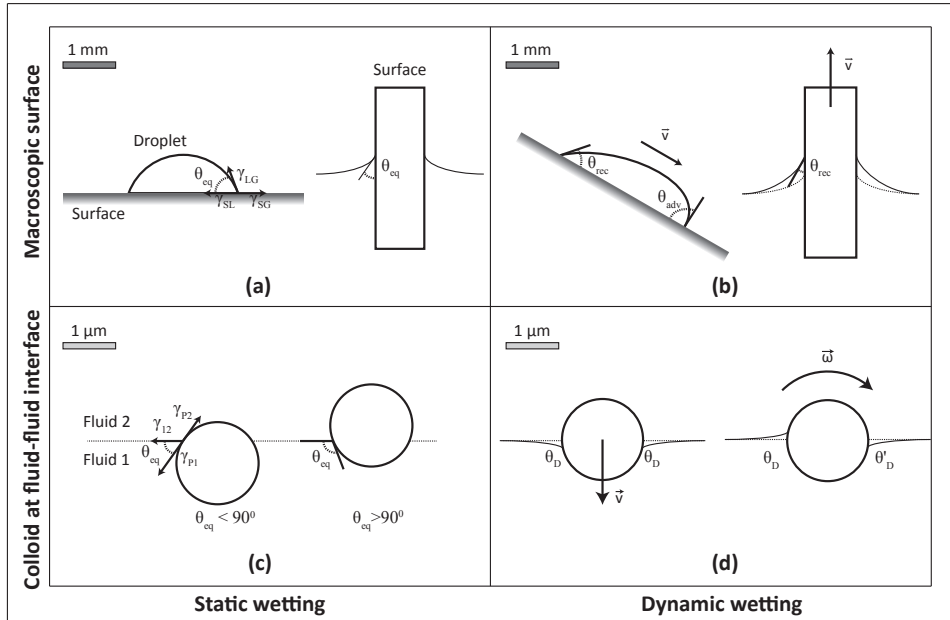


Figure 2.1: Wetting at different scales. On a macroscopic scale (a) static and (b) dynamic contact angles have been studied by placing a droplet on a planar substrate or by dipping a surface into a fluid. On a microscopic scale (c) static and (d) dynamic wetting are being studied using colloidal particles at fluid-fluid interfaces. Reprinted from Ref.,⁹⁴ Copyright (2015), with permission from Elsevier.

call for the development of methods to quantify and model dynamic wetting effects on colloids over a broad range of time and energy scales, preferably at the level of individual particles and suitable for a wide range of particle types, surface functionalizations, and fluid properties. Computer simulations might be used to complement experiments since they allow to model the impact of varying molecular interactions or microscopic surface properties such as roughness, elasticity, charges, or hydrophobic/hydrophilic interactions individually and to investigate the effect of these microscopic quantities on macroscopic measurements.^{111–118}

While a vast literature on numerical simulations of problems involving wetting is available, we limit ourselves to review contributions which utilize microscale algorithms such as molecular dynamics or mesoscale algorithms, such as the lattice Boltzmann method. Molecular dynamics simulations describe a system in terms of individual particles following Newton's equations of motion. Interactions between these particles ('molecules') are commonly implemented in terms of parameterized Lennard-Jones potentials to define the interaction of fluid and surface species. Due to the prohibitive computational cost of molecular dynamics simulations, they are generally limited to temporal and spatial ranges on the nanoscale. The lattice Boltzmann method overcomes this problem at the price of eliminating the molecular details of the involved materials. It is based on a phase space discretization of Boltzmann's equation, several multiphase extensions exist and the

implementation of complex geometries is exceptionally easy. Combined with the molecular dynamics algorithm, it is used to simulate particles with arbitrary shape, adjustable wettability, or different particle-particle interactions suspended in fluid. The method has become a mature alternative to classical computational fluid dynamics methods and is very popular in applications reviewed in this Chapter.

In this Chapter, we review and discuss the status of experimental and numerical techniques to characterize the static and dynamic wetting of single particles at fluid-fluid interfaces, following the scheme presented in Fig. 2.1. First we introduce the basic notions of wetting on planar substrates through Young's equation and the related techniques to measure static and dynamic contact angles (Fig. 2.1a,b) and we focus on the unanswered questions about the origin and scaling relationships of dynamic wetting. Finally, we outline experimental and numerical techniques to study static (Fig. 2.1c) and dynamic (Fig. 2.1d) wetting on single particles at fluid-fluid interfaces.

2.2 Contact angle on planar substrates

2.2.1 Static contact angle

“For each combination of a solid and a fluid, there is an appropriate angle of contact between the surfaces of the fluid, exposed to the air, and to the solid”, T. Young 1805.¹⁶ Two hundred years later, the measurement of contact angles is still the primary way to characterize the interaction of fluids with solid surfaces. This can be expressed with the homonymous equation

$$\cos \theta_{eq} = \frac{\gamma_{SG} - \gamma_{SL}}{\gamma_{LG}} \quad (2.1)$$

that relates the three surface tensions – γ_{SG} , γ_{SL} and γ_{LG} for the solid-gas, solid-liquid and liquid-gas interface respectively – with the equilibrium contact angle θ_{eq} (Fig. 2.1).^{3,16}

Surface tension is defined as the Gibbs free energy G per unit surface area⁸³ at constant temperature, pressure, and chemical potential, whose minimum determines the shape of the interface:

$$\gamma = \left[\frac{\partial G}{\partial A} \right]_{T,P,n} \quad (2.2)$$

In other words, γ can be seen as the energy that must be supplied to increase the surface area by one unit. As an example, the widely used water-decane interface has a surface tension of about 50 mN/m, or $10 k_B T/nm^2$, which represents a large energy density. By analogy with surface tension, the excess free energy per unit length²⁹ associated with a solid-fluid-fluid contact line L is defined as the line tension τ :^b

$$\tau = \left[\frac{\partial G}{\partial L} \right]_{T,P,n} \quad (2.3)$$

^bWe defined the contact line tension τ using the same notation as reported in literature. However, this must not be confused with a similar notation used to describe the torque applied on a particle, as we will introduce in Chapter 5.

For a droplet on a planar substrate with spherical cap geometry (e.g. see Fig. 2.1a) and radius R , the Young equation assumes the form

$$\cos \theta = \cos \theta_{eq} - \frac{\tau/\gamma}{R} \quad (2.4)$$

A curved interface is mathematically described by the Young-Laplace equation and gives rise to a pressure jump across the two fluids

$$\Delta P = \gamma \left(\frac{1}{R_1} + \frac{1}{R_2} \right) \quad (2.5)$$

where R_1 and R_2 are the two orthogonal or "principal" radii of curvature of the interface.^{15,37} The equilibrium shape of a fluid on a planar substrate results from the balance between interfacial and gravitational forces, which is expressed by a characteristic length scale, the capillary length

$$l_\gamma = \sqrt{\frac{\gamma}{\rho g}} \quad (2.6)$$

(typically 1 mm), where ρ is the density of the fluid and g is the gravitational acceleration. The three surface tensions uniquely define the angle of contact for the considered system, which is used to characterize the static wetting properties of a surface. For $\theta_{eq} = 0$ the fluid wets completely the surface, while for $\theta_{eq} > 0$ only partially. If the size of the droplet is smaller than the capillary length, then the droplet assumes a spherical cap geometry. A surface where the contact angle of a droplet is $0^\circ < \theta_{eq} < 90^\circ$ is referred as hydrophilic, while if $90^\circ < \theta_{eq} < 180^\circ$ the surface is referred as hydrophobic.

2.2.2 Experimental techniques

Contact angles on flat surfaces can be measured with sessile drop, captive bubble and Wilhelmy plate methods.^{3,14} In the sessile drop method (Fig. 2.1a, left) a droplet of fluid is dispensed on a surface and the goniometric angle is measured directly from a magnified image of the droplet at equilibrium. In the captive method the droplet, which is usually lighter than the surrounding fluid, is held captive from a top surface. With the Wilhelmy plate method a sample with a well-defined geometry is dipped in the liquid of interest (Fig. 2.1a, right) and the capillary force is directly measured with a microbalance.

The surface tension of two immiscible fluids, for example, a water-air or water-oil interface, can be measured with different methods, such as the ring tensiometer, spinning drop, pendant drop, and Wilhelmy plate.^{4,15} These methods can measure values of surface tension down to a few mN/m. For lower surface tension systems alternative methods based on confocal microscopy¹¹⁹ or microfluidics¹²⁰ are required.

Line tension has been long debated in literature and its existence and origin are still controversial.¹²¹ Theories based on statistical mechanics predict values in the range of $10^{-12} - 10^{-10}$ N. A direct method to estimate the magnitude of line tension τ is based on the measurement of the contact angle of fluids on a solid substrate as a function of droplet volume, which is then related to eqn (2.4). However, due to the small length scales involved and to the difficulties to measure contact angles due to hysteresis (see

Section 2.2.4), experimental values of τ vary greatly with positive and negative values in a range of $10^{-11} - 10^{-5}$ N.¹²¹

2.2.3 Numerical techniques

In computer simulations utilizing molecular dynamics or lattice Boltzmann methods the surface tension is often an input parameter. However, this is not the case for all multiphase and multicomponent models on the market. Furthermore, in the case of complex fluids such as suspensions or mixtures, the surface tension has to be obtained from simulations. Often the classical setup of Laplace is used, where a droplet is suspended in a secondary fluid and the surface tension can be obtained from the pressure difference between the inside and outside of the droplet together with the curvature of the interface. Alternatively, the surface tension can be directly obtained from integration of the pressure tensor across the fluid-fluid or fluid-solid interface.¹²¹⁻¹²⁵

2.2.4 Contact angle hysteresis

Young's equation (eqn (2.1)) assumes the contact angle to be in thermodynamic equilibrium on an ideal solid surface – smooth, insoluble, chemically homogeneous, nonreactive, and non-deformable.¹²⁶ In most experimental situations, chemical or topological heterogeneities are present. This becomes clear when we observe an out-of-equilibrium situation, such as a droplet on a tilted surface (Fig. 2.1b). The droplet first deforms and eventually starts moving downhill with different values for the advancing (θ_{adv}) and receding (θ_{rec}) contact angles. The difference between the two states is known as contact angle hysteresis ($\Delta\theta$):

$$\Delta\theta = \theta_{adv} - \theta_{rec}. \quad (2.7)$$

Contact angle hysteresis is omnipresent in nature – even for single crystal structures like mica or graphene – and is relevant for many technological applications, for example, dip coating, painting, and immersion lithography.¹¹ Contact angle hysteresis is the result of the interaction of the three-phase contact line with macroscopic (micrometer) and microscopic (nanometer) sized defects, where the local contact angle may assume values different from the macroscopic θ_{eq} . Contact angle hysteresis has been used to characterize surface heterogeneities.^{3,50,85,126,127} As an example, Bormashenko *et al.* studied contact angle hysteresis on different polymer substrates, finding that the pinning force of the contact line correlates with the dielectric constant of the polymer substrate.¹²⁷ On a macroscopic level, this represents the level of polarity of the polymer, which correlates with the surface energy of the substrates, which in turn is correlated to the measured contact angle. Numerically, contact angle hysteresis has been studied in the context of droplets on heterogeneous substrates or capillary filling using lattice Boltzmann^{111,112,128,129} and molecular dynamics simulations.¹³⁰⁻¹³²

2.2.5 Dynamic contact angle

Wetting – static and dynamic – is the result of microscale interactions of fluid molecules with a surface. The specific properties of the involved fluids and surface result in macroscopic effects which are typically characterized by experimentally accessible parameters such as viscosity, surface tension, wetting speed and (dynamic) contact angle. However,

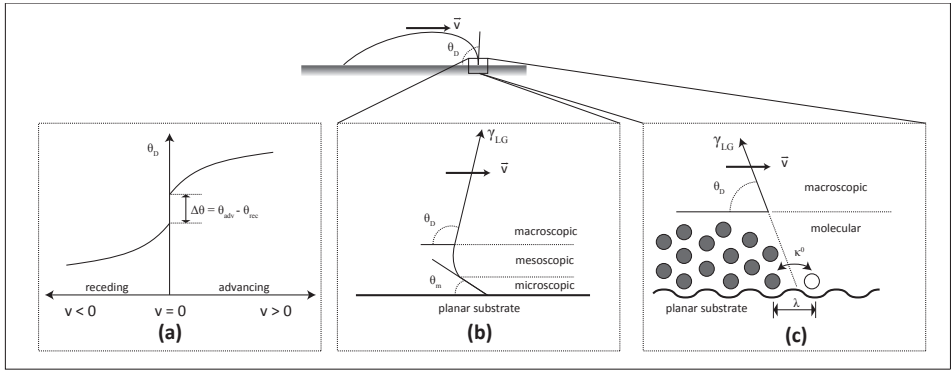


Figure 2.2: Dynamic wetting. (a) Velocity-dependence of contact angle on partially wetting substrates; the jump at zero velocity corresponds to contact angle hysteresis. Modeling of an advancing contact line on a planar substrate with (b) a hydrodynamic theory and (c) molecular kinetic theory. In (b) the contact line is described at three different scales: macroscopic, mesoscopic and microscopic, with $\theta_D \neq \theta_m$. In (c) the system is described at a molecular level as a thermally activated process with $\theta_D = \theta_m$. Reprinted from Ref.,⁹⁴ Copyright (2015), with permission from Elsevier.

this indirect quantification of the underlying microscopic processes complicates the development of models and leaves still many questions unanswered. Computer simulations might be used to complement experiments since they allow to model the impact of varying molecular interactions or microscopic surface properties such as roughness, elasticity, charges, or hydrophobic/hydrophilic interactions individually and to investigate the effect of these microscopic quantities on macroscopic measurements.^{111–118}

The motion of a contact line over a surface can be studied experimentally with passive and active methods. In spontaneous wetting, a droplet spreads on a flat surface and the dynamic contact angle θ_D or the contact line radius are measured as a function of time. In force driven wetting, the contact line is moved by external forces and dynamic contact angles are measured as a function of the speed v of the moving contact line. The scaling behavior of a moving contact line is often expressed with dimensionless quantities: the Reynolds number Re and Capillary number Ca

$$Re = \frac{vL}{\mu}, \quad Ca = \frac{v\eta}{\gamma} \quad (2.8)$$

where L is a characteristic linear dimension (e.g. the dimension of a microfluidic channel or the radius of a colloid), $\mu = \eta/\rho$ the kinematic viscosity, η is the dynamic viscosity and γ the surface tension. The Reynolds number represents the ratio between inertial forces and viscous forces; the Capillary number describes the relative effect of viscous forces and capillary forces.

As a general outcome of many reported experiments, the dynamic contact angle shows a directional and time-dependent character, with values for the advancing and receding contact angles depending on the velocity of the moving contact line (Fig. 2a). This dependency suggests that the process must be thermodynamically irreversible and therefore dissipative.^{50,85} Yet there is still no consensus on a physical model that can describe and

integrate the multi-scale aspects of dynamic wetting. The two main approaches to model the dissipation mechanism are the hydrodynamic theory and molecular kinetic theory. The complete treatment of these theories is outside the scope of this Chapter and we refer to recent reviews for further details.^{3,50,85,86} Below we outline the basic principles.

2.2.6 Hydrodynamic theory

The hydrodynamic theory assumes that the dissipation is caused by the viscous flow within the wedge of liquid near the moving contact line. The system is described at three different scales (Fig. 2.2b): *macroscopic*, where the conventional no-slip boundary condition is applied and the system is described by the dynamic contact angle θ_D ; *mesoscopic*, where viscous bending of the interface occurs; and *microscopic*, where the fluid is allowed to slip within few molecular layers above a solid substrate with a local microscopic contact angle θ_m ($\theta_D \neq \theta_m$). The relation between the viscous bending of the interface and the macroscopic contact angle can be expressed by the Cox-Voinov law¹³³

$$\theta_D^3 - \theta_m^3 = 9Ca \ln\left(\frac{L}{L_m}\right) \quad (2.9)$$

that relates the macroscopic θ_D and microscopic θ_m contact angles, the Capillary number Ca and macroscopic (L) (e.g. the capillary length) and microscopic (L_m) length scales. The latter parameter represents the typical length scale where the no-slip condition breaks. This model, valid for small Capillary and Reynolds numbers ($Ca, Re \ll 1$) on ideal surfaces, strongly depends on the boundary conditions imposed to the problem.

2.2.7 Molecular kinetic theory

The molecular kinetic theory (MKT) describes the contact line motion as a stochastic process. The motion of the contact line is described by individual molecules that hop in a potential well landscape provided by the atoms of the substrate, with equilibrium frequency κ^0 and average displacement λ . Here the contact angle is defined at a molecular scale (Fig. 2.2c) and has the same value as the macroscopic contact angle ($\theta_D = \theta_m$). The velocity-dependence can be interpreted as being the result of a perturbation of the equilibrium process, which gives rise to surface tension forces. An approximate solution is given by the relation

$$v = \frac{\kappa^0 \lambda^3 \gamma (\cos \theta_{eq} - \cos \theta_D)}{k_B T} = \frac{\gamma (\cos \theta_{eq} - \cos \theta_D)}{\xi} \quad (2.10)$$

where $\xi = k_B T / \kappa^0 \lambda^3$ is the friction coefficient and has the same unit as dynamic viscosity (Pa s).³

2.2.8 Comparison with experiments

Several authors^{3,50,86,134} have reported studies on specific wetting geometries in order to test the proposed models. For example, data can be obtained by pushing fluids into capillaries, or by dip coating substrates into a pool of liquid at different velocities. In

most of the cases, both models can reproduce the data for low Capillary numbers, despite the fact that the models are based on different physical mechanisms.

A limitation for the hydrodynamic model is to have accurate information about θ_m , which is typically assumed to be either $\theta_m = 0$ (a totally wetting fluid with a precursor film) or $\theta_m \approx \theta_{eq}$. The associated length scales are typically $L/L_m \approx 10^4$. For the molecular kinetic model, the value of the equilibrium frequency may vary by several orders of magnitude, while λ is usually of the order of a few nanometers. Values for the contact line friction are found to be higher than the dynamic viscosity of the fluid. Furthermore, the MKT model lacks a link to the hydrodynamics of the system. The main limitation of both models is the inability to predict the parameters for a given solid-liquid system. The key parameters usually have to be treated as adjustable parameters and obtained from experiments by curve-fitting procedures.

For high Capillary numbers, there is a maximum speed for the contact line motion and wetting transitions may occur, such as the deposition of liquid films, breakup of liquid drops, or entrainment of air bubbles. This topic has been recently reviewed by Snoeijer *et al.*⁸⁶ They conclude that at low wetting speeds the dissipation is mainly dominated by thermal activation and at higher speeds by hydrodynamics. Moreover at very short timescales the spreading of droplets on partially wetting surfaces is dominated by inertial effects rather than viscous effects, and is independent of substrate wettability.¹³⁵

Wetting is a complex problem because phenomena at different length and timescales need to be coupled. Models based on hydrodynamic and molecular kinetic theories can describe equally well the experimental data, although the underlying physical mechanisms are different. The difficulty to access microscopic scales makes it difficult to prove or disprove one model or the other. Thus new experimental techniques accompanied by reliable numerical tools are needed. The study of wetting on single colloidal particles trapped at fluid-fluid interfaces may offer novel avenues where small scale effects are dominant and quantitatively observable.

2.3 Interaction of particles with fluid-fluid interfaces

The transport of a spherical colloidal particle leading to adsorption to a fluid-fluid interface depends on its distance z from the interface (Figure 2.3). At large distances ($z \gg R$), the motion of the particle is dominated by a diffusive transport. In proximity of the interface ($z \approx R$), an adsorption energy barrier may be present, e.g. electrostatic or steric. When the particle breaches the interface ($z < R$), interfacial forces drive the motion of the particle within the interface. In the following we will describe the physics governing these processes.

2.3.1 Diffusion of a particle in proximity of a fluid interface

The Stokes' law describes the friction force that a spherical particle of radius R experiences while moving with velocity \mathbf{v} in a fluid of viscosity η :

$$\mathbf{F} = 6\pi\eta R \cdot \mathbf{v} \quad (2.11)$$

The proximity of a fluid-fluid interface ($z \approx R$) contributes to an apparent increase of the drag of the particle. This can be taken into account by considering a correction

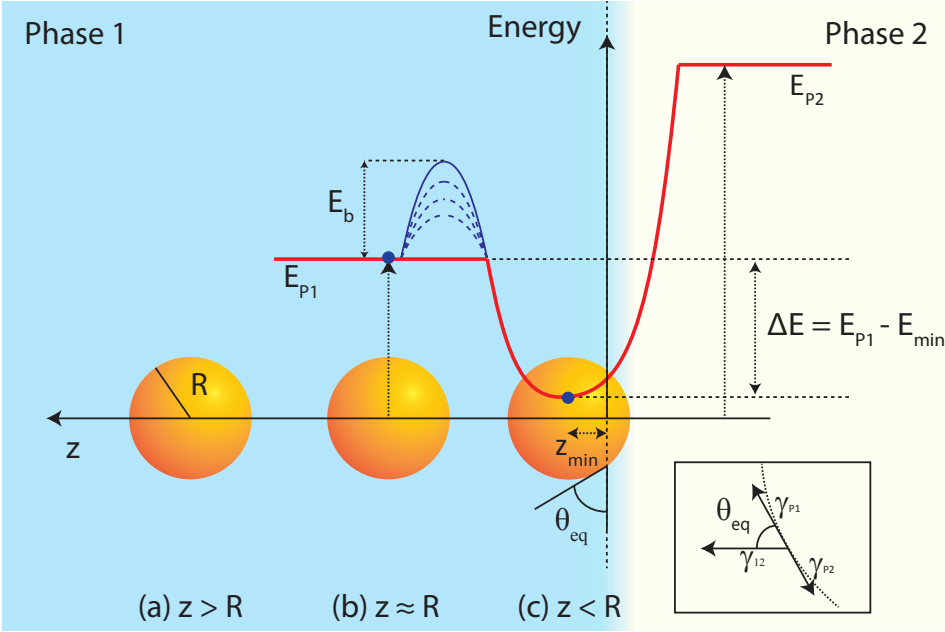


Figure 2.3: Transport of a spherical particle of radius R towards a fluid-fluid interface formed by two immiscible phases. (a) Bulk diffusion for $z > R$; (b) particle-interface interaction for $z \approx R$; (c) particle adsorption for $z < R$.

parameter $\lambda = \lambda(\eta_1, \eta_2, h)$, as described by Brenner¹³⁶ and Bart.¹³⁷

$$\mathbf{F} = 6\pi\eta R \cdot \lambda \mathbf{v}, \quad (2.12)$$

where

$$\lambda = \frac{4}{3} \sinh \alpha \sum_{n=1}^{\infty} \frac{n(n+1)}{(2n-1)(2n+3)} \left\{ \frac{\eta_1 X_n + \eta_2 Y_n}{\eta_1 V_n + \eta_2 T_n} - 1 \right\}. \quad (2.13)$$

As an example, Tsai *et al.* proved experimentally the validity of this model by measuring the normal component of the speed of paramagnetic particles pulled magnetically towards a water-oil interface.¹²⁰

2.3.2 Electrostatic interaction

A method to stabilize colloidal particles in an aqueous solution is to functionalize the surface of the particles with charged groups. The resulting electrostatic – repulsive – forces prevent the particles to cluster. When a charged particle approaches a fluid-fluid interface – charged or neutral – it experiences a repulsive net force due to two contributions. (i) *Confinement effect*: the double layer surrounding the colloid is heavily distorted by the presence of the interface, which is impenetrable by ions. (ii) *Image charge effect*: if a charged particle is diffusing from a high dielectric medium (e.g. water, $\epsilon_{water} \approx 80$) towards a lower one (e.g. air $\epsilon_{air} \approx 1$, or decane $\epsilon_{decane} \approx 2$), image-charges arise, which are always repulsive.

Mbamala *et al.*¹³⁸ described this interaction within the framework of Poisson-Boltzmann (PB) theory. The PB equation can be written as

$$\nabla^2 \phi = \kappa^2 \sinh \phi. \quad (2.14)$$

where $\phi = e\beta\psi$ is the normalized potential and ψ the electrostatic potential. Once ϕ is known, the grand potential Ω_h can be calculated, and therefore the particle-interface interaction $\beta V(h) = \Omega_h - \Omega_\infty$. This problem has only a numerical solution. An analytical solution can be achieved by using a linear version of eqn (2.14) and assuming $\epsilon'/\epsilon \rightarrow 0$ ($\epsilon' \approx 80$ and $\epsilon = 2$). These considerations led to the following result of the interaction potential:

$$V(h) = \left(\frac{Ze^{\kappa a}}{1 + \kappa a} \right)^2 \frac{\lambda_B}{2\beta} \cdot \left(\frac{e^{-2\kappa h}}{2h} \right) \quad (2.15)$$

where $Z = \sigma 4\pi a^2$ is the number of charges on the colloid, $-\sigma$ is the surface charge density, $\lambda_B = \frac{e^2 \beta}{4\pi \epsilon_0 \epsilon_r}$ is the Bjerrum length, $\kappa^2 = 8\pi \lambda_B c_s$ is the screening parameter (that is the inverse of the Debye length) and c_s is the bulk ion concentration. The screening parameter κ can be modified by changing the electrolyte concentration of the water phase. If the ionic strength of the solution I_s is increased also κ increases and therefore the size the double layer around the particle. This results in the decreasing of the DL adsorption barrier.

The total energy of interaction between a particle and a fluid interface may contain additional terms, such as van der Waals, interfacial bending, or steric interactions. We refer the reader to ref.¹⁸ for more details.

2.3.3 Interfacial forces

A particle trapped at a fluid-fluid interface can be described by Young's equation (eqn (2.1)), where now the three phases are the surface of the particle and the two fluids. For a water-air interface, if the contact angle is $0 \leq \theta \leq 90^\circ$ then the particle is more immersed in the water (hydrophilic), while for $90^\circ \leq \theta \leq 180^\circ$ the particle is more exposed to the air (hydrophobic).

The energy of adsorption of such a particle can be calculated by considering the contribution of the surface free energies of the three phases³⁰ (see Fig. 2.3c). The total energy for the system as a function of the immersion depth z is the sum of all of the interfacial energy contributions:

$$G(z) = \pi R^2 \left(2\gamma_{P1} \frac{z}{R} + 2\gamma_{P2} \left(1 - \frac{z}{R} \right) - \gamma_{12} \left(1 - \frac{z^2}{R^2} \right) + \frac{2\tau}{R} \left(1 - \frac{z^2}{R^2} \right)^{1/2} \right) \quad (2.16)$$

where the first two terms are the contribution from the portion of the particle exposed to phase 1 and phase 2 respectively (see eqn (2.2)), the third term is the gain in energy due to the removal of a portion of the interface, and the last term is the energy associated with the line tension (see eqn (2.3)).

We first discuss the case in which line tension is neglected. By differentiating eqn (2.16) with respect to z/R , it is possible to demonstrate that a minimum exists for

$$\frac{z_{min}}{R} = \cos \theta_{eq} \quad \text{if} \quad \left| \frac{\gamma_{P2} - \gamma_{P1}}{\gamma} \right| \leq 1, \quad (2.17)$$

otherwise if

$$\left| \frac{\gamma_{P2} - \gamma_{P1}}{\gamma} \right| \geq 1 \quad \begin{cases} \gamma_{P1} > \gamma_{P2}, & \text{particle in phase 2} \\ \gamma_{P1} < \gamma_{P2}, & \text{particle in phase 1} \end{cases} \quad (2.18)$$

The energy of adsorption can be calculated by considering the difference between the energy of the particle being immersed in one of the two phases and the energy of the particle at the interface (eqn (2.16)), and using eqn (2.1). This yields

$$\Delta E = -\pi R^2 \gamma_{12} (1 - |\cos \theta_{eq}|)^2 \quad (2.19)$$

which depends on the radius R of the colloid, on the fluid-fluid interface surface tension γ and the particle three phase contact angle θ_{eq} at equilibrium, as sketched in Fig. 2.3c. This energy is usually much larger than the thermal energy. As an example, for a particle of $1 \mu\text{m}$ radius at a water-decane interface ($\gamma \approx 50 \text{ mN/m}$), with $\theta_{eq} = 90^\circ$, the adsorption energy is about $\Delta E \approx 10^7 k_B T$, making the desorption process practically irreversible (see Fig. 1.2).

If we now include the line tension term in eqn (2.16), the minimization of the interfacial free energy with respect to the particle contact angle yields the so called modified Young-Dupré equation²⁹

$$\cos \theta = \cos \theta_{eq} \left(1 - \frac{\tau}{R\gamma \sin \theta} \right)^{-1} \quad (2.20)$$

This equation shows that line tension may change the equilibrium contact angle θ_{eq} for small enough particles ($R \sim \tau/\gamma$). Experiments on micrometer sized particles at liquid-vapour interfaces have provided estimates of line tension not larger than 10^{-8} N .²⁹ For typical values of the surface tension ($\gamma \sim 30 \text{ mN/m}$) the line tension becomes relevant for nanoparticles with radius $R \sim 300 \text{ nm}$. However, line tension measurements on nanoparticles are challenging and other effects such as roughness of the particle, electric charges on the particle, or the presence of surfactants, might contribute to deviations from the equilibrium contact angle as predicted by Young's equation.²⁹ In this thesis we neglect any effects due to line tension as the particles used have sizes in the micrometer range.

2.3.4 Inter-particle interactions

The interactions of particles at fluid-fluid interfaces differ both in range and nature with respect to the interactions in the corresponding single fluid phase. Hydrophilic colloidal particles bear surface charges in order to be stable in an aqueous solution. Away from the isoelectric point, electrostatic repulsive forces dominate over the short range van der Waals attractive forces, extending over tens or hundreds of nanometers depending on the

particle surface charge and fluid ionic strength.^{37,139} The presence of a fluid-fluid interface between a polar and non-polar fluid (e.g. a water-oil interface) creates an asymmetric distribution of charges across the interface, which creates an electric dipole responsible for strong repulsive forces between particles.^{29,36,38–40} According to the analysis provided by Hurd,¹⁴⁰ the magnitude of the electric dipole is determined entirely by the charge dissociation in the polar phase. Aveyard *et al.*⁸⁰ proposed an alternative model based on the assumption that a small amount of residual charges may be present in the non-polar phase, as the result of residual water in the non-polar phase, or water entrapped in the cavities of the surface roughness of the particle. The absence of a charge screening effect in the non-polar phase would suffice to generate the observed long-ranged electrostatic interaction between particles. Although both models predict a same functional form of the resulting interacting force, a consensus on the underlying physical origin of this interaction is still lacking.⁴⁰ Here, we limit to report the functional form of the electrostatic interaction force between two particles at a fluid-fluid interface:

$$F_{el} = F_0 \left(\frac{R_A + R_B}{S} \right)^4 \quad (2.21)$$

where S is the center-to-center inter-particle separation distance, F_0 is the closest proximity force that depends on the particles and fluids properties, and R_i is the radius of particle i .

Another class of interactions that have no counterpart in bulk fluids are capillary interactions, which originate from the overlap of local deformations of the interface. Deformations of the interface may be induced by gravity,^{71,72} by particles with shape anisotropy (e.g. ellipsoidal),^{73–75} or chemical anisotropy (e.g. Janus particles),¹⁴¹ by the presence of an external torque,¹⁴² or induced by surface patterning.^{41,143} These interactions are responsible for long-ranged capillary forces and torques between particles that cause particles to aggregate, to form chains and long-ranged ordered structures.

Danov *et al.*⁷⁷ formally treated the concave and convex deviations of the meniscus shape from planarity as positive and negative capillary charges, in analogy with electrostatics. The inter-particle potential can be then described as the superposition of capillary multipoles (capillary charges, dipoles, quadrupoles etc.). An asymptotic solution of the inter-particle potential between two capillary multipoles with an arbitrary order and large distances S is given by the relation

$$\Delta E_{AB}(S) \approx -\pi\gamma G_0 H_A H_B \cos(m_A \phi_A - m_B \phi_B) \frac{r_A^{m_A} r_B^{m_B}}{S^{m_A+m_B}} \quad (2.22)$$

where γ is the surface tension between the two fluid phases, H_A and H_B are the undulation amplitudes of the menisci around particles A and B , m_A and m_B are the respective multipole orders ($m = 0, 1, 2, \dots$) with orientations ϕ_A and ϕ_B , G_0 is a constant that depends on the multipole orders, and r_A and r_B are the radius of the particle cross section with the interface.

The relative contributions of gravity and surface tension to deformations of the inter-

face can be expressed by the particle Bond or Eötvös number^c $Eo = \frac{\Delta\rho g R^2}{\gamma}$, where $\Delta\rho$ is the difference between the particle density and fluid density, R is the particle radius, and g is the gravitational acceleration constant. Typically, for micrometer sized particles ($< 10 \mu\text{m}$), $Eo \ll 1$ and deformation due to gravity can be neglected. For spherical particles dipolar deformations ($m = 1$) require the application of an external torque. Therefore, the first non-vanishing term is the quadrupolar interface deformation ($m = 2$) and the resulting force between two identical particles can be expressed as

$$F_{quad} = -\frac{\delta E_{AB}}{dS} = -48\pi\gamma H_2^2 \cos(2(\phi_A - \phi_B)) \frac{r_c^4}{S^5} \quad (2.23)$$

where H_2 is the amplitude of the quadrupolar meniscus and r_c is the radius of the cross section formed by the particle with the interface, which is related to the equilibrium contact angle θ by the geometrical relation $r_c = R \cos \theta$ (Fig. 2.3c).

Interfacial deformations can be induced also by the electric field generated by charged particles adsorbed at a polar non-polar interface.¹⁴⁴ The electric field gives rise to mechanical stresses described by the Maxwell pressure tensor.¹⁴⁴ The resulting force, known as electro-dipping force, is directed towards the liquid of highest dielectric constant, usually the water phase, thereby deforming the interface. This force is independent of the ionic strength of the aqueous phase, suggesting that the force is mainly caused by charges at the particle-non-polar interface.¹⁴⁵ The interaction between two like-charged particles can be described by a superposition of electrostatic repulsion and electrocapillary attraction induced by the electrocapillary force. The electrostatic interaction force is described by eqn (2.21), while the electrocapillary interaction force is described asymptotically as a superposition of two dipoles, with a force that scales with inter-particle distance as $F_{ec} \propto 1/S^4$.

Other forces, such as Van der Waals, fluctuation forces and solvation forces, may also be present. However, these forces are usually significant only at short separation distances ($\sim\text{nm}$) and for nanoparticles. We refer the reader to ref.²⁹ for a more detailed description. In Table 2.1 we summarize the properties of inter-particle interactions that may occur at fluid-fluid interfaces.

2.4 Particles at fluid-fluid interfaces: static contact angle

In section 2.2 we focused on unanswered questions about the origin and scaling relationships of dynamic wetting. One important challenge is to gain access to the small scale of a moving contact line. This problem may be addressed by studying wetting on single colloidal particles at fluid-fluid interfaces. In the next sections we outline experimental and numerical techniques to study static and dynamic contact angles on single particles at fluid-fluid interfaces.

^cIn this thesis, we will refer to the Bond or Eötvös number as Eo , in order to distinguish it from the Boussinesq number Bo (see Chapter 3).

Table 2.1: Summary of the interactions between particles at fluid-fluid interfaces as described in Section 2.3.4. The interaction potential is generically given by (functionality) \times (strength). In the last column we indicate the typical particle size for which the interaction is expected to play a significant role. Table after F. Bresme *et al.*²⁹

Interaction	Character	Functionality	Strength ($k_B T$)	Particle size
Electrostatic				
-dipolar	rep	$(2R/S)^3$	$10 \dots 10^5$	nm... μm
Capillary				
-gravity	attr/rep	$\ln(2R/S)$	$10 \dots 10^5$	nm...mm
-dipolar	attr/rep	$(2R/S)^2$	$10 \dots 10^5$	μm
-quadrupolar	attr/rep	$(2R/S)^4 f(\phi)$	$1 \dots 10^5$	μm
-electrocapillary	attr	$(2R/S)^3$	$1 \dots 10^3$	100 nm... μm

2.4.1 Experimental techniques for measuring the contact angle of particles at fluid interfaces

The equilibrium contact angle of colloidal particles trapped at fluid interfaces cannot be measured with the same techniques as for planar surfaces. The main differences are the small scales of the system (micro- and nanoparticles) and the presence of an optical discontinuity between the two fluids. Several approaches have been reported in literature and the topic has been recently reviewed by Maestro *et al.*³⁶ Here we will discuss some of the techniques, with focus on single particle methods.

We can distinguish two different approaches: ensemble measurements and single particle based methods. Ensemble measurements deduce an average contact angle from a measurement on a large number of colloids. In many cases the results are obtained with assumptions that can be difficult to verify. For example, in the Washburn technique⁹⁵ a powder bed with irregular nanometer sized particles is put in a capillary and the position as function of time of a fluid adsorbing into the powder is measured. The contact angle is extracted by fitting the data to a model function. The model relies on the pore diameter of the wetted powder, whose physical meaning is a matter of debate. In a Langmuir trough experiment⁹⁶ pressure and area are measured upon compression of the interface containing the particles. During the process the particles are tightly packed and eventually expelled from the interface. The contact angle is extracted from the measured critical pressure, assuming no deformation of the interface.

Single particle based techniques have interesting advantages. Ideally the measurements are direct, with minimal assumptions to extract contact angles. Furthermore, a measurement on single particles allows one to investigate small-scale effects and to quantify particle-to-particle variability. In an early report, Mingins *et al.*¹⁰¹ directly observed 50 μm silica particles on a water-air interface of a pendant drop and extracted the contact angle from microscope images. Hadjiiski *et al.*¹⁰³ measured the interference pattern of micrometer sized particles on a substrate trapped in a thin film and the value of the contact angle was extracted from the meniscus profile. Horozov *et al.*¹⁰⁷ developed a similar interferometric technique, but now with a particle bridging a thin film. Preuss *et al.*¹⁰⁴ glued a colloidal particle onto the cantilever of an atomic force microscope (AFM). In

this colloidal probe AFM experiment, the particle is brought into contact with the interface, where capillary forces cause the cantilever to bend. Upon further approach of the probe, it reaches a zero-force position and thereafter forces apply in the opposite direction. Depending on the direction of cantilever actuation, values for the advancing and receding contact angles can be extracted, using the radius of the particle and the difference between the first-contact and the zero-force positions. The contact angle was measured for a $5\ \mu\text{m}$ silica particle at a water-air interface with and without the presence of surfactants.

Paunov *et al.*¹⁰⁵ developed a gel trapping technique (GTT) to measure contact angles on single nanoparticles with a diameter of 100 nm. The technique uses a thermo-responsive non-adsorbing gellant agent in the water phase. Then a soft polymer (PDMS) is used to replace the oil phase and trap the particles upon solidification, thereafter the mold is analyzed with a scanning electron microscope or AFM.¹⁴⁶ An alternative solidification technique was developed by Isa *et al.*¹⁰⁸ Particles were spread at a fluid-fluid interface, and after jet-freezing and cracking of the interface, the particles were metal-coated at a specific angle, thus forming a shadow. By measuring the geometry of the shadow with SEM images, it is possible to quantify the contact angle. The technique allows one to measure the contact angle of particles with diameters down to 20 nm. N. Vogel *et al.*¹⁰⁹ reported a method to study particles at a water-air interface based on polymerization. A monomer is introduced in the gas phase that polymerizes in contact with the water phase. Thereafter the film is analyzed with scanning electron microscopy and the value of the contact angle is extracted.

Maestro *et al.* compared the contact angle values obtained with different techniques for different particle-interface systems; see Table 1 in Ref.³⁶ Their extensive analysis shows that several parameters influence the measured values, such as particle radius, chemical nature of the surface, charge density, roughness and porosity, fluid properties, and the experimental protocol. The large number of parameters and the lack of an extensive study over a wide range of particle-interface systems make it still difficult to predict values for contact angles from a priori knowledge of a system. Moreover, as for planar surfaces, contact angle hysteresis is present and the measured contact angle is an apparent value. Contact angle hysteresis is a dynamic effect and depends on the history of the moving contact line. The above mentioned solidification techniques do not allow studies of such dynamic effects.

Another aspect that strongly affects the behavior of colloidal particles is the shape of the interface. Particle surface heterogeneities may distort the interface at the three-phase contact line, which can be described as a superposition of capillary multipoles, in analogy with electrostatics (capillary charge, dipole, etc.)^{39,41,74,147-149} The overlap of these interfacial deformations result in long-range interactions between particles at interfaces, thus controlling the assemble into ordered structures. As an example, interfaces with anisotropic curvature may change the particles assembly from an hexagonal (flat interface) to a square lattice (as a result of quadrupolar interactions).⁴¹ This effect is particularly important for anisotropically shaped objects, which assemble in preferred directions.^{74,76,150}

Prior to any measurement, particles need to be positioned at the interface. This can be done either by spontaneous adsorption from the bulk fluid or with the use of spreading

solvents (typically alcohols) that frequently implies a turbulent flow at the interface.³⁶ As an example, Table 1 of Maestro *et al.* shows that for the same system – 2 μm diameter PMMA particles at a water-air interface, measured with the gel trapping technique – the measured contact angle changes significantly depending on the solvent used – 56° for isopropanol and 29° for methanol. The difference is attributed to the solvent molecules adsorbed to the surface of the particles.¹⁵¹ Variability may also arise from the dynamic nature of wetting. Initially, the capillary forces and hydrodynamics of a particle adsorbing to a fluid-fluid interface give wetting speeds in the order of a few m/s, while also longer timescale relaxation processes are observed with speeds as low as 10^{-3} $\mu\text{m/s}$.^{51,52,110} Such dynamic wetting effects should be taken into account when extracting values for the contact angle. The capillary adsorption energy (eqn (2.19)) depends on the curvature of the interface, but it becomes significant only when the curvature of the interface is comparable with the radius of the particle.¹⁵²

2.4.2 Numerical techniques to simulate particles in the vicinity of fluid interfaces

Particles at fluid interfaces have been studied using (semi-)analytical treatment and computer simulations by numerous authors in the past. However, in most cases the hydrodynamic properties of the involved fluids are ignored in order to simplify the problem and to save computing time.^{141,147,149,153–157} While these works have provided a thorough insight of the general behavior of particles at interfaces, they are only of limited applicability for understanding dynamic wetting properties. To understand the fundamental origin of wetting a proper treatment of hydrodynamics and the dynamic movement of the contact line or deformability of the interface is required.

Simulation methods which are able to cover the movement of particles and the hydrodynamics of the fluid-fluid interface can generally be classified as hybrid approaches: the particles follow Newton's equation of motion and can be treated by standard molecular dynamics or discrete element algorithms. The fluids have to be treated on the level of a multiphase or multicomponent solver recovering the Navier-Stokes equation or at least the Stokes equation. Molecular dynamics is a possible method here, but its applicability is limited by the huge computational costs involved.¹⁵⁸ Often diffuse interface models are applied in order to avoid the complicated tracking of the interface and in particular the three phase contact line.

Finally, the particle- and fluid solvers have to be coupled, which needs to be implemented by a consistent treatment of momentum transfer between the fluids and the particle surface on a scale sufficiently smaller than the particle diameter. Typical choices for the flow solver include classical finite element methods,¹⁵⁹ dissipative particle dynamics (DPD) and again the lattice Boltzmann method. Algorithms involving the lattice Boltzmann method have been successfully applied to study the formation of particle stabilized emulsions such as Bijels and Pickering emulsions involving spherical^{91,160,161} and anisotropic particles such as ellipsoids.¹⁶² Furthermore, these methods have been used to study particle covered droplets or particles at interfaces under the influence of external fields.^{76,124,163} Static wetting effects can be easily controlled by tuning, for example, the surface properties of the particles and parameters such as the particle contact angle are

directly accessible from the fluid concentration fields obtained in the simulation.^{161, 164–166}

2.5 Particles at fluid-fluid interfaces: dynamic wetting

Dynamic wetting plays an important role in the adsorption process of colloids at fluid-fluid interfaces. A description of the adsorption process based on capillary forces and hydrodynamics results in exponential relaxation times with typical timescales of μs . Recently much longer timescales – several minutes or even hours – were measured.^{51, 52, 110} These observations call for the development of methods to quantify and model dynamic wetting effects on individual particles over a broad range of time and energy scales, and suitable for a wide range of particle types and fluid properties.

The dynamic nature of wetting can be studied by monitoring the spontaneous adsorption of a particle and by perturbing its equilibrium position (Fig. 2.1d). This requires the ability to measure the time evolution of the position of a particle with respect to the interface, and an actuation method in order to move a particle out of its equilibrium position. In the following paragraphs we outline experimental and numerical techniques to study dynamic contact angles on single particles at fluid-fluid interfaces. Finally we conclude by discussing the status and future of single particle based experimental techniques, and we propose a method based on magnetic tweezers.

2.5.1 Experimental techniques

Kaz *et al.*⁵¹ studied the relaxation to equilibrium of colloids using digital holographic imaging in combination with optical tweezers (Fig. 2.4a). They recorded trajectories of micrometer-sized polystyrene particles with different surface chemical properties as they approached and breached a water-decane interface (Fig. 2.4b). Holographic images were generated by illuminating the particles with a laser. The two fluids were index matched and the axial position of the particle was calculated by solving the Lorentz-Mie scattering equation in bulk. Another laser was focused on the back of a high numerical aperture microscope objective, creating an optical trap⁸¹ in order to move the particle towards the interface. With this setup the 3-dimensional position of the particle was resolved with 2 nm spatial resolution and sub-millisecond time resolution.

The initial approach trajectory can be explained by the hydrodynamic interaction of the particle with the interface (Fig. 2.4b). A particle in a low salt water solution (1 mM) reaches a steady level in proximity of the interface, while for a higher value (100 mM) the particle breaches the interface. This is attributed to the electrostatic barrier that arises when charged particles approach an interface between a high dielectric (water) and a low dielectric medium (decane).^{38, 138} After a sudden jump the particle follows a logarithmic trajectory (Fig. 2.4b). The position of the interface, and so the apparent contact angle, is computed from the relative position of the particle right before the snap-in process.

The results were interpreted with a molecular kinetic theory,⁵⁰ as described in section 2.2.5. The model describes the motion of the contact line as a stochastic process. Local surface heterogeneities trap fluid molecules in a potential well, whose energy is modified by a driving capillary force. The velocity of the contact line is related to the rate at which it hops over surface defects with average area A . This model is able to describe the observed

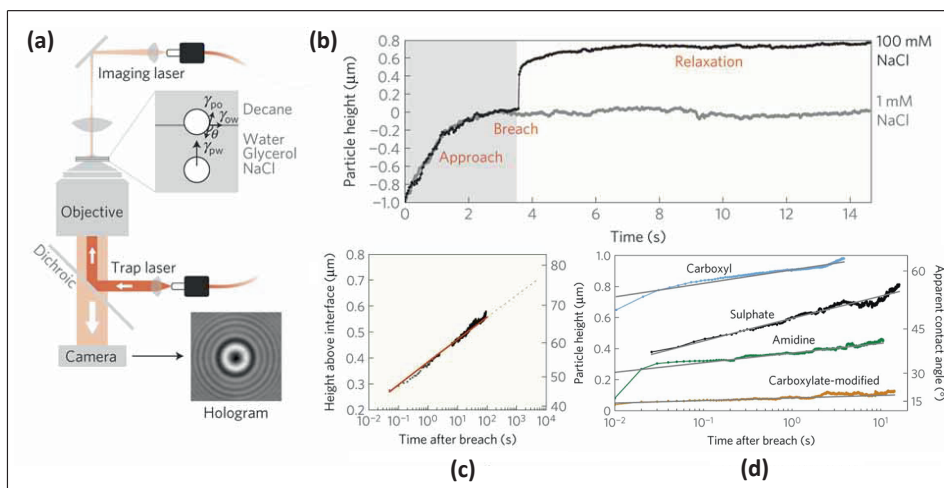


Figure 2.4: Study of relaxation to equilibrium of particles at a water-decane interface, as reported in Ref.⁵¹ (a) Sketch of the experimental setup: an optical trap is used to bring a particle towards the interface and its height is measured using holographic imaging microscopy. (b) Approach curves of 1.9- μm -diameter polystyrene particles at low and high salt concentrations. The position of the interface is determined from the sharp transition when the particle breaches the interface. (c) Trajectory of a particle relaxing towards equilibrium, showing a logarithmic relaxation behavior. The red dotted line is a fit obtained according to the MKT model. (d) Particles with different surface functionalization show similar logarithmic trajectories, but different relaxation rates. Reprinted and adapted by permission from Macmillan Publishers Ltd.: Nature Materials (Ref.⁵¹). Copyright (2012).

logarithmic trajectories for times greater than 10 ms over three decades (Fig. 2.4c). Particles with different surface functional groups show the same logarithmic behavior (Fig. 2.4d), providing similar values for surface defect areas in the order of a few nm^2 , but with different relaxation rates. In a follow up paper¹¹⁰ Wang *et al.* further investigate the nature of these defects, demonstrating that the contact line is pinned to topological defects rather than charged patches. Interestingly, they observed a fast relaxation behavior for PMMA particles approaching from the decane phase rather than from the water phase, showing the complex nature of wetting.

Chen *et al.*⁵² used a colloidal probe AFM to study the time-dependence and force of the early snap-in stage of a particle adsorbing to a water-air interface (Fig. 2.5a). Experiments were performed with silica particles of different radii, in a hydrophilic state as well as with a hydrophobic coating. The position of the interface and the snap-in time were determined by the deflection of the cantilever using a similar approach as Kaz *et al.*⁵¹

Chen *et al.* observed two relaxation timescales: a slow logarithmic relaxation for $t \sim s$ (Fig. 2.5b), in agreement with;⁵¹ and a fast relaxation for $t < ms$ (Fig. 2.5c). At this short timescale the fast adsorption is characterized by damped oscillations with the same frequency as the resonance frequency of the cantilever. The snap-in time, t_s , defined as the time for the particle to reach a steady position, was similar for both hydrophilic

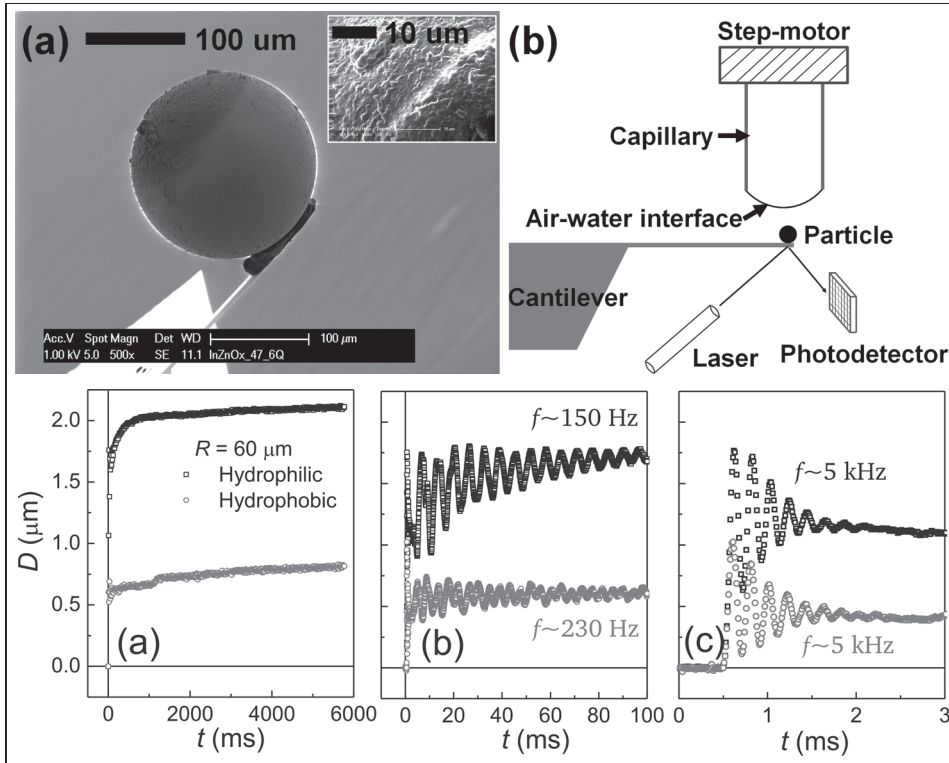


Figure 2.5: Study of the snap-in dynamics of a particle at a water-air interface using a colloidal probe AFM, as reported in Ref.⁵² (a, top) Scanning electron micrograph of a glass particle glued onto a cantilever and (b, top) schematic of the colloidal probe AFM setup. The probe approaches the interface and the deflection of the cantilever determines the particle surface-to-interface distance D . (a, bottom) Distance D versus time for a hydrophilic (black-squared dots) probe and a hydrophobic (gray-rounded dots) probe. At long time scales ($t = 0$ to $t = 6$ s) both curves show a slow logarithmic relaxation. (b, bottom). At intermediate time scales, damped oscillations are observed due to the excitation of capillary waves upon contact of the particle with the drop surface (c, bottom) At short time scales ($t = 0$ to $t = 3$ ms) a fast wetting process is observed, which is independent of particle wettability. Reprinted with permission from Ref.⁵² Copyright (2012), AIP Publishing LLC.

and hydrophobic particles. A characteristic timescale of the snap-in process can be obtained by considering the particle momentum change and capillary forces. This results in $\tau \sim (\rho_P R^3 / \gamma)^{1/2}$, where ρ_P and R are the density and the radius of the colloidal probe respectively. Measurements of t_s for particles with different radii and hydrophobicity confirmed this relation, proving that the snap-in time is dominated by inertia rather than particle wettability. As the authors pointed out, the scaling behavior is analogous to the initial spreading of droplets on flat surfaces,¹³⁵ where the early-stage spreading ($t \sim \mu\text{s}$) is dominated by inertia rather than surface wettability. From force measurements, Chen *et al.* estimated snap-in forces in the order of a few μN , with a linear relationship between the snap-in force and the radius of the colloid, which is larger for hydrophilic than for

hydrophobic particles.

2.5.2 Numerical techniques

Numerical studies relevant to dynamic wetting are very limited, but cover topics such as interface functionalization, the adsorption and desorption behavior of single particles at a fluid interface, capillary interactions between several (anisotropic) particles, or the impact of external fields on the structuring and movement of particles at interfaces.

An example for the functionalization of colloidal particles at a fluid interface is based on molecular dynamics simulations of Ehlinger *et al.*:¹⁵⁸ they demonstrate that hydrophobic colloidal particles can be placed crossing a lubricating gas layer between two liquid phases. Under a shear flow, these particles act as bearings and allow to substantially reduce the friction as compared to a pure fluid-fluid interface. Razavi *et al.*¹⁶⁷ also investigated the rotational dynamics of particles using molecular dynamics and their findings are particular relevant for the example of a possible measurement technique based on magnetic tweezers as provided in Chapter 5.

DeGraaf *et al.* presented a Langevin dynamics study¹⁶⁸ of adsorption trajectories and free energy separatrixes for colloidal particles with arbitrary shape. However, hydrodynamics is not included in the model. Günther extended these studies by lattice Boltzmann simulations of single ellipsoidal particles adsorbing to an interface and demonstrated that the deformability of the interface has an influence on the exact shape of the adsorption trajectories.^{162,166} Davies *et al.* on the contrary have studied in detail how an anisotropic particle detaches from an interface by dragging it off with a constant force. From such simulations a precise measurement of detachment energies is possible.¹⁶⁹

Joshi and Sun studied the dynamic wetting properties of evaporating droplets covered by particles using lattice Boltzmann simulations¹⁷⁰ and very recently Frijters *et al.* demonstrated that a dynamic change of contact angles in particle stabilized emulsions might be a possible route to the self-assembly of well-defined filters or catalysts.¹⁶²

Davies *et al.*^{76,171} studied the behavior of magnetic ellipsoidal particles under the influence of a magnetic field using the lattice Boltzmann method. The particles undergo a magnetic torque and deform the interface, leading to capillary interactions. They show a novel bottom-up method to facilitate self-assembly structure of ellipsoidal particles at the interface.

A relevant example for our discussion – that allows a direct comparison with the experimental results presented in^{51,52} – is provided by Colosqui *et al.*¹⁷² In this paper, the adsorption of a particle to a fluid–fluid interface is analyzed theoretically and by molecular dynamics simulations. The motion of the particle towards equilibrium is driven by the minimization of the surface free energy. The adsorption dynamics is modulated by introducing local energy minima and maxima in the potential energy landscape, expressed by

$$U(z) = U_S(z) + \frac{1}{2}\Delta U \sin(\lambda z + \phi) \quad (2.24)$$

where z is the center-to-interface distance, $U_S(z)$ is the interfacial free energy (eqn (2.19)), $(1/2)\Delta U$ is the amplitude of the perturbation, $l = 2\pi/\lambda$ is its wavelength and ϕ is a variable

phase. These perturbations (with $l \ll R$) are interpreted as microscale surface heterogeneities. The forward and backward hopping of the contact line from these metastable states is described with Kramers' theory.¹⁷³ The solution of the equation of motion is described by three independent physical quantities, that is, the characteristic hop length, the trajectory amplitude (determined by the initial separation from equilibrium position), and a characteristic hop time. The model predicts different relaxation regimes, from fast exponential relaxation – for a perfectly smooth $1 \mu\text{m}$ radius particle the decay time is $0.1 \mu\text{s}$ – to slow logarithmic or exponential relaxations in the vicinity of the equilibrium position, recovering the same behavior as for Kaz *et al.*⁵¹

As stated by the authors, their model based on Kramers' theory is mathematically similar to the MKT model presented in,⁵¹ and both can describe the slow logarithmic relaxation. The difference lies in the underlying physical assumptions. The MKT assumes that dissipative forces – determined by a characteristic hopping time over atomic sized defects – are driving the particle towards equilibrium, while Kramers' theory assumes that the driving force is related to a quasi-static process of surface minimization, determined by geometrical features on the particle surface. These findings demonstrate that the wetting dynamics of a particle adsorbing at a fluid-fluid interface is dominated by surface heterogeneities, but as for planar substrates, a consensus on the underlying physical mechanisms is still lacking.

2.6 Conclusions

In this Chapter we provided an overview of the basic concepts of particles at fluid-fluid interfaces. In particular, we focused on the description of the physics and the experimental and numerical approaches to study static and dynamic wetting of single particles at fluid interfaces.

The theory presented in this Chapter highlights the complexity of describing wetting phenomena, even for the classical study of a droplet on a planar substrate, where macroscopic effects are determined by the micro- and molecular scale interactions between the molecules of the fluids and of the solid substrate. To obtain such information scientists have developed techniques based on micro- and nanoparticles at fluid-fluid interfaces, where small scale effects are dominant and quantitatively observable. However, unlike many bulk colloidal suspensions in simple fluids that can be characterized in terms of electrostatic and van der Waals forces, the interactions of particles at fluid interfaces requires the addition of contributions due to discontinuities (e.g. density, viscosity, permittivity) and deformability of the interface. Electrostatic forces may extend over several particle diameters and interfacial deformations are responsible for non-trivial long-ranged inter-particle interactions that depend on how the interface was deformed (e.g. by gravity, particle shape or chemical surface properties, electro-dipping force). For micrometer spherical particles these forces typically range from a few fN to several pN or nN (see Table 2.1) and in general they depend on the interfacial tension, on the particle radius and three-phase contact angle. Although these parameters can be modulated by changing the materials and fluid compositions, it is often challenging to control each of them independently. For example, surfactants can be used to lower the surface tension of the

interface, which in turn may a change of the particle contact angle, hence the electrostatic and capillary interactions between particles. Moreover, the time-dependent adsorption of surfactants (or other macromolecules) may introduce ageing effects, with a variation on time of the particle properties and of the mechanical response of the interface.

Overall, this calls for the development of experimental methods able to control and disentangle the different contributions to the total interaction potential. To this aim scientists are following two approaches. The first one is focused on the production of particles with tailored properties, such as shape, size and surface functionalization. The second one is to develop experimental techniques able to disentangle the different forces, which represents the aim of the work summarized in this thesis.

Interfacial rheometry of polymer at a water-oil interface by intra-pair magnetophoresis

We describe an interfacial rheometry technique based on pairs of micrometer-sized magnetic particles at a fluid-fluid interface. The particles are repeatedly attracted and repelled by well-controlled magnetic dipole-dipole forces, so-called interfacial rheometry by Intra-Pair Magnetophoresis (IPM). From the forces ($\sim pN$), displacements ($\sim \mu m$) and velocities ($\sim \mu m/s$) of the particles we are able to quantify the interfacial drag coefficient of particles within a few seconds and over very long timescales. The use of local dipole-dipole forces makes the system insensitive to fluid flow and suited for simultaneously recording many particles in parallel over a long period of time. We apply IPM to study the time-dependent adsorption of an oil-soluble amino-modified silicone polymer at a water-oil interface using carboxylated magnetic particles. At low polymer concentration the carboxylated particles remain on the water side of the water-oil interface, while at high polymer concentrations the particles transit into the oil phase. Both conditions show a drag coefficient that does not depend on time. However, at intermediate polymer concentrations data show an increase of the interfacial drag coefficient as a function of time, with an increase over more than three orders of magnitude (10^{-7} to 10^{-4} Ns/m), pointing to a strong polymer-polymer interaction at the interface. The time-dependence of the interfacial drag appears to be highly sensitive to the polymer concentration and to the ionic strength of the aqueous phase. We foresee that IPM will be a very convenient technique to study fluid-fluid interfaces for a broad range of materials systems.^a

^aParts of this Chapter have been published as: S. Cappelli, A.M. de Jong, J. Baudry, and M.W.J. Prins, Interfacial rheometry of polymer at a water-oil interface by intra-pair magnetophoresis, *Soft Matter*, 12(25):5551-5562, 2016.

3.1 Introduction

Macromolecules, such as proteins, surfactants and nanoparticles, are known to strongly bind to and thereby modify fluid-fluid interfaces, with applications in food processing technologies for the stabilization of foams and emulsions,^{6,7} micro-encapsulation techniques for personal care¹⁰ and drug delivery,^{35,174} and in the creation of new functional materials based on self-assembly.^{11,31} Upon adsorption, the interface becomes crowded and the interaction between the adsorbed species strongly changes the mechanical properties of the fluid-fluid interface.^{7,25,44,48,175–179} Studies of these processes require rheometry techniques that are suited for small amounts of materials, small length scales, short and long timescales, and that are easy to use. Conventional interfacial rheometers have a limited sensitivity due to the size of the probes, typically millimeter or larger, and are not suited for biomedical research, where the amounts of material are generally limited and the relevant scales are well below the millimeter scale.^{26,56–58}

Microrheology refers to the use of micrometer-sized objects to measure interfacial shear viscosities on small length scales ($\sim \mu\text{m}$), small sample volumes ($\sim \mu\text{L}$), and with a high sensitivity.^{25,26,48,57–60} The sensitivity to the interfacial viscosity is expressed through the Boussinesq number Bo , which for a water-oil interface and a probe of characteristic dimension a can be expressed as:

$$\text{Bo} = \frac{\eta_S}{a(\eta_{\text{water}} + \eta_{\text{oil}})} \quad (3.1)$$

where η_S is the interfacial viscosity, η_{water} and η_{oil} are the bulk viscosities of water and oil respectively. If $\text{Bo} \gg 1$ the motion of the probe is decoupled from the hydrodynamics of the sub-phases and is dominated by the interfacial shear viscosity η_S . Microrheology can be divided in passive^{26,56,59,61} and active methods.^{62–67} In passive microrheology the Brownian motion of a probe is followed in time and is related to its diffusivity using a mean-squared displacement (MSD) analysis.²⁵ The accuracy of this method relies on the correct estimation of the drift (due to thermal convection, Marangoni effect, sample, etc.) that is superimposed on the thermally activated motion of particles. The drift can be corrected by subtracting the average motion of an ensemble of trajectories or by following the motion of a fixed reference object. For high viscosities ($\eta_S > 10^{-6}$ Ns/m) the static noise of the setup is generally comparable to the particle average displacement, and an incorrect estimation of the drift leads to systematically lower values for interfacial viscosities.²⁶ Two-particle microrheology overcomes these limitations by extracting the particle diffusivity from ensemble-averaged cross-correlated motion and inter-particle distances, which however requires a large amount of trajectories to be recorded.¹⁸⁰

In active microrheology external forces control the motion of the probes, such as generated with optical or magnetic tweezers. These forces allow one to reduce the number of probes required, to measure interfacial viscosities as high as $\eta_S \sim 10^{-4}$ Ns/m, and to reduce the measurement time to a few seconds, ideal to study time dependent phenomena. Optical tweezers have mainly been used to study the rheology of bulk fluids^{181–185} and in some cases also for fluid-fluid interfaces.^{186–188} The position of the probe is controlled with nanometer accuracy and it is possible to apply a wide range of forces. Mag-

netic tweezers have the advantage of low interference, because organic materials are fully permeable and insensitive to magnetic fields. With the use of micro-fabricated probes, such as magnetic nanowires and magnetic micro-buttons, magnetic tweezers have been successfully used to study the ageing of protein films^{62,65,66} and the shear viscosity of phospholipid and surfactant monolayers.^{64,67} The forced motion of a probe allows one to bring the system out of equilibrium and to explore many interesting and important material properties. However, the geometry of the probe and the dynamics of the actuation play an important role, as different rheological deformations such as dilatational and shear contributions might be coupled in one experiment. This makes the interpretation of data dependent on the material system under study, the conditions of the experiment and on assumptions of the hydrodynamic model used.^{26,55,68,69}

In this Chapter we describe an interfacial rheometry technique based on pairs of micrometer-sized magnetic particles that are repeatedly attracted and repelled by well-controlled magnetic dipole-dipole forces, so-called interfacial rheometry by Intra-Pair Magnetophoresis (IPM)¹⁸⁹ (Fig. 3.1a,b). From the forces, displacements and velocities of the particles one can quantify the interfacial drag coefficient within a few seconds and over very long timescales. This approach does not require microfabricated probes and operates with commercially available magnetic particles, which are nowadays available with a wide range of sizes, material and optical properties, and which can be easily functionalized to suit a wide range of applications.¹² The use of local dipole-dipole forces makes the method insensitive to fluid flow and suited for parallelization. Moreover, this method allows one to study proximity effects during particle separation and approach under different forces and shear rates.

We first validate the use of IPM for the measurement of viscous drag coefficients by comparing IPM data of particles in bulk water to data of Brownian motion analysis. Then, we study the dependence of interfacial drag on the adsorption of an amino-modified silicone polymer to a water-oil interface (Fig. 3.1c). Polyelectrolytes have a broad range of applications, such as for the production of microcapsules for biomedical applications,¹⁹⁰ food science,²³ and personal care products.¹⁰ In these systems, the time-dependent adsorption of polyelectrolytes to water-oil interfaces plays an important role in the production method and determines the final material properties.³⁵ At low polymer concentration the IPM particles remain mainly in the water side of the water-oil interface, while for high concentrations the particles transit into the oil phase (Fig. 3.1d). In both cases measurements show values of drag coefficients independent of time. However at intermediate polymer concentrations the data show an increase of the interfacial drag coefficient by several orders of magnitude as a function of time and of fluid composition.

3.2 Materials and methods

3.2.1 Materials

We use a silicone-based polymer functionalized with diamino-groups on the side chain (KF8004, provided as samples by Shin-Etsu Silicones Europe B.V.). The polymer is soluble only in the oil phase and concentrations are prepared by weighting the components. The radius of gyration of the polymer in oil was measured using dynamic light scatter-

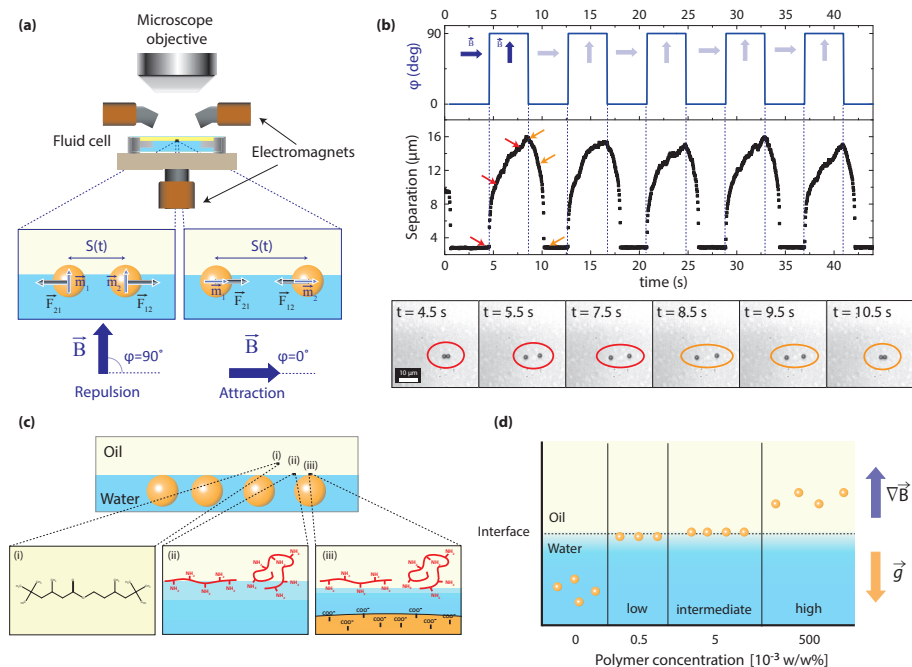


Figure 3.1: Principle of the Intra-Pair Magnetophoresis (IPM) experiment. **(a)** Pairs of particles are repelled and attracted by changing the orientation of the magnetic field φ generated by a set of electromagnets. Trajectories are recoded using a digital camera mounted on an optical microscope. **(b)** A typical IPM experiment consists of five repulsions and attractions. Center-to-center separation distance curves are extracted from the digital images (bottom). The drag is calculated by fitting the average of five repulsions to eqn (3.3). **(c)** Magnetic particles at a water-oil interface: oil-soluble amino-modified silicone polymer is dispersed in the oil phase (i) and adsorbs to the interface (ii). At the fluid-fluid interface, carboxylated magnetic particles (with negative charge) interact electrostatically with the amino-modified polymer (with positive charge) (iii). **(d)** Position of the particles as a function of polymer concentration c_p . Particles are brought into contact with the interface by means of magnetic field gradients. The particles sediment to the bottom of the fluid cell by gravitational forces when no polymer is present in the oil phase. The particles adsorb and retain a position in the interface when polymer is present at a low or intermediate concentration. The particles transit into the oil phase when polymer is present at a high concentration.

ing (DLS), which results in $R_G = 15 - 20$ nm. The oil phase is isononyl-isononanoate (Lanol 99, Seppic, $\eta_{oil} = 6$ mPa·s). The aqueous phase consists of phosphate buffered saline (PBS), prepared by dissolving PBS tablets (PBS tablets, pH 7.4, Sigma Aldrich) in 200 mL of ultra-pure water (resistivity > 18.2 M Ω ·cm) according to the supplier and then further diluted. All the components were used as received from the suppliers, without any further purification step.

We use carboxylic superparamagnetic particles (Dynabeads M-270 carboxylic acid, diameter $2R = (2.8 \pm 0.1)$ μ m, Life Technologies) as probes in all the experiments. In the presence of a magnetic field, the induced magnetization follows a Langevin function, with a particle-to-particle variation of magnetic susceptibility of about 8%.¹⁸⁹ Particles

were magnetically washed four times in ultra-pure water in order to remove surface-active elements present in the storage buffer, and were then dispersed in each corresponding buffer in a ratio 1 : 10000 from the stock solution.

3.2.2 Positioning of the particles at the interface

We create a flat water-oil interface using a custom made fluid cell (see Fig. 3.6) which consists of two circular aluminum rings. The outer ring, with a bottom hole to host a glass coverslide (19 mm diameter, Thermo ScientificTM), contains the inner ring with a central hole with sharp edges where the water phase pins. The oil phase is gently deposited on top of the water phase and the cell is closed with a glass coverslide (24 mm diameter, Thermo ScientificTM). The moment when the oil-water interface is formed sets the starting point for the reference time (adsorption time t_A) in our experiments. The whole system is held by capillary forces and we found the interface to be stable for several hours. Prior to any measurements all the fluid cell components (inner rings and glass cover slides) were washed in a sonic bath for 10 min first in acetone and then in isopropanol, ethanol (Sigma Aldrich), and finally in ultra-pure water.

After assembling the fluid cell, we bring the particles from the water phase to the interface by shortly applying a vertical magnetic force with a permanent magnet. After removing the magnet, the particles that are not trapped at the interface sediment to the bottom of the fluid cell. The microscope (Leica, DM6000 B) is equipped with a motorized stage that allows us to locate the position of the focal plane with micro-meter accuracy, thereby the position of the particles within the fluid cell. The concentration of particles is chosen in order to have a low surface coverage at the interface ($< 0.1\%$) so as to limit particle-particle interactions.

3.2.3 Particle tracking

We visualize the probes with a 40x magnification (0.40 N.A.) and acquire images with a high speed CMOS camera (MotionPro X3, Redlake) with a sampling rate of 30 frames per second. The trajectories of the particles are reconstructed from digital image analysis of consecutive frames with in-house written Matlab routines. Briefly, images (Fig. 3.1b bottom) are filtered with a low-pass Gaussian filter and corrected for the background. The particle center is determined using an algorithm based on the Hough transform, which looks for a set of pixels belonging to the same geometrical object, in our case a circle.⁸⁸ Other computationally more efficient strategies, such as cross-correlation or centroid tracking, cannot be used in this study as they fail to track objects that are in close proximity. Finally, the particle positions are correlated through consecutive frames using a Matlab implementation of the algorithm developed by Crocker and coworkers.^{87,191}

3.2.4 Interfacial rheometry by Intra-Pair Magnetophoresis (IPM)

Intra-Pair Magnetophoresis (IPM) was previously developed in our group to quantify distributions of the magnetic properties of superparamagnetic particles.¹⁸⁹ Here, we expand the use of IPM for rheometry studies of particles at fluid-fluid interfaces. We actuate magnetic particles by positioning the sample between a set of five electromagnets with soft iron cores, four of which are positioned above (normal to each other) and one below the

sample (Fig. 3.1a). The intensity and the direction of currents in the electromagnets (e.g. the magnetic fields) are controlled with a LabView interface that allows us to program any arbitrary actuation sequences (e.g. Fig. 3.1b). With this geometry we can apply magnetic fields with a magnitude between 0.1 and 50 mT.

When a superparamagnetic particle is exposed to a magnetic field it acquires a magnetic moment along the direction of the field, and a magnitude that scales with the field intensity, following approximately a Langevin function.¹⁸⁹ When two particles are in close proximity we can exploit their magnetic dipole-dipole interaction in order to induce magnetic attraction or repulsion (insets Fig. 3.1a). If we apply a field normal to the plane of the interface (out-of-plane), the force is repulsive and the center-to-center separation distance S increases. The motion of the particles is opposed by the hydrodynamic drag. In a material system with linear dependence of drag force on velocity, the following equations apply:

$$F_{dd} = \frac{3\mu_0 m_1 m_2}{4\pi S^4}, \quad F_{drag} = \frac{f}{2} \cdot \frac{dS}{dt} \quad (3.2)$$

where F_{dd} is the dipole-dipole induced magnetic repulsive force, μ_0 is the vacuum permeability, m_i is the magnitude of the induced magnetic moment (in units Am^2) for particle i , F_{drag} is the drag force and f is the hydrodynamic drag coefficient (in units Ns/m). Inertia can be neglected, since the Reynolds number (ratio between inertial and viscous forces) for the system under study is $Re \approx 10^{-6} \ll 1$.

The forces in eqn (3.2) define the equation of motion, and the solution of the differential equation yields

$$S(t)^5 = \frac{15\mu_0}{2\pi} \cdot \frac{m_1 m_2}{f} \cdot t + S_0^5 \quad (3.3)$$

where S_0 is the separation distance at time $t_0 = 0$. The repulsive magnetic force is always aligned with the inter-particle distance vector and does not depend on the orientation of the pair. If the magnetic field is now applied parallel to the interface (in-plane field, Fig. 3.1a) the resulting magnetic dipole-dipole force is attractive, with a solution that is of the same form as eqn (3.3) but has a different prefactor. This force depends on the relative orientation between the applied magnetic field and the inter-particle distance vector, but with the actuation protocol used in our experiments, the pair orientation hardly deviates from the field orientation (Fig. 3.1b, section 3.B). Details of the calculations can be found in reference.¹⁸⁹

A typical IPM experiment is shown in Fig. 3.1b. Particles are repeatedly attracted and repelled by changing the orientation of the magnetic field every 5 seconds, and images are acquired at a rate of 30 frames per second. The intra-pair separation distance S is extracted from digital image analysis (see previous section) and the drag coefficient is obtained by fitting the average of 5 curves with eqn (3.3). The drag coefficient is obtained by assuming a linear relationship between drag force and translational particle velocity, i.e. a Newtonian system. However, soft-matter systems can also exhibit non-linear properties. For example, polymer solutions can be viscoelastic, with a drag force that depends on the velocity history.^{53,54} The hydrodynamic properties of fluid-fluid interfaces may also depend on the type of adsorbed species.^{58,62} For the material system in this Chapter, we

find that the response is essentially linear, so that the motion of the particles is dominated by the linear shear response of the interface.

3.2.5 Interfacial rheometry by Mean-Squared Displacement (MSD)

The viscous drag of a fluid can be determined by the thermally activated motion of particle probes, i.e. Brownian motion.²⁵ From the trajectory of particles it is possible to calculate the diffusion coefficient D from the mean-squared displacement according to

$$\langle (r(t + \tau) - r(t))^2 \rangle = 2dD \cdot \tau \quad (3.4)$$

where $r(t)$ is the position of the particle at time t , τ is the lag time, d is the dimensionality of the system, and D is the diffusion coefficient of the particles. In our experiments the average is performed over all the particles in the field of view (usually between 5 and 20 particles) and lag times $0.03 \text{ s} < \tau < 10 \text{ s}$. Fits are performed for lag times $\tau < 2 \text{ s}$. We estimate the drift from the motion of the center of mass of the particle ensemble, according to the algorithm developed by V. Pelletier and coworkers.¹⁹²

The value of the drag coefficient can be determined from the Einstein relation:

$$D = \frac{k_B T}{f} \quad (3.5)$$

where k_B is the Boltzmann constant and T the absolute temperature. For a particle of radius R moving in a fluid with viscosity η , the drag coefficient reduces to the Stokes' drag $f = 6\pi\eta R$. Eqn (3.5) also holds for a particle at a fluid-fluid interface.^{25,26} The interfacial drag coefficient depends on the particle three-phase contact angle θ , the radius R , and the viscosities of the two phases and of the interface. The relation between the drag coefficient and the rheology of the interface depends on the material system under study, the assumptions of the hydrodynamic model used for the analysis,^{55,68,69} as well as on the actuation dynamics (e.g. rotation or translation) of the probe.⁶⁷

In this study we present data as the particle drag coefficient f extracted from fits of eqn (3.3) to the IPM trajectory data. In section 3.4.1 we will relate f to the rheology of the interface.

3.3 Results

In this section we present results as follows. We first measure and compare the drag coefficient of particles moving in bulk water with IPM and MSD analysis, thus proving the validity of the method. Then, we study how the polymer influences the position of particles at the water-oil interface and finally we apply IPM to study the adsorption of polymer at the interface for different fluid compositions. For clarity in presenting the results, we will express the polymer concentration in units of 10^{-3} w/w\% .

3.3.1 Drag measurements in water

In an IPM experiment particles are repeatedly brought in contact and then separated by several micrometers ($S \approx 3 - 16 \mu\text{m}$) by changing the orientation of the magnetic field (see Fig. 3.1b). Fig. 3.2a shows repeated magnetic repulsion curves for the same particle

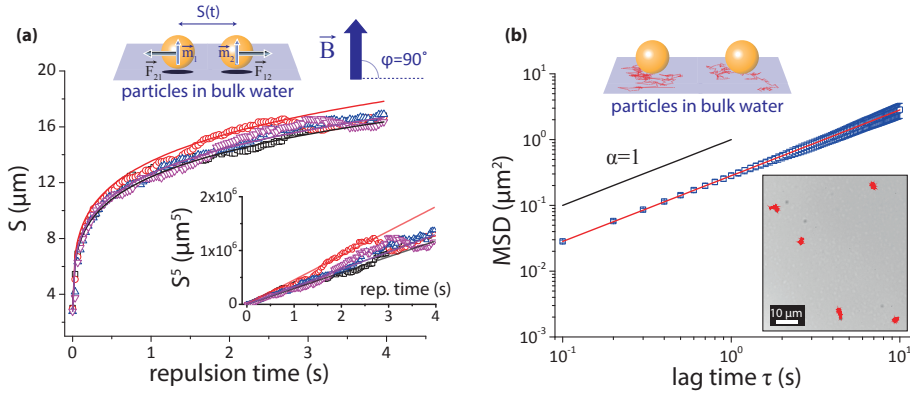


Figure 3.2: Particle motion data from Intra-Pair Magnetophoresis (IPM) and Brownian motion experiments, for particles in water near a solid substrate. **(a)** Center-to-center separation distance S as a function of magnetic repulsion time. Symbols and colours represent experimental data of four repulsion curves for the same pair of magnetic particles, with an average standard deviation between the measured points of about 3%. The solid lines represent fits according to eqn (3.3). The fitting routine is applied in the range $S < 10 \mu\text{m}$, because at higher separations Brownian fluctuations appear in the trajectories. The inset shows that S^5 scales linearly with repulsion time, in agreement with theory. The variation in slopes is less than 10%. **(b)** Mean-squared Displacement (MSD) of particle motion extracted from the average of 12 particles; the red line is the fit according to eqn (3.4) with a standard deviation of 0.2%. The inset shows an image with particles and superimposed trajectories.

pair, where the particles move in bulk water over a glass surface (so not yet for a system with an oil-water interface). At a separation distance in the order of a particle diameter, particles separate with initial speeds of a few tens of $\mu\text{m/s}$; at larger separations the velocity decreases due to the lower dipole-dipole force [cf $1/S^4$ in eqn (3.2)]. We limit the data range for our analysis to $S < 10 \mu\text{m}$, because at higher separations Brownian fluctuations appear in the trajectories. From the fit of every single curve according to eqn (3.3) we extract an average value for the drag coefficient of $f_{water}^{IPM} = (5.8 \pm 0.6) \cdot 10^{-8}$ Ns/m (weighted average over 15 curves \pm standard deviation). Plots of S^5 as a function of repulsion time (inset Fig. 3.2a) show the expected linear relationship for the motion of particles in a Newtonian fluid. Data obtained from attraction curves give similar results as the repulsion curves (data not shown).

Fig. 3.2b shows an MSD curve obtained from the trajectories of 12 particles undergoing Brownian motion. The red straight line is a fit according to eqn (3.4). The curve shows the expected linear behavior with slope $\alpha = 1$ as for the motion of a particle in a purely viscous fluid, with an accuracy of 0.2%. From the Stokes-Einstein relation (eqn (3.5)) we quantify the value of the drag coefficient from 9 measurements to be $f_{water}^{MSD} = (5.9 \pm 0.4) \cdot 10^{-8}$ Ns/m. This value is in agreement with IPM results within the experimental errors, confirming the consistency of the methods.

3.3.2 Particle position as a function of polymer concentration

Particles bind to the interface only when the polymer is present in the oil phase. Without any polymer, particles do not bind to the interface and sediment to the bottom of the fluid

cell. For high polymer concentrations ($c_P > 500 \cdot 10^{-3}$ w/w%) particles transit into the oil phase, which was proven by applying a vertical magnetic force after about 30 minutes and by observing that particles are able to reach the top glass of the fluid cell. For lower concentrations particles remained at the interface. These results show that it is possible to change particle wettability by varying the polymer concentration in the oil phase, as summarized in Fig. 3.1d.

3.3.3 Drag measurements at a water-oil interface

Here, we apply IPM to study the influence of the adsorption of polymer at a water-oil interface as a function of time and fluid composition. We will refer to the range of polymer concentrations as defined in Fig. 3.1d (low, intermediate, high). In Fig. 3.3a we show an example of IPM experiments for particles at a water-oil interface. Experiments were recorded at different polymer adsorption times of the interface. At $t_A = 251$ s (black symbols) particles separate tens of μm , with similar distances as compared to the motion of particles in bulk water (Fig. 3.2a). For longer polymer adsorption times, the inter-particle separation is reduced to a fraction of the particle diameter. The small error bars, represented as the standard deviation of 5 repeated repulsion trajectories, highlight the high reproducibility of IPM trajectories. In Fig. 3.3b we represent IPM trajectories as S^5 and perform fits according to eqn (3.3). The data show a linear relationship within the error bars for all times. The linear relationship is observed for all fluid compositions used in this study, proving the linear shear response of the interface to the motion of the probe. If there was a substantial nonlinear contribution to the force, the data would deviate significantly from eqn (3.3). Interestingly, for long polymer adsorption times and short repulsion times, we observe a very weak non-linearity (Fig. 3.3b, third panel), which will be discussed in section 3.4.1.

Low and high polymer concentrations.

Fig. 3.4 shows measurements of the drag coefficient f as a function of polymer adsorption time for low and high concentrations of polymer and for different ionic strengths of the water phase. Measurements obtained from the same particle pair (points connected by a dashed line in Fig. 3.4) show time independent values. Variations between values are observed from measurements on different pairs. All measured values are higher than the theoretical Stokes drag coefficient for the particles in their respective bulk fluids, as indicated by the dotted lines in Fig. 3.4. Results for a low and high polymer concentration yield an average drag coefficient of $f_{low} = (5.1 \pm 0.8) \cdot 10^{-8}$ Ns/m, and $f_{high} = (3.8 \pm 0.6) \cdot 10^{-7}$ Ns/m (for the aqueous phase with 150 mM PBS) respectively.

Intermediate polymer concentrations – high ionic strength.

Data in Fig. 3.5a show values for f as a function of polymer adsorption time for different initial polymer concentrations and a high salt concentration (150 mM PBS) in the aqueous phase. Data for $c_P = 1 \cdot 10^{-3}$ w/w% show first a constant value for f followed by a 100 fold increase over a timespan of a few hours (one time decade). For $c_P = 2 \cdot 10^{-3}$ w/w% the increase is a 1000 fold ($\sim 10^{-7} - 10^{-4}$ Ns/m) within a similar timespan. The time onset for the increase of f shifts towards lower adsorption times for higher initial

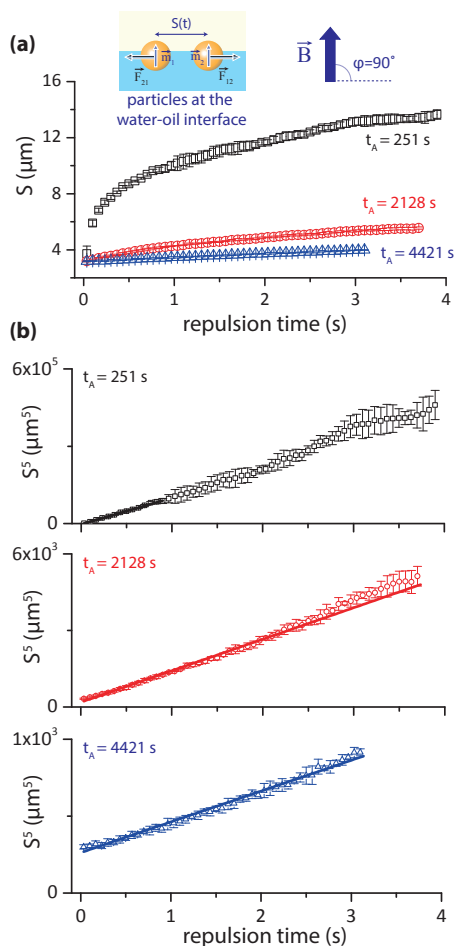


Figure 3.3: Particle motion data from intra-pair magnetophoresis (IPM) experiments, for particles at a water-oil interface. Experiments were performed for an aqueous solution with 150 mM PBS and a polymer concentration in the oil phase of $c_P = 2 \cdot 10^{-3}$ w/w%. **(a)** Center-to-center separation distance S as a function of magnetic repulsion time. Every curve is extracted from the average of 5 consecutive repulsion trajectories, with standard deviations as error bars. Every colour represents experiments recorded at different polymer adsorption times (t_A) of the interface. **(b)** Particle trajectories as S^5 (symbols) with fits (solid lines) according to eqn (3.3). The fitting routine is applied in the range $S < 10 \mu\text{m}$, because at higher separations Brownian fluctuations appear in the trajectories. All the curves are shown at a half of the sampling rate of the experiments (30 fps) for clarity.

polymer concentrations, with a similar rate of drag increase. Multiple points measured at the same polymer adsorption time represent data recorded on particle pairs located in the same field of view, with variations of drag coefficients within the experimental errors. Breaks between points, e.g. for $c_P = 1 \cdot 10^{-3}$ w/w% of Fig. 3.5a, are data recorded on different particle pairs located at different positions in the water-oil interface,

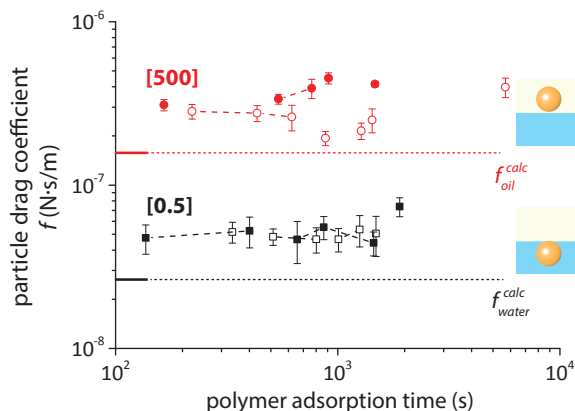


Figure 3.4: Particle interfacial drag coefficient f as a function of adsorption time of polymer at the oil-water interface, extracted from IPM analysis for low polymer concentration $[c_P]$ (black squares) and for high polymer concentration (red circles). The polymer concentration is expressed in units 10^{-3} w/w%. The aqueous solution contains 15 mM PBS (open symbols) or 150 mM PBS (solid symbols). The dotted lines represent the calculated Stokes drag of a particle in bulk water (black) or in bulk oil (red). For a low polymer concentration, the particles are attached to the interface but are situated mainly on the water side. For a high polymer concentration, particles transit to the oil side of the interface. Every measurement point is extracted from a fit according to eqn (3.3) for the average of 5 curves recorded on the same particle pair. Measurement points connected by a dashed line (guide to the eye) are recorded on the same particle pair. Error bars include fitting errors and a variation due to an uncertainty of magnetic susceptibility of 10 %.

showing a similar interface ageing. Drag coefficients extracted from magnetic attraction and repulsion trajectories show no significant differences (see section 3.B).

Intermediate polymer concentrations – low ionic strength.

Data (Fig. 3.5b) for a low salt concentration (20 mM PBS) in the aqueous phase show for all concentrations first a constant value of f followed by a time dependent increase. When comparing these results with the one obtained for a high ionic strength solution (Fig. 3.5a) we observe that the time onset for the drag coefficient increase occurs at higher adsorption times and within a narrower timespan. Moreover, the rate of increase for f strongly depends on the initial polymer concentration. In particular, for $c_P = 1 \cdot 10^{-3}$ w/w% parameter f increases by a factor of 2 in a time span of one decade, which is significantly lower than the 100 fold increase observed for the high ionic strength solution and same polymer concentration (Fig. 3.5a). For c_P equal to 3 and $4 \cdot 10^{-3}$ w/w%, we observe a similar 1000 fold increase. The variability between particle pairs is within the experimental errors.

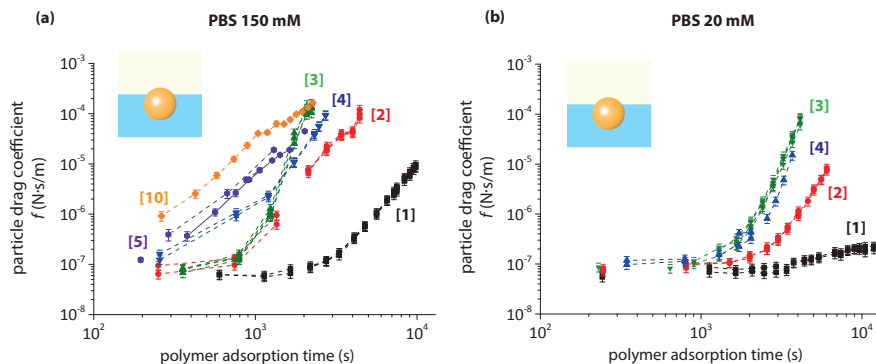


Figure 3.5: Particle interfacial drag coefficient f as a function of polymer adsorption time (t_A) for intermediate polymer concentrations $[c_P]$ expressed in units 10^{-3} w/w%. Panel (a) shows data for 150 mM PBS and panel (b) for 20 mM PBS in the aqueous phase. Every measurement point is extracted from a fit according to eqn (3.3) for the average of 5 curves of the same particle pair. Error bars include fitting errors and an uncertainty in the magnetic susceptibility of the particles of 10 %. Points connected by a dashed line (guide to the eye) are recorded on the same particle pair. Multiple points at the same polymer adsorption time represent data recorded on particle pairs in the same field of view, with a variability within the experimental errors.

3.4 Discussion

3.4.1 Rheometry by Intra-Pair Magnetophoresis

In an IPM experiment, pairs of micrometer-sized magnetic particles are repeatedly attracted and repelled by well-controlled magnetic dipole-dipole forces. From the forces (\sim pN), displacements (\sim μ m) and velocities (\sim μ m/s) of the particles we are able to quantify the interfacial viscous drag within a few seconds (\sim 5 s) and over long timescales (several hours), making this technique suitable to study time dependent phenomena such as the early stages of adsorption of macromolecules at a fluid-fluid interface as well as the aging of interfacial systems.

The size of the probe sets the sensitivity of the system to interfacial viscosities as low as $\eta_s = 7 \cdot 10^{-9}$ Ns/m [using $\eta_{water} = 1$ mPa·s, $\eta_{oil} = 6$ mPa·s, and $a \approx 1$ μ m, see eqn (3.1)], while the upper limit is determined mainly by the tracking accuracy of particles. For example, if we consider a magnetic field of 50 mT, a measurement time of 30 s and a particle displacement of 1 μ m, we can measure a drag coefficient $f \sim 10^{-3}$ Ns/m, which corresponds to interfacial viscosities in the order of $\eta_s \sim 10^{-3}$ Ns/m (for $\theta = 90^\circ$).⁶⁹ Our measurements show a dynamic range of about 4 orders of magnitude (Fig. 3.5), which is comparable to other active methods based on optical^{186–188} and magnetic tweezers^{62–67} experiments. An important advantage of IPM is that commercially available magnetic particles are used and that data can be acquired with high statistics by tracking many particle pairs simultaneously.

The accuracy of the drag coefficient determined by IPM is mainly determined by the uncertainty of the magnetic moment m of particles, which was measured to be about 8

% for the M-270 particles used in this study.¹⁸⁹ The hydrodynamic coupling between the particles¹⁹³ introduces a systematic error, which scales as $\sim 1/S$. Reenen *et al.*¹⁸⁹ performed numerical simulations of intra-pair motion on the very same particles of this study, showing that the hydrodynamic coupling leads to an underestimation of m of about 0.8 %. Here, for our experiments we consider a total uncertainty of magnetization of 10 %. The standard deviation from repeated measurement on the same pair (as shown in Fig. 3.2a) is less than 10 %, showing a good reproducibility of the method.

Superparamagnetic particles are known to have a small remanent magnetic moment.^{89,194} A change of the orientation of the magnetic field would exert a mechanical torque, which may introduce capillary dipolar interactions for particles at the water-oil interface.⁷¹ The maximum magnetic torque $\vec{\tau} = \vec{m} \times \vec{B}$ applicable on the particles of this study has been calculated by van Reenen *et al.*⁸⁹ to be $4 \cdot 10^{-18}$ Nm/rad (for a magnetic field of 36 mT). We used the results from Xie *et al.*¹⁴² to estimate the torque required to deform a fluid-fluid interface. The authors performed lattice Boltzmann simulations of capillary deformations for magnetic Janus particles at a fluid-fluid interface. In the limit of small interfacial deformations, the required torque to induce capillary deformation is $\sim 10^{-13}$ Nm/rad, which is much larger than the magnetic torque (see section 5.4.1 of Chapter 5). This proves that magnetically induced deformation of the interface are negligible.

IPM trajectories obtained for particles moving in water over a surface (Fig. 3.2a) are correctly described by eqn (3.3), which holds for a system with linear viscous behavior. The corresponding drag coefficient is about a factor of 2 higher than the calculated Stokes drag $f_{water}^{calc} = 2.6 \cdot 10^{-8}$ Ns/m for a particle in bulk water. We attribute the higher value to wall effects, as the effective viscosity increases when the distance to the surface becomes comparable to the particle radius.¹³⁶ According to the model by Leach *et al.*,¹⁹⁵ the correction factor for a particle translating over and touching a surface is 1.77. Data of f obtained from Brownian motion experiments give comparable results, proving the validity of IPM method to quantify the shear viscosity of fluids.

For further comparison, we recorded the drag coefficient at a water-oil interface using both IPM and MSD analysis. The resulting values of f are comparable only for a low polymer concentration and for short adsorption times (see Fig. 3.9 of section 3.B). For higher concentrations and longer adsorption times we measure systematically lower values from the MSD analysis. We attribute this discrepancy to an incorrect drift correction in MSD (Fig. 3.8). With the number of particles in the MSD measurement (4 to 20), a sufficient drift correction could not be achieved in the case of high interfacial viscosity. This is in agreement with the results showed by Samaniuk *et al.*,²⁶ where the authors demonstrated that for high interfacial viscosities (e.g. $\eta_S > 10^{-6}$ Ns/m) the diffusivity of particles becomes comparable to the static noise of the system, whose incorrect estimation leads to an apparent lower viscosity.

In active microrheology the geometry, the size of the probe (Boussinesq number) and the dynamics of the actuation (e.g. rotation and translation) play an important role. The deformation flow field of the interface potentially mixes different dynamic modes (e.g. shear and dilatation), thereby complicating the interpretation of the data into meaningful rheological quantities. This complication arises also from the lack of an analytical solution for the steady motion of a sphere in an ideal 2D fluid (Stokes' paradox), so one

must rely on numerical solutions. Danov *et al.*⁶⁸ modeled a fluid-fluid interface as a compressible 2D-fluid and solved numerically the Navier-Stokes equation to obtain the values of the drag coefficient f as a function of the particle contact angle, the dilatational and the shear viscosity of the interface. On the other hand, Fischer *et al.*⁶⁹ assumed that Marangoni forces were instantly compensated by the fast diffusion of macromolecules at the interface (e.g. surfactants), so that the interface behaves as 2D-incompressible. Therefore, care must be taken when interpreting experiments of translating probes at an interface, as an incompressibility of the dilute layer ($Bo \ll 1$) could contribute to the particle's drag increase, even for completely inviscid layers. This was studied by Zell *et al.*⁶⁷ using rotating magnetic micro-buttons to induce only surface shear to surfactant monolayers at an air-water interface. The authors demonstrated that the surfactants had no measurable surface shear viscosity, in contrast to results from translational studies.

From IPM experiments performed at the water-oil interface in the presence of polymer, we show that the response of the interface to the motion of the probe is essentially linear (Fig. 3.3), as expected for a purely viscous system as described by eqn (3.3). The observed increase of drag as a function of polymer adsorption time (Fig. 3.5) could in principle be caused by an increase of interfacial viscosity or interfacial incompressibility, as proposed by Fischer *et al.*⁶⁹ The polymer studied in this Chapter is a synthetic silicone polymer with random side chains, having in solution a 15 nm radius of gyration. When the polymer adsorbs at the interface, we expect polymer entanglement and reptation to play a role,^{46,58} which should generate dissipative effects upon actuation of a particle at the interface. Therefore, we attribute the polymer-dependent increase of drag coefficient to an increase of interfacial viscosity. However, we cannot exclude that also incompressibility effects play a role. This could be further investigated by comparing experiments of particle translation with particle rotation,⁸⁹ where only shear deformations are introduced at the interface.⁶⁷

Interestingly, for long polymer adsorption times we observed a very weak non-linearity at short separation distances (Fig. 3.3b). This may point to a non-linear response of the aged interface that depends on particle velocity or magnitude of the applied magnetic force, which could correspond to an increase of the elastic response or a shear thickening of the interface. We have analysed the non-linearity by a history dependent viscosity^{53,54} or by modelling the interface as a power-law fluid.⁶² However, it appeared that the non-linearity is too small to be able to extract meaningful non-Newtonian parameters from our experiment.

An interesting feature of IPM experiments is that data is generated in two different pair actuation modes, namely repulsion and attraction. In our measurements we did not observe any significant difference between drag values obtained by magnetic repulsion and magnetic attraction (section 3.B). Nonetheless, in a system with strong nonlinear effects, IPM may be used to compare the two perturbation modes of the interface, with emphasis on elongation in the case of particle separation, and compression in the case of particle attraction.

3.4.2 Particle position as a function of polymer concentration

In section 3.3.2 we observed that the position of particles with respect to the water-oil interface is modulated by the amount of polymer present in the oil phase. We interpret this change in particle wettability as an interplay between interfacial forces and electrostatic interaction between particles and polymers. The surface of the magnetic particles is functionalized with carboxylic groups and becomes negatively charged when immersed in a solution with a pH above the isoelectric point of the particles ($pI = 4.5$).¹⁹⁶ Dynamic surface tension measurements (data not shown) have shown that the surface tension decreases as a function of time and polymer concentrations, showing that the polymers adsorb at the interface also in the absence of magnetic particles. The very low solubility of the polymer in water causes only the amine groups to penetrate the interface into the water phase. There the polymer becomes positively charged, giving the possibility to interact electrostatically with the negatively charged magnetic particles.^{35,197} This electrostatic attraction is counterbalanced by interfacial forces that keep the particles at the fluid-fluid interface. Only at high concentrations of polymer the particles are able to transit into the oil phase. A similar result was obtained by Binks *et al.*,¹⁹⁸ who demonstrated that the wettability of silica nanoparticles can be tuned by changing the amount of cationic surfactant adsorbed on the surface of the nanoparticles, leading to a double inversion Pickering emulsion.

Measurements at low polymer concentrations (e.g. $c_P = 0.5 \cdot 10^{-3}$ w/w%) show values of f close to a particle diffusing in bulk water (Fig. 3.4). Here, we estimate the interfacial polymer concentration to be low (section 3.C) and we expect a weak interaction between the particles and the interface. During experiments we observed the detachment of particles from the interface. This can be explained only with a small value of the contact angle θ . The trapping energy of a particle at the interface is determined by the contributions of the surface free energies of the three phases (particle surface, water, oil) and can be calculated with the relation $\Delta E = -\pi R^2 \gamma \cdot (1 - |\cos \theta|)^2$,³⁰ where γ is the surface tension. A typical value for the maximum trapping energy is $\Delta E \approx 4.5 \cdot 10^7 k_B T$ (using $\gamma = 3 \cdot 10^{-2}$ N/m, $\theta = 90^\circ$), making the desorption process very unlikely. The electrostatic interaction between the polymer and the particle surface modulates the particle-oil surface free energy, i.e. the particle contact angle, and $\Delta E \approx k_B T$ only for $\theta < 1^\circ$. At this low polymer concentration the interfacial viscosity η_S can be expected to be low and the drag coefficient of the particle is dominated by the sub-phase viscosity ($Bo \ll 1$). In this regime, it is difficult to extract reliable interfacial viscosities, as changes of the particle contact angle would contribute to an apparent change in the interfacial viscosity, even for an inviscid interface.⁶⁷

For a high polymer concentration in the oil phase ($c_P = 500 \cdot 10^{-3}$ w/w%), the particles at the interface become densely coated with polymer and thereby become hydrophobic, which allows them to transit into the oil phase as confirmed by the drag measurements (Fig. 3.4). Values for f are a factor of two higher than the Stokes drag for a particle in the neat bulk oil ($f_{oil}^{calc} = 1.6 \cdot 10^{-7}$ Ns/m). This difference can be explained in a similar way as for the transport of a particle close to a surface, where the vicinity of the particle to the fluid interface has the effect of increasing the effective viscosity.¹³⁷ Moreover, the presence of polymer might increase the bulk oil viscosity. The measured drag coefficient

shows a higher variability as compared to measurements of particles trapped at the interface (lower polymer concentration); this may reflect variations in how a particle transits into the oil phase. We rule out that the particle crossing is the result of lowering the water-oil surface tension, as previously observed by Tsai and coworkers.¹²⁰ For a high concentration of polymer the surface tension decreases only by about a factor of 3 with respect to a pristine water-oil interface. This change would not be sufficient for the particles to cross the interface, even in the presence of a high magnetic force. For example, a force of 100 pN would result in a vertical displacement of an adsorbed particle by about 5 nm. Only for an ultra-low surface tension ($\approx 10^{-6}$ N/m) the interface crossing would be possible.¹²⁰ In summary, the drag measurements of Fig. 3.4 confirm the qualitative results found in section 3.2: for low concentrations particles are weakly bound to the interface and are more immersed in the water phase; for high concentrations particles can cross the interface and move into the oil phase.

For intermediate polymer concentrations we observe variations of interfacial drag coefficients over several orders of magnitude (Fig. 3.5). The drag coefficient of particles trapped at a fluid-fluid interface is influenced by the particle contact angle, which is unknown in our experiments. Aaron *et al.*¹⁹⁹ compared theoretical models and experiments of particle drag coefficients at a fluid-fluid interface. For a water-air interface with a viscosity ratio $\eta_{water}/\eta_{air} \approx 10^3$, a change of the particle contact angle between 0° and 90° gives a decrease of the particle drag coefficient of about 65%. In the case of nanoparticles at a water-alkane interface, Wang *et al.*²⁰⁰ showed that the drag coefficient increases for increasing viscosity of the alkanes, with an increase of about 60% for $\eta_{C16}/\eta_{water} \approx 3.5$. In our system the viscosity ratio is $\eta_{oil}/\eta_{water} \approx 6$, so we expect that a change of contact angle would give only a small change of drag. Therefore, the variation over several orders of magnitude that we observe for the interfacial drag coefficients, is dominated by changes of interfacial viscosity ($Bo \gg 1$) rather than changes of the particle contact angle. The high sensitivity to interfacial viscosity is in agreement with the large value of the Boussinesq number in our system (eqn (3.1)).

3.4.3 Adsorption of polymers to the interface

The adsorption of macromolecules to a fluid-fluid interface involves a two-step process: diffusive transport from the bulk fluid of one of the two phases to the proximity of the interface, and thereafter a molecular adsorption process that may be influenced by an energy barrier, such as an electrostatic barrier for charged species, or a steric barrier due to the presence of already adsorbed molecules.^{44,175} At short times, $t \rightarrow 0$, polymers adsorb to a pristine interface without steric hindrance. In absence of an energy barrier for adsorption, the surface coverage Γ (mol/m²) can be estimated using the Ward-Tordai equation.²⁰¹

$$\Gamma(t) = 2c_P \sqrt{\frac{Dt}{\pi}} \quad (3.6)$$

For concentrations below the overlap concentration c^* ,²⁰² the diffusion constant D can be estimated by assuming the polymer to be a sphere of radius R_G (see section 4.2.1). The results in Fig. 3.4 for low c_P and short adsorption times indicate that the interface

is in the dilute regime²⁰³ and that the amount of polymer is not sufficient to change the mobility of the particles (section 3.C). Graham *et al.*¹⁷⁶ showed that for protein adsorbing to a water-air interface eqn (3.6) is valid for a relative surface coverage of $\Gamma_R < 10\%$. A similar conclusion has been reported for the early stages of adsorption of polymers at a water-air interface¹⁷⁵ and for polymer-functionalized nanoparticles at a water-n-Decane interface measured with pendant-drop tensiometry.¹⁷⁸

At long times the adsorption rate is lowered due to the presence of only few remaining adsorption sites in the interfacial monolayer and eqn (3.6) is not valid anymore. Here, the interactions between the adsorbed polymers (e.g. hydrogen bonding, hydrophobic or electrostatic interactions) can contribute to an increase of the interfacial viscosity.⁷ This is shown in our experiments for intermediate polymer concentrations (Fig. 3.5a), where the drag coefficient of particles at the interface increases over several orders of magnitude in a timespan of a few hours. The time onset for drag increase shifts towards shorter adsorption times for increasing initial polymer concentration in the oil phase, which is consistent with a higher diffusive flux of polymer to the interface (section 3.C). Data recorded on different particle pairs within the same field of view show variabilities within the experimental error. Data recorded on particle pairs located at different positions of the water-oil interface show a similar increasing rate of drag, suggesting a homogeneous interface ageing. Moreover, this increase is similar for all concentrations, following a power-law relationship. A similar behavior was observed by Maestro *et al.*,⁵⁸ where they studied the interfacial viscosity of poly(*tert*-butyl-acrylate) of different molecular weights at a water-air interface using passive microrheology. They showed that the interfacial viscosity follows a power-law increase as a function of surface concentration ($\eta_s \sim \Gamma^\beta$), with increasing values of β for polymers with a higher molecular weight. This reasoning cannot be directly applied to our data, as measurements were not performed at equilibrium. Nonetheless, under certain assumptions (section 3.D) we estimate an exponent that suggests a strong polymer-polymer interaction at the interface. This is also confirmed by the observed increase of drag coefficient over several orders of magnitude in a short time span.

The kinetics of polymer adsorption and interface ageing are influenced by the ionic strength of the water phase, as shown in Fig. 3.5b. A low ionic strength in the aqueous phase may enhance the electrostatic interaction of the polymers at the fluid-fluid interface due to unscreened charges of the amine groups exposed to the water phase.³⁵ The enhanced electrostatic interaction may favor a stretched conformation of the polymer at the interface, increasing repulsion between polymer chains, and thereby lowering the probability for further polymer adsorption.²⁰⁴ This is suggested by a significantly lower increase of drag coefficient for $c_P = 1 \cdot 10^{-3}$ w/w% as compared to a high salt concentration (Fig 3.5a). Moreover, the time onset for the increase of the drag coefficient for c_P equal to 2, 3 and $4 \cdot 10^{-3}$ w/w% is shifted towards longer adsorption times, indicating slower adsorption kinetics. The increase of drag coefficients spans a similar dynamic range as compared to a high ionic strength solution, with a similar rate of increase. The dependency on the initial polymer concentration suggests a non-equilibrium interface ageing, where the evolution of the interface is determined by the early stages of polymer adsorption.⁴⁵

3.5 Conclusions

We have presented an interfacial rheometry technique wherein pairs of micrometer-sized magnetic particles are repeatedly attracted and repelled by well-controlled magnetic dipole-dipole interactions, so-called interfacial rheometry by Intra-Pair Magnetophoresis. We have validated the technique first by measuring particle drag coefficients in bulk water and by comparing the results to Brownian motion analysis, showing a good agreement between both methods. Thereafter we applied IPM to quantify interfacial drag in a material system with adsorption of an amino-modified polymer to a water-oil interface. In absence of polymer in the oil phase, the particles stay in the water phase and do not attach to the fluid-fluid interface. For high polymer concentrations, the particles transit into the oil phase due to polymer binding to the particles by electrostatic interactions. For intermediate polymer concentration, the particles remain in the fluid-fluid interface and experience a drag that depends strongly on polymer concentration, on time, and on the ionic strength of the aqueous phase. Measurements as a function of polymer adsorption time show an increase of interfacial drag by more than three orders of magnitude over a timespan of a few hours, suggesting a strong polymer-polymer interaction at the interface.

The IPM experiments show that the hydrodynamic response of the interface in the presence of adsorbed polymer is essentially Newtonian. Interestingly, a very small deviation appeared for long polymer adsorption times and small particle separations, which may point to a weak nonlinear response of the interface. In our experiment large displacement amplitudes were used, which might influence elastic structures in the system.⁶⁴ To study the viscoelastic response at weak perturbation, the IPM technique may be applied with small amplitudes, e.g. by imposing onto the particles an oscillatory motion with amplitudes of only tens of nanometers and frequencies of tens of Hz. For further study, it may be interesting to look at possible differences between separation and attraction, where differences due to interface elongation and compression may be revealed. Also it would be interesting to apply IPM to other materials systems, such as albumin⁶⁵ or lysozyme⁶² at an air-water interface, or particle laden fluid interfaces.²⁵ Finally, the application of higher magnetic forces (e.g. with stronger magnetic fields or particles with a higher magnetic content) may more deeply reveal non-linear responses of the interface.

The sensitivity of the IPM method, the short time required for recording a single measurement point, the relatively simple instrumentation that is needed, the possibility to follow simultaneously many particles over a long period of time, and the fact that commercially available particles can be used as probes, make IPM a very versatile method to study interfacial viscosity in a wide variety of soft-matter materials applications.

3.A Design of the fluid cell

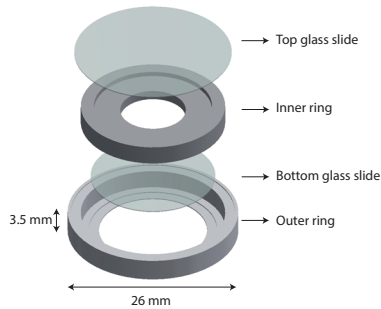


Figure 3.6: Exploded view of the fluid cell used to create a flat water-oil interface.

3.B Comparison between attraction and repulsion curves of Intra-Pair Magnetophoresis experiments

In an Intra-Pair Magnetophoresis (IPM) experiment the value of the drag coefficient f of particles can be extracted by fitting magnetic repulsion curves (Fig. 3.2a and Fig. 3.3a). In the data analysis, eqn (3.2) can be used for a system with linear dependence of drag and velocity. In repulsion experiments, the external magnetic field and the induced magnetic dipole moments of the particles are normal with respect to the plane of the interface (out-of-plane). The resulting force is always directed along the inter-particle separation distance vector, so that the force does not depend on the pair orientation.

For experiments of magnetic attraction, the external magnetic field and the induced magnetic dipole moments of the particles are parallel with respect to the plane of the interface (in-plane). The resulting force is attractive and depends on the relative orientation of the magnetic field and the inter-particle distance vector. The attractive force tends to align the particle pair with the magnetic field. Already at large inter-particle separation, the component of the magnetic force normal to the inter-particle distance vector causes alignment of the particles along the direction of the applied magnetic field. While this

normal component vanishes, the component along the inter-particle distance vector increases. Due to the timescale of the experiment, we found only very small fluctuations in the pair orientation with respect to the direction of the in-plane magnetic field (Fig. 3.1b), so that we can neglect pair orientation in our analysis. Therefore, the drag coefficient of particles can be extracted from attraction curves using the equation:

$$S(t)^5 = S_0^5 - \frac{15\mu_0}{\pi} \cdot \frac{m_1 m_2}{f} \cdot t \quad (3.7)$$

where S is the particle center-to-center separation distance, μ_0 the vacuum permeability, m_i the induced magnetization of particle i , and S_0 the separation distance at time $t_0 = 0$. Details for the calculation of eqn (3.7) can be found in reference.¹⁸⁹

Fig. 3.7 shows values of drag coefficients extracted from magnetic repulsion and attraction curves as a function of polymer adsorption to the water-oil interface and ionic strength of the aqueous phase. For all conditions the data show no significant differences between the two approaches.

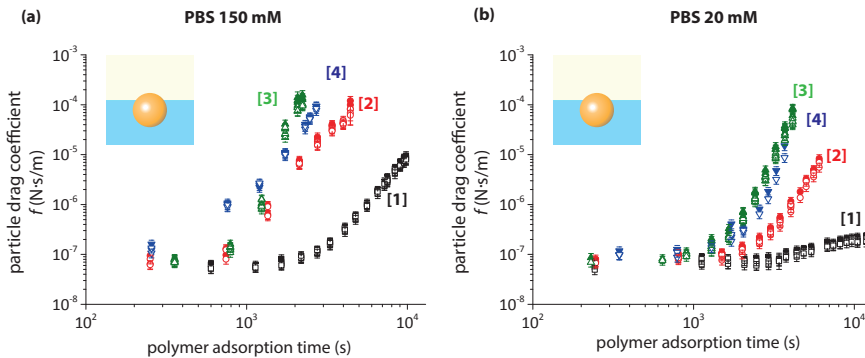


Figure 3.7: Comparison between interfacial drag coefficient f of particles at a water-oil interface as a function of polymer adsorption time obtained from magnetic repulsions (solid symbols) and attractions (open symbols) of IPM experiments. Polymer concentrations $[c_p]$ are expressed in units of 10^{-3} w/w%. Panel (a) shows data for 150 mM PBS and panel (b) for 20 mM PBS in the aqueous phase. Every measurement point is extracted from a fit according to eqn (3.3) and eqn (3.7) for the average of 5 curves of the same particle pair. Error bars include fitting errors and an uncertainty of the induced magnetization of 10%.

3.C Comparison between Intra-Pair Magnetophoresis and Brownian motion experiments

During the time-dependent experiments of polymer adsorption to a water-oil interface, we quantified the particle interfacial drag with both IPM and Brownian motion (BM) methods. Trajectories were acquired for 30 s with a sampling rate of 30 Hz. From the motion of the center of mass of the particle ensemble we estimate the drift of particles superimposed on the Brownian motion. This is performed according to the algorithm developed by V.

Pelletier *et al.*¹⁹² (algorithm available at: <http://people.umass.edu/kilfoil/downloads.html>).

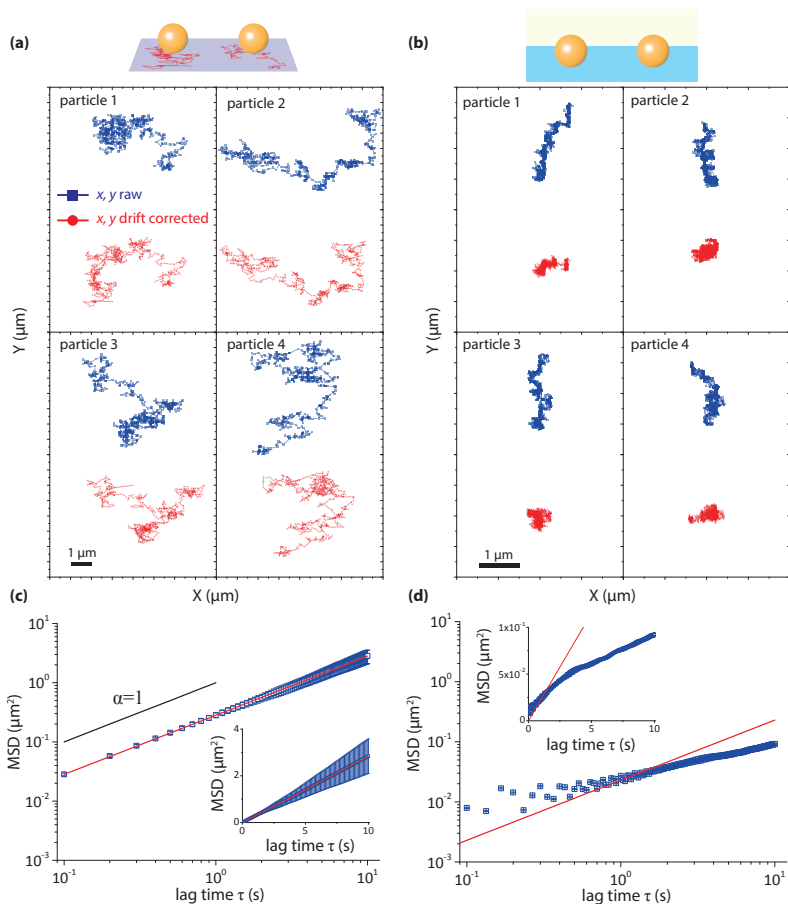


Figure 3.8: Particle motion data from Brownian motion experiments. Panels (a) and (b) show examples of raw trajectories (blue squares) and drift corrected trajectories (red circles) of particles moving in bulk water over a glass substrate and at the water-oil interface respectively. In panel (c) we reproduce for convenience Fig. 3.2b, the MSD curve of the average of 12 particles diffusing in bulk water over a glass surface. Panel (d) shows the MSD curve of the average of 4 particles diffusing at a water-oil interface (150 mM PBS, $c_p = 1 \cdot 10^{-3}$ w/w%, $t_A = 7736$ s). In (c) the fit of the MSD curve (red line) follows the expected behaviour according to eqn (3.4), while in (d) artifacts due to a poor drift correction lead to a deviation from eqn (3.4).

Fig. 3.8a,b show examples of raw x, y trajectories (blue squares) and drift-corrected trajectories (red circles) for different particles in bulk water on a glass surface (Fig. 3.8a) and at the water-oil interface (Fig. 3.8b). The corrected trajectories are then used to construct MSD curves and to extract the drag coefficient of particles, as explained in

section 3.2.5. Results for particles moving in bulk water over a glass surface (Fig. 3.8c) show the expected linear relationship according to eqn (3.4) (red line in Fig. 3.8c). An incorrect estimate of the drift may introduce artifacts that lead to an incorrect estimation of the drag coefficient, as shown in Fig. 3.8d for particles at a water-oil interface (details of fluid composition in the figure caption). According to eqn (3.4), an MSD curve should start from the origin for $\tau = 0$ and then increase linearly ($\alpha = 1$) for a purely viscous fluid, or sub-linearly ($\alpha < 1$) for a visco-elastic fluid. In this example it is clear that the former condition is not satisfied and it is not possible to correctly estimate the drag coefficient (see inset of Fig.3.8d, red line).

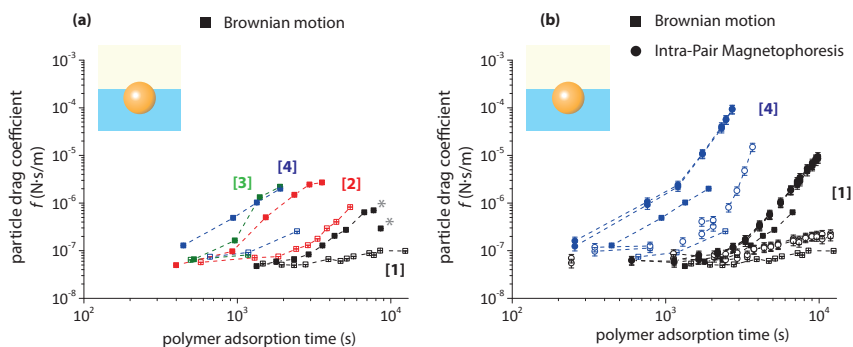


Figure 3.9: **(a)** Particle interfacial drag coefficient f as a function of polymers adsorption time at the water-oil interface extracted from Brownian motion experiments for different polymer concentrations [c_P] (expressed in units 10^{-3} w/w%). Experiments are performed for an aqueous solution containing 150mM PBS (solid symbols) and 20mM PBS (open symbols). Symbols marked with an asterisk represent data with artifacts (Fig. 3.8d). **(b)** Comparison between drag coefficients of particles extracted from BM and IPM experiments performed on the same sample.

We extract the particle drag coefficients from the linear part of MSD curves ($\tau < 2s$). Results in Fig.3.9a are obtained for an aqueous solution with 150 mM PBS (solid symbols) and 20 mM PBS (open symbols). Points marked with a gray asterisk are data that show an incorrect MSD curve, as shown in Fig.3.8d. In Figure 3.9b we directly compare data obtained from IPM and BM experiments for high and low salt concentration, and c_P equal to 1 and $4 \cdot 10^{-3}$ w/w%. For low polymer concentrations and short adsorption times both data agree quantitatively, while for longer times and concentrations BM experiments show systematically lower values. A possible explanation for this discrepancy is the introduction of artifacts due to a poor drift correction, as a limited number of particles was used to construct the MSD curves (between 4 and 20).

In literature other examples can be found where Brownian motion experiments show systematically lower values as compared to active methods. Lee *et al.* studied the protein layer formation at a water-air interface with passive (BM) and active (magnetic nanowire microrheology) methods.⁶⁶ Both approaches show an increase of interfacial viscosity over a few orders of magnitude, with systematically lower values of interfacial viscosity for passive microrheology. They excluded a possible depletion effect in the vicinity of the

probes by probing the correlated motion of particles over longer length scales (3 - 30 μm) using two-particle microrheology.¹⁸⁰ As an alternative explanation, the authors proposed that the increasing layer thickness for longer times might lower the contact angle of the adsorbed probes, thereby probing a less compact underlayer. Samaniuck *et al.*,²⁶ studying interfacial viscosities of monolayers of different polymers at a water-air interface with macro- and (passive) micro-rheology, showed several experimental artifacts that result in an underestimation of interfacial viscosities, such as tracking particles in the immediate vicinity of the interface, large scale heterogeneities of the layer, and the influence of the static noise of the experimental setup. The latter one may become comparable to the average squared displacement of particles for high viscosities, e.g. $\eta_S > 10^{-6}$ Ns/m, and an incorrect estimation of the drift leads to lower values for interfacial viscosities. In IPM experiments, the use of spatially localized forces makes the method insensitive to the drift of particles and suited for the study of systems with high viscosities, where BM experiments have been shown to provide incorrect results.

3.D Interfacial concentration of polymers at a water-oil interface

In this section we estimate the surface density of polymers at the water-oil interface. When the water-oil interface is formed, polymers diffuse to and adsorb to a pristine interface. In absence of an energy barrier for adsorption and steric hinderance, the surface coverage Γ (mol/m^2) as a function of time t can be estimated using the Ward-Tordai equation:²⁰¹

$$\Gamma(t) = 2c_b \sqrt{\frac{D \cdot t}{\pi}}, \quad (3.8)$$

where c_b is the molar concentration (mol/m^3) of polymer in the oil phase, and D is the diffusion coefficient of the polymer. For concentrations below the overlap concentration c^* ,²⁰² the diffusion constant D can be estimated using Einstein's relation (eqn (3.5)) by assuming the polymer to be a sphere of radius R_G , the measured radius of gyration. The molecular weight M_W of the polymer of this study is not known. If we assume a $M_W = 5$ kDa, this corresponds to $c^* = 2.5 \cdot 10^{-7}$ g/ mm^3 . For a polymer concentration of $c_P = 10 \cdot 10^{-3}$ w/w% the overlap concentration is $c_P^* = 8.5 \cdot 10^{-8}$ g/ mm^3 , which is smaller than c^* . Since c^* increases linearly with M_W , for $c_P \leq 10 \cdot 10^{-3}$ w/w% the polymer solution is always in the dilute regime.

It is possible to estimate the surface coverage Γ without knowing the molecular weight of the polymer. To do so, we assume that the area occupied by an adsorbed polymer at the interface is:

$$a_p = l_p \cdot h_p = N l_m \cdot h_m, \quad (3.9)$$

where l_p and h_p are the length and height of the polymer respectively, l_m and h_m the length and height of the N monomers respectively. With this ansatz, we can estimate the maximum number of polymers that geometrically fits the interface:

$$N_P^{max} = \frac{A_{int}}{a_p}, \quad (3.10)$$

where A_{int} is the surface of the interface according the geometry of the fluid cell (Fig. 4.5). The term that we still need to estimate in eqn 3.8 is the bulk polymer concentration c_b . In our experiments we measure the concentrations as weight percentage w_p (w/w%), so we can express the polymer concentration as

$$c_p = \frac{w_p \cdot \rho_{oil}}{100} \cdot \frac{1}{M_W^p}, \quad (3.11)$$

where ρ_{oil} is the density of the oil and M_W^p is the (unknown) molecular weight of the polymer. Since $M_W^p = N \cdot m_m$, with m_m the mass of a monomer, and combining the eqn (3.8 - 3.11) we can calculate the relative surface coverage Γ_R (expressed as a ratio) as:

$$\Gamma_R(t) = \frac{\Gamma \cdot A_{int}}{N_p^{max}} = \frac{w_p \rho_{oil}}{50} \cdot \frac{l_m h_m}{m_m} \left(\frac{Dt}{\pi} \right)^{\frac{1}{2}} \quad (3.12)$$

which is independent of the molecular weight of the polymer.

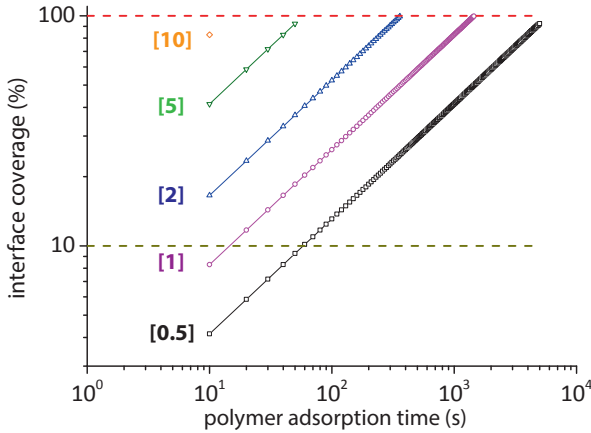


Figure 3.10: Relative interfacial concentration of polymer at a water-oil interface as a function of polymer adsorption time computed using eqn (3.12) for different initial concentrations of polymers c_p (expressed in units 10^{-3} w/w%). Calculations are performed using $\rho_{oil} = 0.85$ g/cm³, $l_m = 3.11$ Å, $h_m = 7$ Å, $m_m = 74.15$ Da, and $D = 2.4$ μm²/s.

In Fig. 3.10 we show calculations according eqn (3.12) with the concentrations that were used in our experiments. For $c_p = 0.5 \cdot 10^{-3}$ w/w% we expect an interfacial concentration of about 40% at the adsorption time $t_A = 1000$ s. Experimental results in the same conditions show values of interfacial drag coefficients that do not depend on time (Fig. 3.3), in agreement with the calculated sub-monolayer polymer density at the interface. For $c_p = 1 \cdot 10^{-3}$ w/w% the expected interfacial coverage at $t_A = 1000$ s is expected to approach a full monolayer. Here, the experimental results show first a constant value of drag coefficients, followed by an increase over several orders of magnitudes (Fig. 3.5a).

The onset of interfacial drag increase observed in the experiments for the different polymer concentrations seems to be in agreement with a very rough model based on polymer diffusion towards the interface.

3.E Interface ageing

Data for intermediate polymer concentrations (Fig. 3.5) show a power-law increase of particle interfacial drag, with $f \sim t_A^{\beta'}$. A similar relationship was observed by Maestro *et al.* from the study of interfacial viscosity of poly(*tert*-butyl-acrylate) of different molecular weights at a water-air interface using passive microrheology.⁵⁸ The authors measured a power-law increase of interfacial viscosity η_s as a function of surface concentration Γ ($\eta_s \sim \Gamma^\beta$), with increasing values of β for polymers with higher molecular weights.

The adsorption time t_A can be related to Γ via eqn (3.8) in case of diffusion limited transport. To test the validity of eqn (3.8), we plot $\log(t^*)$ as a function of $\log(c_P)$, where t^* is the adsorption time for a fixed value of the drag coefficient f . For a diffusion limited adsorption process, eqn (3.8) predicts a slope equal to -2. This condition is satisfied only for $c_P \leq 2 \cdot 10^{-3}$ w/w%, as shown in Fig.3.11 (solid lines). According to Fischer's model, the drag of a particle straddling a fluid-fluid interface can be expressed in a first order approximation as a linear function of the interfacial viscosity η_s .⁶⁹ Hence, $\beta = 2\beta'$ and we obtain $\beta = 7.4 \pm 0.1$ and $\beta = 7.6 \pm 0.2$ for c_P equal to 1 and $2 \cdot 10^{-3}$ w/w% respectively. Although these measurements were not performed at equilibrium, the results are in the correct order of magnitude with the expected maximum scaling of $\eta_s \sim \Gamma^6$,^{46,58,203} suggesting a strong polymer-polymer interaction at the interface. This is also confirmed by the observed increase of drag coefficient over several orders of magnitude in a short timespan.

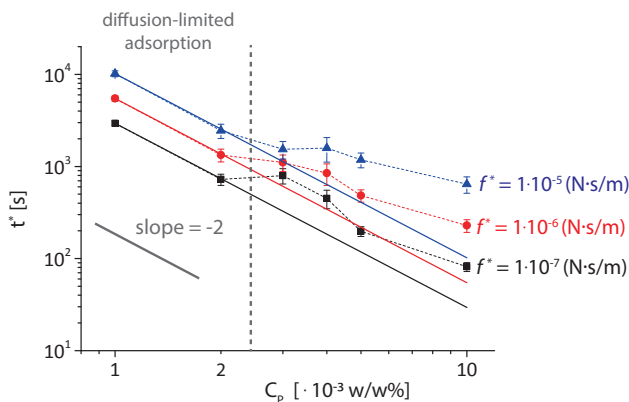


Figure 3.11: Time for drag increase in case of a diffusion-limited model for the adsorption of polymer at a water-oil interface. The values for t^* are extracted from a linear fit of the power-law increase of Fig. 3.5a for a fixed value of the drag coefficient f^* . Error bars are determined from the fit. Solid lines represent the expected relationship for a diffusion limited adsorption as described by eqn (3.8).

Inter-particle capillary forces at a fluid-fluid interface with strong polymer-induced ageing

We report on the forces between spherical magnetic particles adsorbed at a water-oil interface in the presence of polymer. The role of the polymer is twofold. First, the cationic polymer interacts electrostatically with the negatively charged particles, thereby modulating the particle contact angle and the magnitude of capillary attraction between the particles. Second, polymer adsorption to the interface generates an increase of the interfacial viscosity, over several orders of magnitude in a timespan of a few hours. An important challenge is to disentangle the conservative inter-particle forces from dissipative effects caused by interfacial ageing. We have designed an experiment in which well-controlled inter-particle magnetic forces are applied (\sim pN) and repeated motion trajectories are measured on pairs of particles. The experiment gives an independent quantification of the interfacial drag coefficient ($10^{-7} \sim 10^{-4}$ Ns/m) and can reveal correlations with non-viscous attractive inter-particle forces (0.1 \sim 10 pN) in the system. We observed that the attractive force depends on the initial amount of polymer in the oil phase and on the particle pair. However for a given particle pair the attraction appears to be independent of the interfacial viscosity, with changes over a wide range of viscosity values due to ageing. Given the direction (attraction), the range (\sim μ m) and the distance dependence ($\sim 1/S^5$) of the observed inter-particle force, we interpret the force as being caused by quadrupolar deformations of the fluid-fluid interface induced by particle surface roughness. The results suggest that capillary forces are equilibrated at the early stages of interfacial ageing and thereafter do not change anymore with strong changes of interfacial viscosity. Our approach may be useful to study the microrheology and the aggregation kinetics of the self-organization of micro- and nano-particles at fluid-fluid interfaces for systems out of equilibrium.^a

^aParts of this Chapter have been submitted as: S. Cappelli, A.M. de Jong, J. Baudry, and M.W.J. Prins, Inter-particle capillary forces at a fluid-fluid interface with strong polymer-induced ageing.

4.1 Introduction

Scientists are seeking new routes for the production of materials with novel optical, thermal, electrical and/or mechanical properties. An attractive approach is to organize micro- and nanoparticles into 2D ordered structures, where the properties on macroscopic length scales depend on the materials, the shape, and the spatial dimensions between the particles. This approach has already been used for the improvement of solar cells efficiency,³³ for the fabrication of anti-reflective coatings²⁰⁵ and ultrathin membranes.²⁰⁶ Particles can be assembled with nanometer accuracy using top-down approaches, such as electron-beam lithography and focused ion-beam milling. However, true applications demand for a large-area production, inexpensive and scalable techniques. A promising alternative is to use bottom-up approaches based on self-assembly,^{42, 207, 208} such as the self-assembly of colloidal particles at fluid-fluid interfaces. The strong adsorption energy ($\gg k_B T$),³⁰ makes the interface an ideal plane where particles can laterally diffuse and arrange into microstructures as the result of inter-particle interactions.^{31, 36, 94} The resulting assemblies can be then deposited on solid substrates for surface patterning.¹¹

The interactions of particles at fluid-fluid interfaces differ both in range and nature with respect to the interactions in a single fluid phase. As introduced in Chapter 2, the presence of the interface between a polar and non-polar phase is responsible for long-ranged electrostatic interactions. The resulting force is always repulsive, it may extend over several micrometers, and can be modulated by changing the charged species on the particle surface, the particle three-phase contact angle, or the ionic strength of the aqueous sub-phase.^{29, 36, 38–40} Deformations of the fluid interface are responsible for long-ranged capillary interactions, driven by surface minimization. The inter-particle potential has been formally treated as a superposition of capillary multipoles, in analogy with electrostatics, where the order of the capillary multipole (charge, dipole, quadrupole, etc.) depends on how the interface is deformed at the boundary conditions (e.g. by gravity, shape anisotropy, surface heterogeneities).^{70–74, 171} The resulting interacting force can be either repulsive or attractive depending on inter-particle orientation and order of the capillary multipole.³⁹ In the last years, progress has been made in developing theoretical models together with numerical methods in order to describe the interaction of particles at fluid interfaces with arbitrary shapes. Experiments have focused on self-assembly processes of anisotropically shaped particles monitored using video microscopy,^{73, 74, 78, 79} and to optical tweezers experiments.⁴⁰ The small size of the particles, the optical discontinuity between the two fluid phases, and the required control of the positions of and/or the forces on the particles are complicating factors in the experiments.

The inter-particle potential can be measured with both indirect and direct experimental approaches. When the concentration of colloids at the interface is sufficient to form a 2D crystal (surface fraction $\phi_s \geq 0.2$), Zwanzig *et al.*²⁰⁹ demonstrated that the interaction potential can be calculated from the dependence of macroscopic shear modulus on surface coverage. However, this approach is sensitive to both hydrodynamic interactions and defects in the crystal, providing a lower limit for the interaction force.²¹⁰ At a low surface fraction of colloids at the interface ($\phi_s \rightarrow 0$), it is possible to measure the pair correlation function $g(r)$ from digital images and then determine the pair interaction potential from

fitting the Boltzmann distribution $U(r) = -k_B T \ln g(r)$.^{40,210} This method requires a large number of particles and images, and only provides an average potential.

Direct methods allow to measure interactions on single particles and are mainly restricted to optical tweezers experiments.^{80–82} Force versus distance curves are measured on pairs of particles within a force range of 0.1 – 100 pN and with a position accuracy of a few nanometers, from which the interaction potential is determined. Results have shown that electrostatic and capillary forces can be conveniently modulated by the addition of salts, surfactants or polyelectrolytes. This in turn changes particle wettability, surface tension and the rheology of the interface.^{36,58} Several microrheology techniques are available to monitor the interfacial viscosity, such as magnetic micro-needles,^{62,65} magnetic micro-buttons,⁶⁴ and optical tweezers, but only the latter one is suited to measure inter-particle forces. Despite this, most of the studies have been limited to measurements of capillary forces for interfaces at equilibrium.⁴⁰ Only a few studies have shown time-dependent inter-particle interactions upon the addition of surfactants and salts,^{211,212} but only on very large timescales (~hours). The study of non-equilibrium systems poses several challenges, as changes of interfacial viscosities and of inter-particle forces happen on a wide range of timescales and values, and possible correlations have not been fully explored yet.

In this Chapter, we used magnetic tweezers to investigate inter-particle capillary forces between spherical particles adsorbed at a water-oil interface with strong polymer-induced ageing. Magnetic tweezers operates with commercially available magnetic particles, which can be conveniently manipulated by means of external magnetic fields with forces ranging from tens of nN to hundreds of pN,⁸¹ and with low interference with the surrounding materials. Moreover, magnetic particles can be easily functionalized and are available with a wide range of sizes, material and optical properties, making them suitable for a wide range of applications¹² and material systems.

We quantify the interfacial drag coefficient of pairs of particles using the intra-pair magnetophoresis (IPM) technique, as described in Chapter 3.^{189,213} Pairs of magnetic particles are displaced using well-controlled magnetic dipole-dipole forces, (~ pN), allowing one to measure changes of interfacial viscosity within a few seconds and over very large variations (10^{-7} to 10^{-4} Ns/m). In the absence of the magnetic field, we record multiple trajectories of particle attraction utilizing the same particle pair. The experiment gives an independent quantification of the interfacial drag coefficient and of the magnitude of non-viscous inter-particle forces in the system.

4.2 Materials and methods

4.2.1 Materials

We use a silicone-based amino-functionalized polymer (KF8004, provided as samples by Shin-Etsu Silicones Europe B.V.), which is soluble only in the oil phase. The oil phase is isononyl-isononanoate (Lanol 99, Seppic, $\eta_{oil} = 6$ mPa·s) and polymer concentrations are prepared by weighting the components. The aqueous phase consists of phosphate buffered saline (PBS), prepared by dissolving PBS tablets (PBS tablets, pH 7.4, Sigma Aldrich) in 200 mL of ultra-pure water (resistivity > 18.2 M Ω ·cm) according to the supplier and then further diluted to a final concentration of 20 mM. All the components were used as

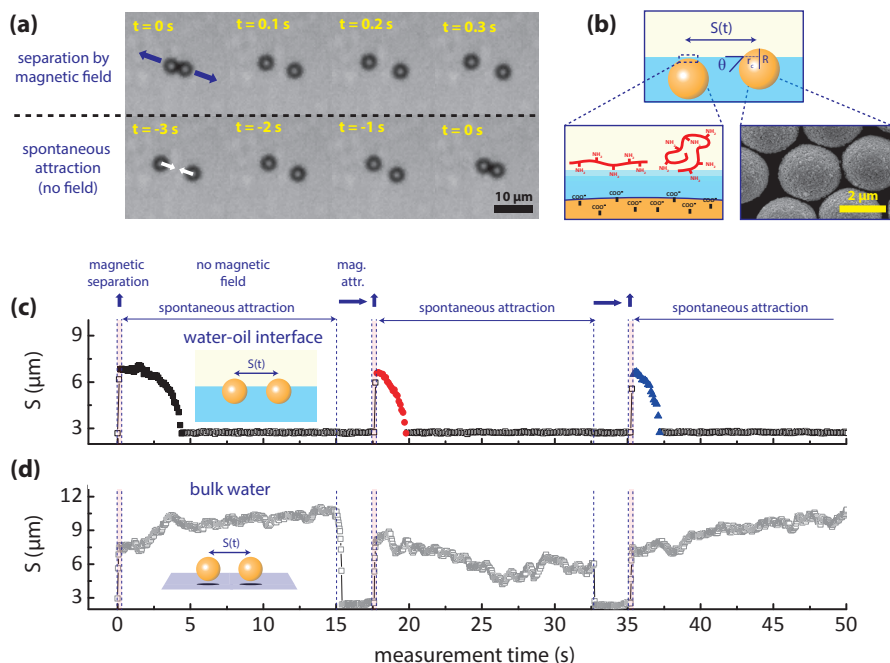


Figure 4.1: Principle of colloidal attraction experiments. (a) Pairs of super-paramagnetic particles at a water-oil interface are separated by applying a brief magnetic field in the direction normal to the interface.¹⁸⁹ In the absence of a magnetic field, spontaneous attraction is observed. (b) Sketch of magnetic particles at a water-oil interface in the presence of an amino-modified silicone polymer. Particles adsorb to the interface only in the presence of the polymer as the result of electrostatic interactions between the carboxylated surface of the magnetic particle, with negative charges, and the amine group of the polymer exposed to the water phase, with positive charges (see Chapter 3).⁵⁵ The Scanning Electron Microscopy (SEM) image of M270 particles ($2R = 2.8 \mu\text{m}$) shows a particle surface roughness of about 50 to 150 nm. Panels (c) and (d) show time-traces of the center-to-center separation distance S during colloidal attraction experiments for particles at a water-oil interface and for particles in bulk water moving on a glass substrate respectively. In (c) the highlighted points (coloured solid symbols) show the trajectories of spontaneous (non-magnetic) particle attraction, which is observed for particles adsorbed to the water-oil interface (as in panel c), but not for particles in bulk water (as in panel d). This proves that the spontaneous attraction is caused by the fluid-fluid interface and not by magnetic forces.

received from the suppliers, without any further purification step.

We use carboxylic super-paramagnetic particles (Dynabeads M-270 carboxylic acid, diameter $2R = (2.8 \pm 0.1) \mu\text{m}$, Life Technologies) to quantify the particle interfacial drag coefficient and inter-particle interactions. In the presence of a magnetic field, the induced magnetization follows a Langevin function, with a particle-to-particle variation of magnetic susceptibility of about 8%.¹⁸⁹ We use carboxylic ferromagnetic particles (CFM-300-5 carboxylic acid, ferromagnetic, nominal size $28 - 34.9 \mu\text{m}$, Spherotech) to quantify the particle contact angle at the water-oil interface. Particles were magnetically washed

four times in ultra-pure water in order to remove surface-active elements present in the storage buffer, and were then dispersed in each corresponding buffer in a ratio 1 : 10000 from the stock solution. The fluid cell and the setup required to actuate magnetic particles are described in Chapter 3.

4.2.2 Quantification of particle drag coefficients and attractive capillary interactions at a water-oil interface

We quantify the drag coefficient of particles and the magnitude of attractive capillary forces at the water-oil interface with a method developed in a previous paper of us and described in Chapter 3, namely intra-pair magnetophoresis (IPM).^{189,213} Pairs of magnetic particles are attracted and repelled by well-controlled magnetic dipole-dipole forces \vec{F}_{dd} . During magnetic separation of the particles, both attractive capillary forces \vec{F}_{cap} and drag forces \vec{F}_{drag} oppose to the motion of the particles, with a total force expression

$$\vec{F}_{dd} + \vec{F}_{cap} + \vec{F}_{drag} = 0 \quad (4.1)$$

In section 2.3.4 of Chapter 2 we introduced a class of interactions that originate from the deformation of fluid-fluid interfaces, namely capillary interactions. Formally, these deformations are described as a superposition of capillary multipoles of order m , where $m = 0, 1, 2, \dots$ represent capillary charges, dipoles, quadrupoles etc., in analogy with electrostatic.³⁹ For micrometer sized particles ($< 10 \mu\text{m}$) deformation due to gravity can be neglected ($E_o \ll 1$). In the absence of any external torque the first non-vanishing term is the quadrupolar interface deformation ($m = 2$) and the resulting force between two identical particles can be expressed as

$$F_{quad} = -\frac{\delta E_{AB}}{dS} = -48\pi\gamma H_2^2 \cos(2(\phi_A + \phi_B)) \frac{r_c^4}{S^5} \quad (4.2)$$

where H_2 is the amplitude of the quadrupolar meniscus and r_c is the radius of the cross section formed by the particle with the interface, which is related to the equilibrium contact angle θ by the geometrical relation $r_c = R \cos \theta$ (Fig. 4.1b). For ease of notation, we rewrite eqn (4.2) as

$$F_{cap} = -F_0 \left(\frac{2R}{S} \right)^5, \quad \text{with } S \geq 2R, \quad (4.3)$$

where $F_0 = \frac{3\pi}{2R} \gamma H_2^2 \sin^4 \theta$ is the closest proximity capillary force, i.e. the force calculated at $S = 2R$. For particles in a purely viscous fluid (e.g. water) and in the absence of magnetic forces (i.e. $\vec{F}_{dd} = 0$ in eqn 4.1), this force is counterbalanced by the particle drag force $F_{drag} = \frac{f}{2} \frac{dS}{dt}$, where f is the particle drag coefficient, and the resulting equation of motion can be expressed as

$$S^6 = -\frac{12(2R)^5 F_0}{f} \cdot (t - t_0) + S_0^6 \quad (4.4)$$

from which F_0 can be estimated once the drag coefficient of particle f is known.

In Chapter 3, we introduced the formalism to describe magnetic dipole-dipole forces, which we summarize here for convenience. Briefly, by applying a field normal to the plane of the interface, the particles induced dipole moments are parallel and point in the same direction. If only drag forces are present (i.e. $\vec{F}_{cap} = 0$ in eqn 4.1), the center-to-center separation S increases according to

$$S(t)^5 = \frac{15\mu_0}{2\pi} \cdot \frac{m_{d,1}m_{d,2}}{f} \cdot (t - t_0) + S_{0,dd}^5 \quad (4.5)$$

where μ_0 is the vacuum permeability, $m_{d,i}$ is the magnitude of the induced magnetic dipole moment (in units Am^2) for particle i , and $S_{0,dd}$ is the separation distance at time t_0 . In principle, the particle drag coefficient f could be then quantified from fitting magnetic repulsion experiments with eqn (4.5). However, in the presence of capillary forces, eqn (4.5) does not hold anymore. By considering eqns (4.3) and (3.2), the equation of motion (4.1) can be recast as

$$\frac{f}{2} \frac{dS}{dt} = F_{0,dd} \left(\frac{2R}{S} \right)^4 - F_0 \left(\frac{2R}{S} \right)^5 \quad (4.6)$$

where for ease of notation we introduced the closest proximity magnetic force $F_{0,dd} = \frac{3\mu_0 m_1 m_2}{4\pi(2R)^4}$ in analogy with the notation we used for the expression of the capillary force. The relation between the particle drag coefficient f and the interfacial viscosity η_s relies on the assumptions of the underlying hydrodynamic models,^{26,55,68,69} and depends on the actuation dynamics of the probe (e.g. rotation or translation).⁶⁷ In Chapter 3, we addressed these issues related to the current technique and we demonstrated that the response of the interface for the material system used in this study is mainly viscous.²¹³ In this study we do not make any assumption on the underlying hydrodynamic model and we will characterize the ageing of the interface through the particle drag coefficient f .

In order to disentangle conservative inter-particle forces from dissipative effects caused by interfacial ageing, both F_0 and f needs to be taken into account in eqn (4.6) and eqn (4.4). We designed an experiment in which for every particle pair, (i) we first acquire a magnetic repulsion trajectory by applying a repulsive field for 4 s, thereby separating the particles of a few particle diameters. After positioning magnetically the particle pair at $S = 2R$, we use a short repulsive field to separate pairs of magnetic particles. Then, in the absence of any magnetic field, (ii) we record 3 motion trajectories of the resulting interaction (Fig. 4.1c) and compute the average of the curves that show full approach. The entire motion trajectory can be recorded in about 60 s. From the trajectories acquired with (i) and (ii), we estimate f and F_0 as described in section 4.D.

4.2.3 Numerical methods

We performed Brownian Dynamics (BD) simulations in order to generate trajectories of particles that undergo Brownian motion in the presence of a total (conservative) force \mathbf{F} . The aim of BD simulations was twofold. On one hand, we determined the interplay between dissipative (viscous) forces and conservative (capillary) forces. On the other hand, we validated and determined the accuracy of the analysis method as described in section 4.2.2 in estimating both f and F_0 . Simulations were performed by following the

approach described by Grassia *et al.*²¹⁴ A massless particle i is moving with a tensor coefficient of linear friction ξ_{ij} and diffusivity tensor $D_{ij} = k_B T / \xi_{ij}$, where $k_B T$ is the Boltzmann temperature. The trajectories of particles are obtained by adding at each time-step δt a random displacement \mathbf{x}_i^{ran} to the systematic displacement $\mathbf{F}_i(\xi_{ij}^{-1})\delta t$. If we neglect hydrodynamic interactions between the particles and we consider a constant linear friction coefficient $\xi_{ij} = f$, then BD trajectories $\mathbf{x}_i(t)$ are computed from the relation

$$\mathbf{x}_i^{n+1} = \mathbf{x}_i^n + \frac{\mathbf{F}_i}{f}\delta t + (24D\delta t)^{\frac{1}{2}}\mathbf{r}_i^n \quad (4.7)$$

where \mathbf{r}_i^n is a random vector with independent components, each of them extracted from a uniform distribution in the interval $[-0.5, 0.5]$. The generated random displacements will converge to a Gaussian distribution, provided a sufficiently small time-step and the correct moments of the distribution,²¹⁵ i.e. zero mean and a variance that follows from the dissipation-fluctuation theorem.²¹⁶ Simulations are performed with a time-step $\delta t = 2 \cdot 10^{-5}$ s. We validated this numerical method following the approach proposed by Northrup *et al.*,²¹⁷ as shown in section 4.A.

4.3 Results

We studied the interaction of carboxylic magnetic micro-particles at a water-oil interface in the presence of an amino-modified silicon polymer in the oil phase. For an aqueous solution containing 20 mM of phosphate buffered saline (PBS), we observed an attractive interaction between particles over tens of micrometers, depending on polymer concentration. On the other hand, polymers are known to adsorb to fluid-fluid interfaces, wherein the interactions between the adsorbed polymers (e.g. hydrogen bonding, hydrophobic or electrostatic interactions) can contribute to large variations of the interfacial shear viscoelasticity,^{58,197} on a timescale varying from a few seconds to several hours. In order to disentangle conservative forces from dissipative effects, we have designed an experiment in which pair of particles are magnetically separated of a few μm using the IPM method. Then, repeated motion trajectories are recorded on the same particle pair (section 4.2.2).

In this section we present the results as follows. We first provide examples of colloidal attraction experiments for particles at a water-oil interface for different concentrations of polymer in the oil phase. Then, we use Brownian dynamics (BD) simulations to interpret the experiments and to validate our analysis method to quantify capillary and viscous forces. Finally, we quantify the interfacial drag coefficient of particles and attractive capillary forces as a function of polymer concentration.

4.3.1 Measurements of colloidal attractive interactions

In a typical experiment of particle attraction, pairs of magnetic particles are first separated by a few particle diameters by shortly applying an out-of-plane magnetic field and then, after removing the field, the field-free motion trajectories are recorded (Fig. 4.1a). In order to exclude the influence of any magnetic component (e.g. setup, particle magnetic moment) on particle attraction, we performed the same experiment using particles in bulk water moving on a glass substrate (Fig. 4.1d). In the absence of the magnetic field, the

particles showed free diffusion with a diffusion coefficient of $0.18 \mu\text{m}^2/\text{s}$, consistent with the diffusion of a sphere with radius $R = 1.4 \mu\text{m}$ in a fluid of viscosity $\eta = 1 \text{ mPa}\cdot\text{s}$ (free diffusion $D = 0.15 \mu\text{m}^2/\text{s}$) in close proximity to a solid substrate.¹³⁶ In the absence of a magnetic field, particles did not show full approach and attraction was observed only when an in-plane magnetic field was applied.

In Fig. 4.2 we show results of colloidal attraction experiments for particles at a water-oil interface at increasing initial concentrations of polymer in the oil phase. Panels (a1)-(a3) show the center-to-center separation S as a function of the particle approach time $t_{appr} = t - t^*$, where t^* is the time for the particle pair to reach $S = 2R$. In each graph, trajectories are recorded on the same particle pair. For $c_p = 1 \cdot 10^{-3} \text{ w/w}\%$ (a1) the trajectories show either partial or full approach and thermal (Brownian) noise is large compared to the attractive interaction. Attraction is clearly shown for $S < 4 \mu\text{m}$. For c_p equal 2 and $4 \cdot 10^{-3} \text{ w/w}\%$ (panel a2 and a3 respectively), attraction is clearly seen for $S < 6 \mu\text{m}$ and $S < 8 \mu\text{m}$ respectively. The reproducibility of the trajectories is high, with a mean standard deviation of 6% and 3% respectively.

According to the model described by eqn (4.4), the timescale for particle attraction is determined by the initial separation S_0 between the particles, the interfacial drag coefficient of particles f , and the magnitude of the capillary force F_0 . In order to take into account the drag coefficient f experienced by the particle at different ageing times t_{age} of the interface, we plot the mean and standard deviation of the trajectories that show full approach (denoted as N_{appr}) as the product $f \cdot \bar{S}^6$ and as a function of the particle approach time t_{appr} (Fig. 4.2b). Data show two distinct regions. For separation distances of a few particle diameters ($t_{appr} < -2 \text{ s}$), the curves show large variations. When the inter-particle distance decreases ($t_{appr} > -2 \text{ s}$) the curves approach the relationship described by eqn (4.4) (Fig. 4.2b, insets). The observed increase of the steepness of $f \cdot \bar{S}^6$ curves points to an increase of the attractive force as a function of polymer concentration.

4.3.2 Brownian dynamics (BD) simulations of capillary attraction

In order to interpret the attraction curves measured in our experiments and to determine the interplay between attractive forces and thermal fluctuations, we used BD to generate trajectories of pair of particles according to eqn (4.7) and in the presence of an interacting force as described by eqn (4.3). In these simulations, we consider the diffusion of particles in a purely viscous fluid with a constant drag coefficient f and we do not take into account the relative angular orientation nor the hydrodynamic interactions between the particles.

In each graph of Fig. 4.3a, we show 6 trajectories of particle attraction obtained with the same set of initial conditions. For a capillary force $F_0^{sim} = 0.112 \text{ pN}$ (a1) trajectories show both partial and full approach, with a high variation between repeated simulations. For increasing values of F_0^{sim} the range of the attraction extends towards larger inter-particle distances S and the encounter rate of particles increases (section 4.B), with a reduced variation between the trajectories.

Fig. 4.3b shows curves expressing $f \cdot \bar{S}^6$ as a function of particle approach time. These results show similar features as compared to the experimental trajectories shown in Fig. 4.2b. For a low interacting force (b1) and separations larger than ~ 2 particle diameters, the motion is dominated by thermal fluctuations, as the attractive interacting

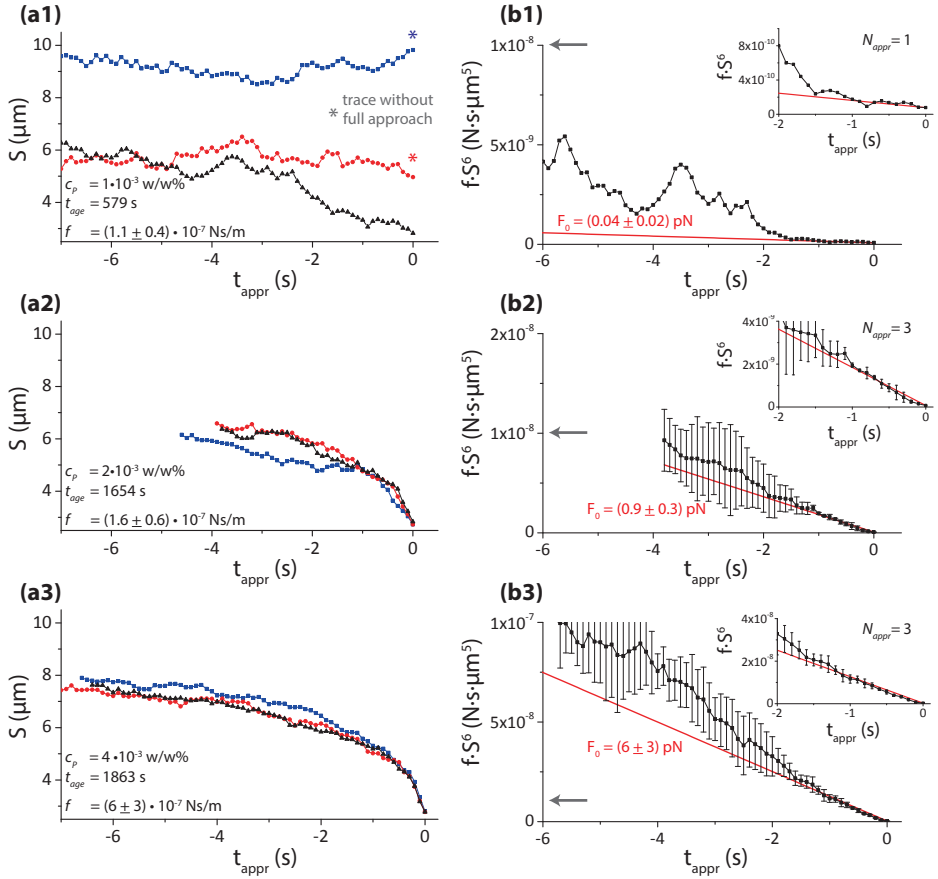


Figure 4.2: Colloidal attraction experiments for particles at the water-oil interface for increasing concentrations of polymer in the oil phase (c_p) and different ageing time (t_{age}). **(a)** Center-to-center separation S as a function of particle approach time t_{appr} . Each panel **(a1, a2, a3)** shows 3 approach trajectories measured on the same particle pair. Different panels **(a1, a2, a3)** show different particle pairs. **(b)** In order to quantitatively compare measurements performed at different ageing times, i.e. to take into account the drag coefficient f of particles experienced at a different t_{age} , we plot attraction curves expressing $f \cdot \bar{S}^6$ as a function of particle approach time for particles with full approach in panels **(a)**, i.e. $S = 2R$ at $t_{\text{appr}} = 0$. Points and error bars in panels **b2** and **b3** represent the mean and the standard deviation. The solid red line is a fit according to eqn (4.4), performed only on the linear part of $f \cdot \bar{S}^6$ attraction curves close to $t_{\text{appr}} = 0$, as shown in the insets. From the fit, we extract the value of the capillary force F_0 , i.e. the capillary force at $S = 2R$. The gray arrow indicates a reference value on the y axis for comparison.

energy is less than $\sim 2 k_B T$. At shorter separations the attractive interaction overcomes the thermal fluctuations and the curve approaches the expected result based on eqn (4.4). This becomes clearer for increasing values of F_0^{sim} (b2), where the linear relationship extends towards larger separation distances ($S \approx 7 \mu\text{m}$). Therefore, in order to correctly estimate

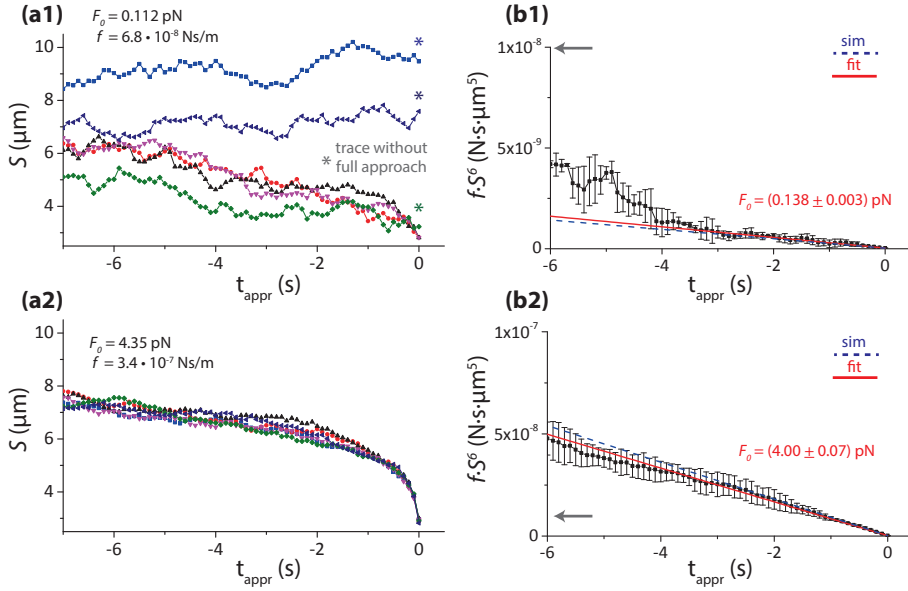


Figure 4.3: Brownian Dynamics simulations for a pair of particles ($R = 1.4 \mu\text{m}$) in the presence of an attractive force as described in eqn (4.3). **(a)** Center-to-center separation S as a function of particle approach time obtained from 6 simulations performed with the same set of initial conditions (as indicated in each graph). **(b)** Attraction curves expressing $f \cdot S^6$ as a function of particles approach time. Points and error bars represent the mean and the standard deviation of the curves that show full approach in the corresponding panel (a), i.e. $S = 2R$ at $t_{\text{appr}} = 0$. The solid red line is a fit according to eqn (4.4) of only the initial linear part of the $f \cdot S^6$ attraction curves. The dashed blue line represents the simulated attraction curve without Brownian motion. The gray arrow indicates a reference value on the y axis for comparison.

F_0 , we select the points close to $t_{\text{appr}} = 0$ that follows eqn (4.4). With this approach we are able to retrieve values of the simulated parameters with an accuracy of at least 15% for $F_0^{\text{sim}} \leq 1$ (see section 4.B, Table 4.D.1).

The last step required to quantify the capillary force F_0 from the experiments shown in Fig. 4.2b is to determine the drag coefficient f of particles at the water-oil interface.

4.3.3 Ageing of the interface due to the presence of polymer

We quantified the drag coefficient f of particles at the water-oil interface from magnetic repulsion experiments using the IPM method (section 4.2.2).^{189,213} In particular, we studied the ageing of the interface by quantifying f as a function of polymer adsorption time, for different initial polymer concentrations c_P in the oil phase. We consider the moment the interface is formed within the fluid cell as the reference time for the experiments.

For all polymer concentrations, data show an increase of f as a function of polymer adsorption time (Fig. 4.4a). The time onset for drag increase shifts towards lower adsorption times for higher values of c_P , consistent with a higher diffusive flux of polymer towards the interface. Values obtained from different particle pairs show a variation within

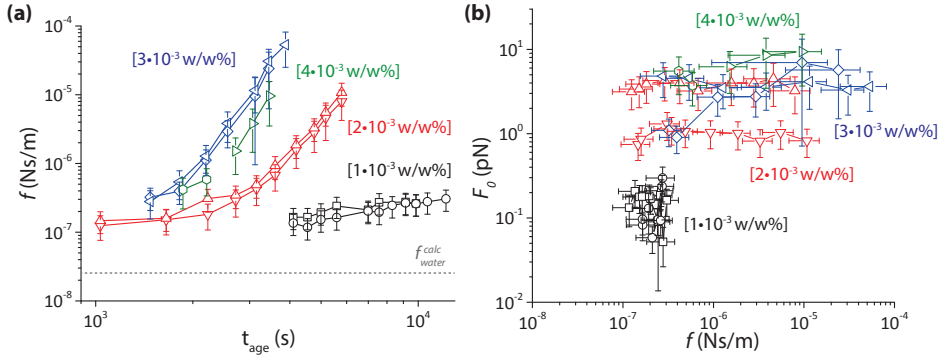


Figure 4.4: Capillary attraction in the presence of polymer-induced interfacial ageing. **(a)** Interfacial drag coefficient f as a function of interfacial ageing time, as measured by IPM experiments.¹⁸⁹ Experiments were performed for different initial polymer concentrations c_P (colours) using an aqueous solution with 20 mM PBS. In both graphs, connected symbols represent data recorded on the same particle pair (a total of 8 pairs are shown). **(b)** F_0 as a function of f . Error bars include a variation of the particle magnetic moment of 8%,¹⁸⁹ and the error from the iterative fitting used to estimate the particle drag coefficient f and the capillary attraction force F_0 , as described in section 4.2.2.

the experimental errors ($\approx 10\%$), suggesting a homogeneous ageing of the interface. As we will show in the next section, capillary forces may become comparable to the magnetic forces used to separate particles. This can be taken into account in our analysis, as described in section 4.2.2 and demonstrated with BD simulations in sections 4.C and 4.D.

4.3.4 Quantification of colloidal attractive force

With the same particle pairs used to quantify f in Fig. 4.4a (represented by open symbols connected by a solid line), we computed the magnitude of the capillary attractive force F_0 , thus providing a direct correlation between f and F_0 . Fig. 4.4b shows values of F_0 as a function of f for different initial concentration of polymer in the oil phase (represented as different colors). For a fixed polymer concentration, the capillary attraction varies strongly per particle pair, but for a given particle pair, interestingly the capillary attraction does not depend on f , hence on the amount of polymer adsorbed to the interface. In particular, for $c_P = 2 \cdot 10^{-3}$ w/w% the represented pairs (up and down red triangles) show similar values for f , but F_0 differs by almost one order of magnitude. For increasing amounts of c_P , F_0 increases with values ranging between ~ 0.1 and ~ 10 pN. For $c_P > 4 \cdot 10^{-3}$ w/w% (data not shown) the attractive force exceeds the maximum magnetic repulsive force achievable with the configuration of the electromagnets used for this study ($F_{dd} \approx 20$ pN), so that it was not possible to record repeated attraction trajectories.

4.4 Discussion

We investigated attractive forces between spherical magnetic particles adsorbed at a water-oil interface in the presence of an amino-modified silicon polymer. The role of the polymer is twofold. First, the very low solubility of the polymer in water causes only the

amine groups to penetrate the interface into the water phase, which then interact electrostatically with the negatively charged particles.^{35,197} This in turn modulates the particle contact angle²¹³ (see section 4.E) and the magnitude of capillary attraction between the particles (Fig. 4.4b). Second, polymer adsorption to the interface generates an increase of the interfacial viscosity, over several orders of magnitude in a timespan of a few hours (Fig. 4.4a). In this section, we first focus on the origin of particle attraction. Then, we discuss how changes of interfacial viscosity influence the conservative attractive force.

4.4.1 Interpretation of capillary attraction curves

Deformations of fluid-fluid interfaces are known to be responsible for long-range capillary forces and torques between particles (see section 2.3.4). The inter-particle potential can be described in terms of capillary multipoles, as described by eqn (2.22), whose terms depend on the nature of the deformations (e.g. gravity, shape or chemical anisotropy).^{71–75,141}

The results in Fig.4.2 show that at large separations, motion trajectories are dominated by thermal (Brownian) motion. Therefore, we performed BD simulations in order to disentangle the contribution of thermal noise from that due to the attractive force and to validate the analysis method described in section 4.2.2. We demonstrated that from the linear part of $f \cdot \bar{S}^6$ curves (Fig. 4.3b) it is possible to compute the magnitude of the capillary coefficient F_0 with an accuracy of at least 15% depending on the magnitude of the attractive force, given the particle drag coefficient f as a fixed parameter (see section 4.B, Table 4.D.1). We tested the ability of our approach to discriminate between different orders of attraction by performing BD simulations using $m = m_A + m_B = 3, 4, 5$ in eqn (2.22). With this analysis method we were able to discriminate between the different orders only in the presence of capillary forces greater than a few pN (section 4.B). Nonetheless, for the system of this study ($2R = 2.8 \mu\text{m}$, $\gamma = 20 \text{ mN/m}$, $\rho_P = 1.8 \text{ g/cm}^3$) the Eötvös number $\text{Eo} \approx 10^{-6} \ll 1$, and deformations due to gravity ($m = 0$) are negligible. For spherical particles, dipolar deformations ($m = 1$) require the application of an external torque or the presence of surface chemical anisotropy, such as for Janus particles.¹⁴² Super-paramagnetic particles are known to have a small remanent magnetic moment. The maximum magnetic torque $\vec{\tau} = \vec{m} \times \vec{B}$ applicable on the particles of this study has been calculated by van Reenen *et al.*⁸⁹ to be $4 \cdot 10^{-18} \text{ Nm/rad}$ (for a magnetic field of 36 mT). We used the results from Xie *et al.*¹⁴² to determine the torque required to deform a fluid-fluid interface (see Chapter 5). The authors performed lattice Boltzmann simulations of capillary deformations for magnetic Janus particles at a fluid-fluid interface. The strong affinity of the two phases with the hemispheres of the Janus particle mimic the pinning of the three-phase contact line to the surface of the particle, so that only interfacial deformations are considered. In the limit of small interfacial deformations, the required torque to deform the interface is $\sim 10^{-13} \text{ Nm/rad}$, which is well above the maximum applicable magnetic torque in our system. Therefore, the first non-vanishing term in eqn (2.22) is the capillary quadrupole ($m = 2$).

The attractive force observed in experiments performed at the water-oil interface (Fig. 4.2) agrees in range ($\sim 10 \mu\text{m}$) and magnitude ($\sim \text{pN}$) with BD simulations (Fig. 4.3), with an inter-particle dependence as $\sim 1/S^5$. Stamou *et al.* suggested that quadrupolar

interface deformations may originate from the pinning of the three-phase contact line to local heterogeneities (e.g. chemical or topological) of the surface of the particles,⁷⁰ with the corresponding interacting force as described by eqn (4.3). The particles used in this study (M270 - carboxylic, $2R = 2.8 \mu\text{m}$) have a surface roughness between 50 nm and 150 nm, as determined by SEM images (Fig. 4.1b). According to eqn (4.2), a contact angle $\theta \simeq 16^\circ$ (with $H_2 = 50 \text{ nm}$, $\gamma = 20 \text{ mN/m}$) would be sufficient to generate attractive forces as large as $F_0 \simeq 1 \text{ pN}$. Therefore, we interpret the force as being caused by quadrupolar deformations of the fluid-fluid interface induced by particle surface roughness. A similar conclusion was reported by Park *et al.* from measurements of attractive forces between polystyrene beads confined at a water-decane interface using time-shared optical traps.⁸² The authors measured forces with the same functional form as eqn (4.3) and magnitudes similar to the ones shown in Fig. 4.4b, with values that depended on fluid composition and particle contact angle.

Electrostatic interactions may also play a role between particles at fluid-fluid interfaces.⁴⁰ The asymmetry of the charge distribution across the interface is responsible for long-ranged repulsive forces that scale with inter-particle distance as $\sim 1/S^4$. Attractive electrostatic forces have been previously observed only at short inter-particle distances ($< 100 \text{ nm}$), resulting from patches of charges on the surface of the particles.²¹⁸ We performed experiments of particle attraction using different ionic strengths of the aqueous phase. For an aqueous solution containing 150 mM PBS, no significant repulsion or attraction was measured for all polymer concentrations (data not shown), while for an aqueous solution with 20 mM PBS experiments showed an increase of an attractive force. The contribution of the dissociated charges in the water side of the interface is negligible for both fluid compositions, as the Debye length $\kappa^{-1} \simeq 0.8 \text{ nm}$ and $\kappa^{-1} \simeq 2 \text{ nm}$, for 150 mM and 20 mM PBS in the aqueous phase respectively. A small amount of surface charges may be present in the oil phase due to residual water in the non-polar solution or to water entrapped on cavities present on the surface of rough particles. This would be sufficient to generate long-ranged repulsive forces.⁸⁰ In our system, the negative charges exposed to the oil side of the interface are expected to be counterbalanced by the cationic polymer.¹³⁹ Moreover, in the experiments no distance dependence as $\sim 1/S^4$ was observed, so that electrostatic forces can be neglect in our analysis. Other forces, such as van der Waals or solvation forces may be present, but are relevant only at small distances ($\sim \text{nm}$), with a contribution to the total energy potential of only a few $k_B T$.²⁹

4.4.2 Capillary attraction as a function of interface ageing

We quantified the dissipative effects caused by interfacial ageing using the IPM method.^{189,213} With this technique, we were able to quantify the drag coefficient f of particles at the water-oil interface within a few seconds ($\sim 5 \text{ s}$) and over long timescales (several hours), with a sensitivity to changes of interfacial viscosity as low as $\eta_s = 7 \cdot 10^{-9} \text{ Ns/m}$.²¹³ Using BD simulations, we demonstrated that the presence of known attractive capillary forces can be correctly taken into account in the analysis, providing results with an accuracy within 4% in retrieving the input parameters (section 4.C). When both f and F_0 are unknown, our analysis method provided results with an accuracy of 9% and 30% respectively with respect to the input parameters (see section 4.D, table 4.D.1).

When the interface is formed, polymers adsorb to a pristine interface without steric hindrance. In absence of an energy barrier for adsorption, at short times ($t \rightarrow 0$) the surface coverage can be estimated by a diffusive transport.²⁰¹ For longer times the adsorption rate is lowered by the presence of only few remaining adsorption sites in the interfacial monolayer.⁴⁴ Here, the interactions between the adsorbed polymers contribute to a strong interface ageing, as shown by the increase of the particle drag coefficient f over several orders of magnitudes ($f \sim 10^{-7}$ to 10^{-4} Ns/m, Fig. 4.4a).

In Chapter 3,²¹³ we demonstrated that the adsorbed polymer layer to the interface responds to the motion of the probe mainly as a viscous fluid, so that the magnetic induced motion of the probe can be described by eqn (4.5). For increasing polymer concentrations, the time onset for drag increase shifts towards lower times, in agreement with a higher diffusive flux of polymer to the interface. The rate of drag increase depends strongly on c_P . For $c_P = 1 \cdot 10^{-3}$ w/w% f increases of a factor 2 in a time span of one decade, while for c_P equal to 3 and $4 \cdot 10^{-3}$ w/w% f shows a 1000 fold increase. Moreover, we found the adsorption kinetics to be strongly influenced by the ionic strength of the water sub-phase. In particular, for an aqueous phase with 20 mM PBS and $c_P = 1 \cdot 10^{-3}$ w/w% (black squares Fig. 4.4a), the adsorption kinetics cannot be described only by diffusive transport, as compared to experiments performed with higher polymer concentrations or higher ionic strength of the aqueous phase.²¹³ These results point to a history-dependent adsorption kinetics, where the evolution of the interface is determined by the early stages of polymer adsorption.⁴⁵

The presence of the polymer at the interface is also responsible for the modulation of the position of the particle at the interface, i.e. its contact angle, as the result of electrostatic interactions as described in Chapter 3.^{35,213} Particles adsorbed to the interface only in the presence of the polymer and, for a sufficient polymer concentration, the particles transitioned into the oil phase. Typically, the adsorption of particles to fluid-fluid interfaces is driven by strong interfacial forces, with timescales varying from milliseconds to several minutes or hours. The slower times can be attributed to friction forces due to the displacement of the three-phase contact line on the surface of the particle.^{51,52,94} Measurements of the contact angle of larger particles ($2R \approx 34 \mu\text{m}$) (with a similar surface chemical functionality as the small particles) show an increase of the particle contact angle for increasing polymer concentrations, with a time-dependent increase ($\sim \text{min}$) for $c_P > 5 \cdot 10^{-2}$ w/w% (see section 4.E).

From a direct comparison between F_0 and f (Fig. 4.4b), we observe that capillary attractive forces increase for increasing polymer concentration in the oil phase. According to eqn (4.2), this could be attributed to an increase of the particle contact angle, provided the other parameters are the same. This is in agreement with contact angle measurements (section 4.E) and with the observation of attractive forces exceeding magnetic repulsive forces for higher concentrations of polymer. Moreover, the absence of attractive forces for a high ionic strength solution suggests a small particle contact angle due to a weak electrostatic interaction between the polymer and the particles.

However, for a fixed polymer concentration, F_0 does not depend on f and changes are dominated by particle-to-particle variation. Data in Fig. 4.4b show that F_0 depends only on the initial amount of polymer in the oil phase and is independent of f , hence

on the amount of polymer that is subsequently adsorbed to the interface. For low and constant values of f , the density of the polymer at the interface is low ($\eta_S \sim 0$) and the motion of the probe is sub-phase dominated ($Bo \ll 1$).⁶⁹ In this regime, the drag of the particle is sensitive to changes of θ . For $c_P = 1 \cdot 10^{-3}$ w/w%, f increases by a factor of 2, but F_0 do not show any correlation with f . Therefore, we attribute the increase of drag as an increase of polymer concentration at the interface, while the contact angle remains constant. For increasing values of f , the motion of the probe is dominated by changes of interfacial viscosity (Boussinesq number $\gg 1$). The lack of a correlation between the corresponding values of F_0 suggests again a constant value of the contact angle.

Overall, these results suggest that the position of the particle at the interface is fixed at the early stages of polymer adsorption. As proposed by Maestro *et al.* studying polymers to an air-water interface,⁴⁶ at an early ageing time ($t_{age} \approx 0$) and a low polymer concentration, all the monomers in a chain are adsorbed at the interface, with an ideal pancake-like conformation (for a good solvent condition). Here, the polymer exposes the amine groups to the water side of the interface, where they interact with the carboxylic groups of the particle surface. For increasing initial polymer concentration in the oil phase, the higher polymer flux towards the interface combined with the strong attractive force of polymer to the particle contributes to an increasing polymer density on the surface of the particle, which translates in an increase of the particle contact angle. Thereafter ($t_{age} > 0$), the entangled polymer layer hinders further diffusion of polymers to the particle surface, thus equilibrating the particle contact angle and capillary forces.

4.5 Conclusions

We have studied attractive forces between spherical magnetic particles at a water-oil interface for a system with strong polymer-induced interface ageing. The experiment gives an independent quantification and a direct correlation of the interfacial drag coefficient ($10^{-7} \sim 10^{-4}$ Ns/m) and the non-viscous inter-particle forces (0.1 \sim 10 pN) in the system. We have validated the proposed method by performing Brownian Dynamics (BD) simulations, showing a good qualitative and quantitative agreement with experiments. Given the direction (attraction), the range ($\sim \mu\text{m}$) and the distance dependence ($\sim 1/S^5$) of the observed inter-particle force, we interpret the force as being caused by quadrupolar deformations of the fluid-fluid interface induced by particle surface roughness.

The magnitude of the attractive force can be modulated by the addition of a cationic polymer in the oil phase, where the amine groups of the polymer exposed to the water phase (with positive charges) interact electrostatically with the carboxylic groups (with negative charges) on the surface of the particles.³⁵ The increase of the attractive force for increasing concentrations of polymer in the oil phase can be interpreted as an increase of the particle three-phase contact angle, as proposed by Stamou *et al.*⁷⁰ and confirmed by measurements of contact angle (see section 4.E). Surprisingly, for a fixed polymer concentration the magnitude of the attractive force shows no dependence on the amount of polymer adsorbed to the fluid-fluid interface. The results suggest that capillary forces are equilibrated at the early stages of interfacial ageing and thereafter the polymer layer hinders further attachment of polymers to the particle surface, while the polymers still

contribute to strong changes of interfacial viscosity.

The IPM technique appeared to be a very versatile method to disentangle conservative inter-particle forces from dissipative effects caused by interface ageing. To our knowledge, this represents the first study of a fluid-fluid system far from equilibrium, which gives new opportunities. The availability of magnetic colloids with a tailored surface roughness would allow one to investigate the relation between attractive capillary forces and surface structures. In particular, the IPM technique could be used to study capillary interactions at different length scales by modulating the strength of the dipole-dipole force. In the far-field ($S \gg 2R$), capillary interactions can be described as a superposition of leading-order capillary multipoles, with the quadrupolar term being the leading one.^{39,70,74} In the near-field ($S \approx 2R$), this approximation may not hold as the interaction is dominated by the shape details of the undulated meniscus around the particle and higher orders may appear. Moreover, the rotational dynamics could be studied by coupling fluorescent tags on the surface of the particle.

A current issue of particle-based microrheology is that for low Boussinesq number, the interfacial drag coefficient of particles is sensitive to changes of the particle contact angle.^{26,67} Variations of the capillary attraction, together with surface tension measurements (e.g. with a Langmuir trough), could be used to indirectly determine changes of the particle contact angle, thus obtaining reliable rheological information. With this information available, IPM could then be applied to study the dynamics of interface ageing, using polymers with different molecular weights as the dynamics is strongly dependent on chain length.⁴⁶ We foresee that IPM will help scientists to shed light on the complex interaction of micro- and nanoparticles at fluid-fluid interfaces for a wide range of materials, with particular interest for systems out of equilibrium.

Appendix

4.A Validation of Brownian Dynamics (BD) simulations

In order to validate the numerical method described in section 4.2.2, we first performed BD simulations of the 2- and 3-dimensional Brownian diffusion of particles experiencing a constant drag coefficient $f = 1 \cdot 10^{-8}$ Ns/m, without hydrodynamic interactions. The diffusion coefficient D of particles can be computed from the mean-squared displacement (MSD) of simulated trajectories

$$\langle (\mathbf{x}(t + \tau) - \mathbf{x}(t))^2 \rangle = 2dD \cdot \tau \quad (4.8)$$

where $\mathbf{x}(t)$ is the position of the particle at time t , τ is the lag time, and $d = 2, 3$ is the dimensionality of the system.²⁵ Then, the diffusion coefficient D can be related to the drag coefficient f via the Einstein equation $D = k_B T / f$. We performed BD simulations with a time step of $\delta t = 10^{-5}$ s, and generated trajectories for a total time of 10 s. The MSD curves were computed for $\tau_{max} = 2$ s. From simulations performed in 2 and 3 dimensions we obtained $f_{sim}^{2D} = (1.03 \pm 0.01) \cdot 10^{-8}$ Ns/m (2390 trajectories) and $f_{sim}^{3D} = (1.02 \pm 0.01) \cdot 10^{-8}$ Ns/m (1990 trajectories), in agreement with the input parameter.

As a second method, we followed the approach proposed by Northrup *et al.*,²¹⁷ used to calculate the diffusion-influenced bimolecular reaction rates in a 3-dimensional system. The diffusion-influenced reaction rate between two identical spheres of radius R can be expressed as²¹⁷

$$k = k_D(S)p \quad (4.9)$$

where $k_D(S)$ is the rate constant (expressed in units m^3/s) governing the rate at which particles achieve center-to-center separation S , and p is the probability of reaction upon contact. Assuming $p = 1$, if no forces or hydrodynamic interactions are present, then the rate constant is given by the Smoluchowski result

$$k_D^0(S) = 4\pi D_0 S \quad (4.10)$$

In the presence of an interaction potential $U(x)$ and hydrodynamic interactions, both centrosymmetric, the more general result of eqn (4.9) is given by

$$k_D(S) = \left(\int_S^\infty dx \left[\frac{\exp[U(x)/k_B T]}{4\pi x^2 D(x)} \right] \right)^{-1} \quad (4.11)$$

Brownian Dynamics (BD) simulations can be used to estimate the reaction rate constant between pair of particles. In principle one would require to generate a large number of trajectories diffusing from large separations to the reaction surface, but this is highly unpractical and computationally infeasible. Northrup *et al.* proposed an alternative method based on the estimation of the particle encounter rate β and recombination probability Ω from BD trajectories. Here, we summarize the main results useful for our analysis.

A pair of particles is separated at an initial arbitrary distance $S = b$ and then allowed to diffuse according to eqn (4.7). The simulation is terminated upon reaction, i.e for $S = 2R$, or if the particle diffused to a distance $S > q > b$. From the resulting encounter rate β (computed on the finite domain $S \in [b, q]$) it is possible to determine the reaction rate from the relation

$$k = \frac{k_D(b)\beta}{1 - (1 - \beta)\Omega} \quad (4.12)$$

where $\Omega = k_D(b)/k_D(q)$ can be computed using eqn (4.11). The values obtained for k are independent on the choice of b and q .

We simulated the 3-dimensional diffusion of pairs of particles in the presence of a potential with the functional form as of eqn (2.22), with $m_A = m_B = 2$ (i.e. a quadrupolar interaction) and $\phi_A = \phi_B = 0$ (rotational independent). The resulting interacting force is described by eqn (4.3), which we rewrite here for convenience

$$F_{cap} = -F_0 \left(\frac{2R}{S} \right)^5, \quad \text{with } S \geq 2R \quad (4.13)$$

where F_0 is the magnitude of the capillary force at shortest separation, i.e. $S = 2R$. In these simulations we neglect hydrodynamic interactions between particles and we consider a frequency independent drag coefficient, hence $D(x) = D = k_B T / f$.

The encounter rate β is computed from the simulations of 1000 trajectories performed with the same set of initial conditions. Then, the reaction rate k is computed using eqn (4.12). In Fig. 4.5 we show the reaction rates k obtained from different values of the capillary coefficient F_0 . The results obtained from BD simulations are in agreement with the expected analytical solution of eqn (4.11), thereby confirming the validity of our numerical method.

4.B Analysis of BD simulations of particle attraction trajectories

Particle trajectories always contain thermal (Brownian) noise, which may mask an underlying interaction potential. In order to disentangle thermal noise and particle attraction at the water-oil interface, we performed BD simulations in the presence of an inter-particle attractive force as described by eqn (4.13). The motion of the particles due to the attractive force is counterbalanced by the drag force, which for a continuous, nonelastic Newtonian medium, and under no-slip conditions can be expressed as $F_{drag} = \frac{f}{2} \frac{dS}{dt}$. The resulting equation of motion is given by eqn (4.4), which we rewrite here for convenience

$$S^6 = -\frac{12F_0(2R)^5}{f} \cdot (t - t_0) + S_0^6 \quad (4.14)$$

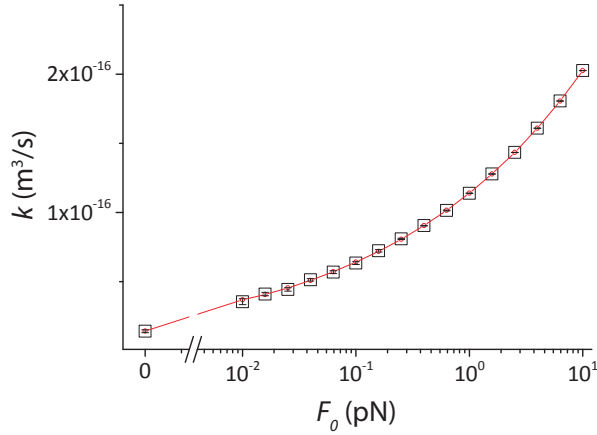


Figure 4.5: Reaction rate constant k as a function of the closest-proximity capillary force F_0 , obtained from BD simulations with interaction force as in eqn (4.13). Particles are initiated at a distance $b = 8 \mu\text{m}$ and simulations, performed with a time step of $20 \mu\text{s}$, are terminated if $S = 2R$ (reaction), or if $S > q = 10 \mu\text{m}$ (no reaction). The open black squares and error bars represent the mean and standard deviation of 6 simulation runs (every simulation run consist of 1000 trajectories, for a total of 6000 trajectories). The red lines represents the analytical solution according to eqn (4.11) with $S = 2R$.

With this equation it is possible to extract F_0 from particle trajectories, once the drag coefficient f is known. The results of BD simulations (Fig. 3b), show curves expressing $f \cdot \bar{S}^6$ with two distinct regions. At large separations, the attractive interaction is weak and the motion is dominated by thermal noise. At short separations, the attractive force dominates and trajectories approach to the expected behaviour of eqn (4.14). In order to correctly estimate F_0 , we consider only the linear part of the $f \cdot \bar{S}^6$ curves close to approach time $t_{appr} = 0 \text{ s}$ (see insets of Fig. 4.3b). In order to assess the accuracy of this procedure, we introduce the parameter R_{F_0} , defined as

$$R_{F_0} = \left(\frac{F_0^{sim} - F_0}{F_0^{sim}} \right) \cdot 100\% \quad (4.15)$$

With this procedure, and considering f as a known fixed parameter, we obtained estimates for F_0 with an accuracy of at least 15% with respect to the input parameters depending on the magnitude of F_0 (see Table 4.D.1).

For a given starting distance between particles, the fraction of trajectories that show full approach, i.e. achieve $S = 2R$, depends on the magnitude of the interacting force F_0 . Using the concepts presented in the previous section, we can determine the size of a "capture radius" R_{cap} , which represents the size of the region required to obtain the same association rate as in the case of free diffusion.²¹⁹ In other words, for a given value of k_D computed by eqn (4.11), we compute the effective radius that the particle would have in the absence of any attractive force in order to achieve the same reaction rate,

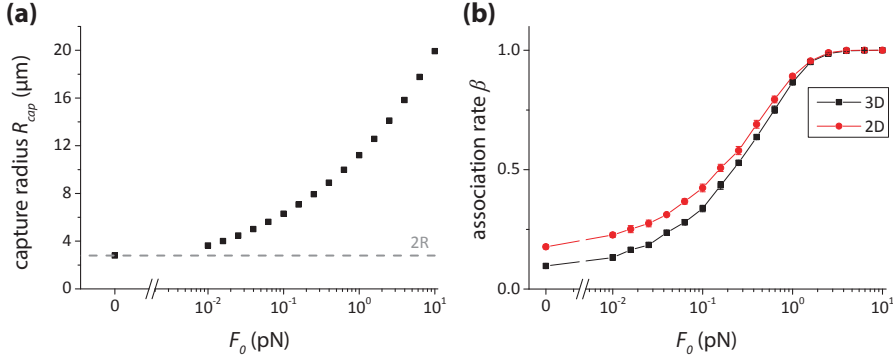


Figure 4.6: **(a)** Capture radius R_{cap} as a function of the closest proximity capillary force F_0 . The gray dashed line represents the capture radius for particles diffusing in the absence of any force, which correspond to the sum of the radii of the two particles. **(b)** Association rate β for simulations performed in 3 dimensions (red circles) and in 2 dimensions (black squares). Values of β are computed from 1000 simulated trajectories, with initial separation $b = 8 \mu\text{m}$ and cutoff distance $q = 10 \mu\text{m}$. Every dot is obtained from the average of 6 simulation runs (for a total of 6000 trajectories), with the standard deviation as error bars. Lines are a guide to the eye.

i.e. $k_D^0 = k_D$. Typical values of the capture radius are shown in Fig. 4.6. With the values of F_0 used in the simulations shown in Fig. 3 (b1) and (b2), we expect a capture radius of $R_{cap} \approx 6 \mu\text{m}$ and $R_{cap} \approx 16 \mu\text{m}$ respectively. However, this reasoning is only applicable for a system with spherical symmetry, i.e. for the 3 dimensional diffusion of particles with a centrosymmetric potential. When a particle is diffusing in 2 dimensions – as for the diffusion of particles trapped at the water-oil interface – these conditions don't hold anymore and it is not possible to obtain an exact solution for the steady-state rate constant.²²⁰ Nonetheless, the reaction rate in 2 dimensions provides an upper bound estimate of the true rate constant. This is also shown by our numerical calculations of the association rates β , with higher values for simulations performed in 2 dimensions as compared to 3 dimensions (Fig. 4.6, Table 4.B.1). The range of the attractive interaction

Table 4.B.1: Results of BD simulations. Values of the three phase contact angle θ were calculated according the model proposed by Stamou *et al.*⁷⁰ (see eqn (4.2)), computed for $\phi_A = \phi_B = 0$, $\gamma = 20 \text{ mN/m}$, $R = 1.4 \mu\text{m}$, and $H_2 = 50 - 150 \text{ nm}$.

F_0/pN	β_{3D}	β_{2D}	θ/deg
0.1	0.34	0.42	9.0 - 5.2
1	0.87	0.89	16.1 - 9.2
10	1.00	1.00	29.6 - 16.6

(capture radius) and the magnitude of the capillary force F_0 used in these simulations are in qualitative and quantitative agreement as compared to experiments of particle attraction performed at the water-oil interface (see Fig. 4.2).

In order to test the sensitivity of our analysis method to discriminate between different orders of the attractive interaction, we performed BD simulations with an interaction force

with a scaling law as

$$F(S) = F_0 \left(\frac{2R}{S} \right)^n \quad \text{with} \quad n = m_A + m_b + 1 = 4, 5, 6, \quad (4.16)$$

and, for a given n , the same initial conditions (F_0, S_0). We then analyzed the results considering the attraction as the result of quadrupolar induced deformation of the interface, i.e. by fitting the linear part of curves expressing $f \cdot \bar{S}^6$ to eqn (4.14) starting from $t_{appr} = 0$.

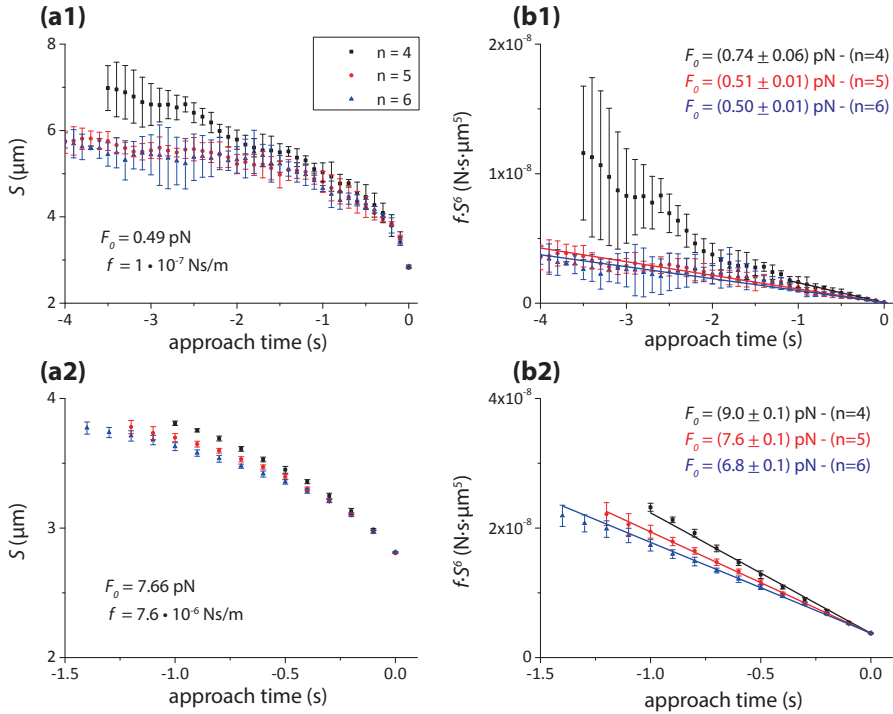


Figure 4.7: BD simulations of capillary attraction between a particle pair in the presence of an attractive force that scales with distance as $\sim 1/S^n$, with $n = 4, 5, 6$. (a) Center-to-center separation S as a function of particle approach time. The points represent the mean and standard deviation of 3 attraction curves. (b) Normalized attraction curves $f \cdot \bar{S}^6$ as a function of particle approach time of the same curves as shown in (a). The solid lines are a fit according to eqn (4.14) of only the linear part of the curve for approach times close to zero.

The simulated trajectories show small differences between different values of n (Fig. 4.7a). The curves in Fig. 4.7b show that for a low interacting force (panel b1), it is possible to determine a linear region close to $t_{appr} = 0$ and to obtain accurate results from the fit according to eqn (4.14) regardless the value of n . Only for $n = 4$, the estimated value of F_0 is higher as compared to the simulated one. For a higher interacting force (panel b2), only a careful analysis of the residuals allows one to find systematic variations

from eqn (4.14) for n equal 4 and 6, in particular at large separations. Therefore, our analysis method can retrieve the right scaling order n only for F_0 greater than a few pN.

In our experimental system, we can exclude $n = 4$ as it would require one of the two particle to induce a dipolar deformation of the interface ($m = 1$). This is not the case of this study, as discussed in section 4.4.1. Higher interaction orders ($m_A + m_B + 1 = n > 5$) may be present, but only relevant at short separations. At large distances, the slowest decaying term of the inter-particle force is $n = 5$, i.e. a quadrupolar capillary interaction.

4.C Quantification of drag coefficient in the presence of attractive capillary interaction

In order to quantify the capillary force F_0 from eqn (4.14), it is necessary to quantify the drag coefficient f of particles at the water-oil interface. This can be done using the intra-pair magnetophoresis (IPM) method, where f is quantified from the displacement of pairs of particles using well controlled magnetic dipole-dipole forces (see section 4.2.2). During magnetic separation of the particles, both attractive capillary forces and drag forces oppose to the motion of the particles, with a total force expression described by eqn (4.1).

We evaluate the accuracy of the IPM method in retrieving the value of f in the presence of capillary forces, by performing BD simulations of pairs of particles obeying eqn (4.1). The dipole-dipole force F_{dd} during magnetic repulsion can be approximated by the equation¹⁸⁹

$$F_{dd} = \frac{3\mu_0 m_{d,1} m_{d,2}}{4\pi S^4} \quad (4.17)$$

where μ_0 is the vacuum permeability, and $m_{d,i}$ is the magnitude of the induced magnetic moment (in units Am^2) of particle i , which we assume to be identical for both particles ($m_{d,1} = m_{d,2}$). In the absence of capillary forces, one can use eqn (4.5) to compute f (see section 4.2.2), which we rewrite here for convenience

$$S(t)^5 = \frac{15\mu_0}{2\pi} \cdot \frac{m_{d,1} m_{d,2}}{f} \cdot (t - t_0) + S_{0,dd}^5 \quad (4.18)$$

In the presence of capillary forces the equation of motion can be expressed as eqn (4.6), that is

$$\frac{f}{2} \frac{dS}{dt} = F_{0,dd} \left(\frac{2R}{S} \right)^4 - F_0 \left(\frac{2R}{S} \right)^5 \quad (4.19)$$

where for ease of notation we introduced the closest proximity magnetic force $F_{0,dd} = \frac{3\mu_0 m_1 m_2}{4\pi(2R)^4}$ in analogy with the notation we used for the expression of the capillary force. In Fig. 4.8 we show how the magnetic force and the capillary quadrupolar force scales with inter-particle distance. In our magnetic repulsion experiments $F_{0,dd} \simeq 20$ pN, while capillary forces are maximally a few pN. As shown in Fig. 4.8, capillary forces are relevant only at short separation distances as they decay faster with distance as compared to magnetic forces.

In order to study the influence of attractive capillary forces on the quantification of the drag coefficient f , we analyzed the simulated trajectories with $F_0 = 0$ and with F_0

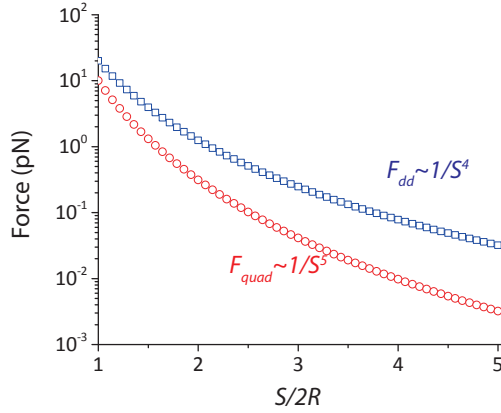


Figure 4.8: Magnetic force (blue squares) and capillary quadrupolar force (red circles) as a function of inter-particle distance. Magnetic and capillary forces are computed using $F_{0,dd} = 20$ pN and $F_0 = 10$ pN respectively.

at the input parameter, hence using eqn (4.18) and eqn (4.19) respectively. Example are shown in Fig. 4.9a. Then we evaluate the accuracy of our analysis method in retrieving the simulated drag coefficient f_{sim} via the parameter R_f , defined as

$$R_f = \left(\frac{f_{sim} - f}{f_{sim}} \right) \cdot 100\% \quad (4.20)$$

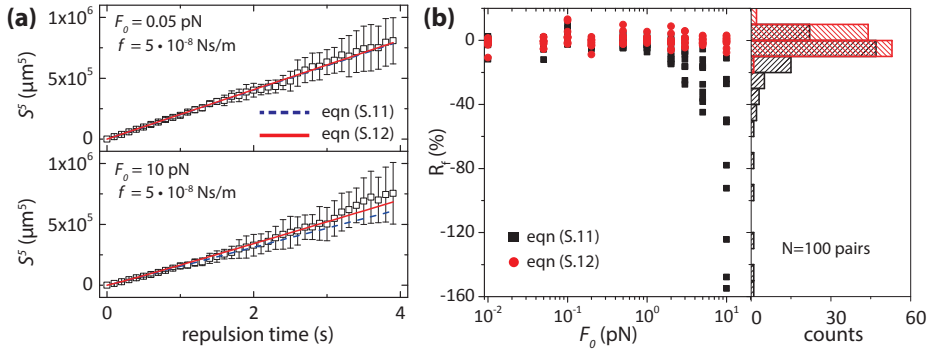


Figure 4.9: Influence of attractive capillary forces on the quantification of drag coefficient, studied with BD simulations. (a) Trajectories of magnetic repulsion simulations plotted as S^5 as a function of time. Each symbol represent the mean and standard deviation of 6 trajectories. The dashed blue line represent a fit according to eqn (4.18), thereby neglecting the influence of capillary forces. The solid red line represents a fit according to eqn (4.19). (b) Relative error R_f of the estimation of f as a function of F_0 . Simulations were performed for a range of f between $1 \cdot 10^{-8}$ and $5 \cdot 10^{-4}$ Ns/m.

Results in Fig. 4.9b show that F_0 influences the estimation of f when F_0 becomes comparable to the magnetic force, e.g. for $F_0 > \frac{F_{0,dd}}{2R}S$ (with $S \geq 2R$). When the capillary force F_0 is taken into account in the analysis and considered as a fixed parameter, it is possible to estimate f with an accuracy that is less than 4% (see Table 4.D.1), represented as the standard deviation of the distribution of R_f as shown in Fig. 4.9b.

4.D Iterative quantification of f and F_0

A typical attraction experiment of particles at the water-oil interface consists of two steps. First, pairs of particles are magnetically separated of a few μm . Then, particle trajectories are recorded in the absence of the magnetic field, as shown in Fig. 4.1c. In the case of magnetic separation, the particle trajectories are described by eqn (4.19). In the case of particle spontaneous attraction, the particle trajectories are described by eqn (4.14). In order to estimate the particle drag coefficient f and the capillary force F_0 from eqns (4.19) and (4.14), both quantities need to be considered. Therefore, we iteratively estimate f from magnetic repulsion trajectories by considering F_0 as a fixed parameter of eqn (4.19). Then, we estimate F_0 from spontaneous attraction trajectories by considering the previously estimated value of f as a fixed parameter of eqn (4.14). The iteration is performed until the difference of both quantities between two consecutive iterations becomes less than 10^{-8} .

We tested the accuracy of this analysis method on the numerical data generated by BD simulations, as presented in sections 4.2.2, 4.B and 4.C. With this approach, we were able to estimate values of f and F_0 with an accuracy of at least 9% and 30% respectively with respect to the input parameters (see Table 4.D.1). In all cases, the precision, defined as the average of R_f and R_{F_0} , was about 2%. These results confirm the validity of our analysis method.

Table 4.D.1: Evaluation of the analysis method as described in section 4.2.2 using BD simulations. R_{F_0} and R_f are computed with eqn (4.15) and eqn (4.20) respectively and values are expressed as the standard deviation obtained from N simulations.

F_0/pN	$R_{F_0}/\%$ (f fixed)	$R_f/\%$ (F_0 fixed)	$R_{F_0}/\%$ (iterative)	$R_f/\%$ (iterative)
≤ 1	15% ($N = 132$)	4% ($N_{\text{tot}} = 100$)	30% ($N = 116$)	9% ($N = 116$)
$1 < F_0 \leq 5$	8% ($N = 110$)	4% ($N_{\text{tot}} = 100$)	16% ($N = 97$)	9% ($N = 97$)
> 5	6% ($N = 21$)	4% ($N_{\text{tot}} = 100$)	-	-

4.E Contact angle measurement of particles using z-stack of images

Magnetic particles with a carboxylic functionalized surface adsorb to a water-oil interface only in the presence of a cationic polymer dissolved in the oil phase as the result of electrostatic interactions.³⁵ This in turn modulates the particle three-phase contact angle.²¹³ To study how contact angle depends on polymer concentration and time, we measured the contact angle of particles at the water-oil interface using a method based on the acquisi-

tion of images of the particle at different focal planes. A similar approach was previously developed by Mohammadi and coworkers.¹⁰⁶ However, the particles used in this study are too small ($2R \approx 2.8 \mu\text{m}$) to be able to resolve their vertical position with respect to the fluid-fluid interface by microscopy. Therefore, we measured the contact angle on larger particles, but with the same surface chemical functionality as the small ones (CFM-300-5 carboxylic acid, ferromagnetic, nominal size $28 - 34.9 \mu\text{m}$, Spherotech). Samples were placed on a motorized stage and digital images (30x objective, $NA = 0.5$) were acquired at different focal planes (Fig.4.10a), with a vertical interval of $\Delta z = 0.4 \mu\text{m}$. For every

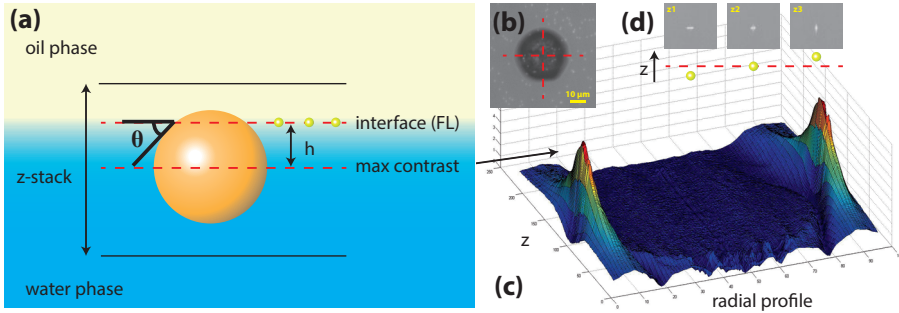


Figure 4.10: Method to determine the particle three-phase contact angle θ from z-stack of images. (a) Images of a particle were taken at different focal planes using a motorized stage with vertical steps of $\Delta z = 0.4 \mu\text{m}$. (b) Images were acquired combining transmission and fluorescent imaging, so that the magnetic particle resulted as a dark disk and fluorescent nanoparticles as bright dots. For every image the mean radial intensity profile was extracted (red dotted lines). (c) Form the 3D graph of the radial profile as function of height it is possible to extract the position z_p of maximum contrast. (d) The position of the interface z_{int} is determined from the focal plane where the fluorescent nanoparticles are present using astigmatic lenses, so that the eccentricity of the image of the particle depends on z . Thus, from $h = z_{int} - z_p$ the particle contact angle can be computed using eqn (4.21).

z position, the mean radial intensity profile of the particle was extracted (red line in Fig. 4.10b). From a stack of z -radial profiles it is possible to locate the height z_p where the contrast of the particle is maximum, corresponding to its equatorial plane (Fig. 4.10c). The position of the interface z_{int} was determined by adsorbed fluorescent nanoparticles (FluoSpheres, carboxylic acid, yellow/green, $0.2 \mu\text{m}$ diameter) at the interface, whose position was determined using astigmatic lenses. Hence the contact angle can be determined by geometrical considerations, yielding the relation:

$$\theta = \cos^{-1} \left(\frac{h}{R} \right) \quad (4.21)$$

where $h = z_{int} - z_p$.

In order to calibrate the method for particle height determination, particles were deposited on a glass substrate in PBS buffer. The small fluorescent particles interact non-specifically with the glass surface giving the position of the interface (glass-water), while

the big particles sediment at the surface. The data in Fig.4.11a show a relative height

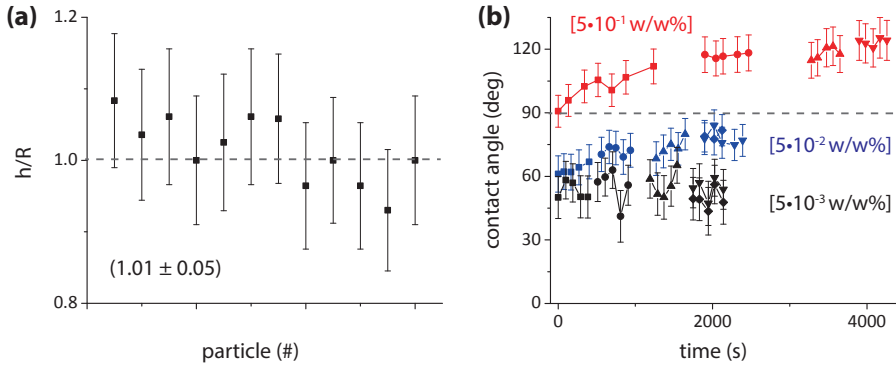


Figure 4.11: Measurements of particle three-phase contact angle θ from z -stack of images. **(a)** Experiments performed with large ferromagnetic particles ($2R \approx 33 \mu\text{m}$) on a glass substrate show that the ratio between the height h and the particle radius R is close to unity, with a weighted standard deviation of 5%. **(b)** Contact angle measurement of $2R \approx 33 \mu\text{m}$ ferromagnetic particles at the water-oil interface as a function of polymer adsorption time and different concentrations of cationic polymer dissolved in the oil phase. For every polymer concentration (color), each symbol represents measurements performed on the same particle. The experimental error bars are computed considering the uncertainties of the height of the interface z_{int} , the height z_p relative to the maximum contrast of the particle, and the radius R of the particle to be $\Delta z_{int} = 2 \mu\text{m}$, $\Delta z_p = 2 \mu\text{m}$, and $\Delta R = 1 \mu\text{m}$ respectively.

$h/R = (1.0 \pm 0.05)$, so that the focal plane at which the contrast of the particle is maximal corresponds to the equatorial plane of the particle with an accuracy of 5%.

We apply now this method to measure the contact angle of large carboxylic particles ($2R \approx 33 \mu\text{m}$) trapped at the water-oil interface as a function of polymer concentration and time, with the cationic polymer dissolved in the oil phase. Experiments were performed right after the interface was formed. Results in Fig. 4.11b show that the three-phase contact angle increases with increasing polymer concentration in the oil phase, with a transition from hydrophilic to lyophilic for increasing polymer concentrations. The timescale for the particle to reach the equilibrium contact angle depends on polymer concentration, with relaxation times on the order of several minutes. The slow relaxation times can be attributed to the pinning of the three-phase contact line on surface heterogeneities of the particle, as previously suggested by several authors^{51,52} and recently reviewed by us.⁹⁴

These results confirm that the contact angle of large particles ($2R \approx 33 \mu\text{m}$) depends on the polymer concentration in the oil phase and on time. These measured values cannot be directly used to describe the contact angle of the small particles ($2R \approx 2.8 \mu\text{m}$) used for the main study. However, they support our hypothesis that the increasing values of the capillary attraction force F_0 observed for increasing polymer concentration (Fig. 4b) is the result of an increase of the particle contact angle.

With the model proposed by Stamou *et al.*,⁷⁰ we can estimate the contact angle that the particle would have in order to generate a certain capillary force for a fixed amplitude of the corrugation of the three-phase contact line around the particle. These calculations, performed for the particles used in the main study ($2R \simeq 2.8 \mu\text{m}$), are shown in Table 4.B.1. These values are in a similar range as the one observed for the large particles and a polymer concentration $c_P = 5 \cdot 10^{-3}$ w/w%.



5

Dynamic wetting of single particles at fluid-fluid interfaces

The fundamental molecular and microscopic properties of materials leading to dynamic wetting and relaxation effects have been subject to numerous studies in the past decades, but a thorough understanding is still missing. While most previous experiments utilize fluids deposited on planar substrates, this Chapter focuses on an alternative method based on single colloidal particles: colloidal particles have the ability to strongly interact with fluid-fluid interfaces and the behavior strongly depends on the surface properties of the particles and the fluids used. Recent progress in the manipulation and synthesis of colloidal particles with well-defined surface properties and shapes makes them ideal candidates to probe the fundamental surface properties leading to dynamic wetting effects. In this Chapter we propose a new experiment based on the rotation of ferromagnetic particles at an aqueous-two-phase-system (ATPS) interface. Particles are interrogated with an out-of-plane rotating magnetic field. The rotational motion trajectories show wetting patterns that depend on the particle surface properties. We interpret the results with a model that includes dissipative effects due to contact line friction and elastic contributions due to interface deformation.^a

^aParts of this Chapter have been published in: S. Cappelli, Q. Xie, J. Harting, A.M. de Jong, and M.W.J. Prins, Dynamic wetting: status and perspective of single particle based experiments and simulations. *New Biotechnology*, 32(5):420-432, 2015.

5.1 Introduction

In Chapter 2 we focused on unanswered questions about the origin and scaling relationships of dynamic wetting. From an experimental point of view, dynamic wetting plays an important role in the adsorption process of colloids at fluid-fluid interfaces. From a fundamental point of view there is a need to understand the mechanisms underlying dynamic wetting processes, over a wide dynamic range in space and time. One important challenge is to gain access to the small scale of a moving contact line. This problem may be addressed by studying wetting on single colloidal particles at fluid-fluid interfaces. The knowledge of dynamic wetting of single particles is important for technological applications in order to be able to predict the behavior of ensembles of particles and to scale up systems.

Optical tweezers and colloidal probe AFM are suitable techniques to study relaxation to equilibrium of colloids with different surface functionalization and sizes (1-100 μm), and for different systems (e.g. water-oil and water-air interfaces). To move a particle out of its equilibrium position forces normal to the interface or torques can be applied. Forces in the range of several hundreds of pN to μN are typically required. Optical tweezers provide a 'contact-free' actuation method that can apply both translational and rotational forces. Vertical forces range from 0.1 pN to hundreds of pN, but for such high forces a high intensity laser is required, which might heat the sample changing the local properties of the interface or even melt or destroy the particle. Torques can only be applied to optically anisotropic particles,²²¹ in the range of $1 - 10^5$ pN nm. AFM can apply translational forces from a few pN to hundreds of nN, depending on the cantilever spring constant,^{81, 222} but it cannot apply torques.

Another technique that allows to apply forces and torques is magnetic tweezers. Magnetic tweezers use magnetic fields and magnetic field gradients to manipulate magnetic particles.^{12, 34, 81} A magnetic particle in a magnetic field gradient experiences a translational force that depends on the magnitude of its magnetic moment and of the gradient. In a spatially uniform, but rotating, magnetic field, a magnetic particle does not experience a translational force but experiences and exerts a torque. Magnetic fields can be controlled by electrical currents which gives the possibility to create magnetic fields with different magnitudes and orientations. Particles can be imaged using conventional digital microscopy techniques to resolve their position. Typical forces range from few pN to tens of nN⁸¹ depending on the magnetic properties of the particles and the source of the magnetic fields. Typical torques range from 10 to 10^7 pN nm (for particles with a magnetic moment between 10^{-16} and 10^{-13} A·m² and magnetic fields of 0.1-100 mT^{12, 88}).

The main advantage of magnetic tweezers is the possibility to actuate the probe with 6 degrees of freedom (3 translational and 3 rotational). By measuring the translation and angular orientation of the particle it is possible to measure the response of the system upon external stimuli. This method has been exploited for example for interfacial microrheology studies,^{26, 55} as demonstrated in Chapter 3. Translation can be resolved with microscopic techniques; rotation can be resolved if optical features are present on the rotating object, such as holes on a flat disk,⁶⁴ or fluorescent tags on a magnetic particle.^{12, 88}

Here we propose an attractive alternative based on magnetic tweezers to study wetting

at small scales. A magnetic particle trapped at a fluid interface is interrogated with different magnetic torques. The torque is applied in such a way to displace the three-phase contact line on the surface of the particle, so called *out-of-plane* rotation, as sketched in Fig. 5.1. We performed experiments at a water-decane interface and at an aqueous-two-

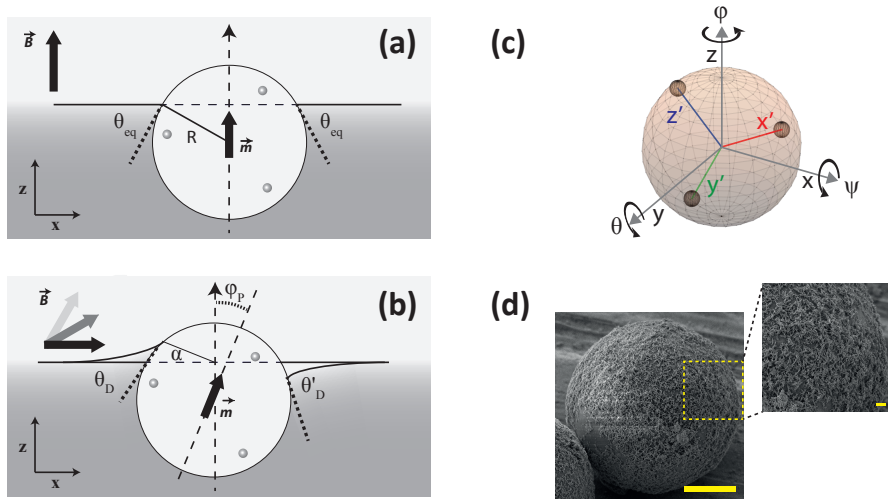


Figure 5.1: Study of dynamic wetting of single particles at a fluid-fluid interface, by out-of-plane rotation. **(a)** A magnetic particle with radius R is trapped at a fluid-fluid interface; optical labels (e.g. fluorescent nanoparticles) on the particle surface allow for orientation tracking. The magnetic moment \vec{m} and magnetic field \vec{B} are aligned and normal to the interface. **(b)** In the presence of a magnetic field parallel to the interface the particle experiences a torque. We define the particle angular orientation φ_p as the angle between the magnetic moment and the vertical axis z . **(c)** Coordinate system for the tracking of the 3D rotation of a particle. The particle-fixed coordinate system $x'y'z'$ is rotated according to the extrinsic rotation matrix of eqn (5.5). As an example we show a rotation with Euler angles $\psi = -15^\circ$, $\theta = -30^\circ$, and $\varphi = 0^\circ$. **(d)** Scanning electron micrographs of a $33 \mu\text{m}$ ferromagnetic particle used for this study. The particle (large image) has a polystyrene core, on top of which chromium dioxide crystals are deposited to make them ferromagnetic (enlarged image). The scale bars are $10 \mu\text{m}$ and $1 \mu\text{m}$ in the large and enlarged image respectively. **(a)** and **(b)** have been adapted and reprinted from Ref.⁹⁴ Copyright (2015), with permission from Elsevier.

phase-system (ATPS) interface, which represents a high-surface tension interface and a low-surface tension interface respectively. From the study of the particle angular orientation as a function of time we observed different behaviors depending on the particle surface properties and on the fluid-fluid interface used. We interpret the results with a model that includes dissipative effects due to contact line friction and elastic contributions due to interface deformation.

5.2 Materials and methods

5.2.1 Preparation of fluid-fluid interfaces

We performed experiments of *out-of-plane* rotation of particles at a fluid-fluid interface, for two material systems. A water-oil interface was prepared using decane as the oil phase (Sigma-Aldrich), as received from the supplier, and ultra-pure water (resistivity $> 18.2 \text{ M}\Omega\text{-cm}$) as the aqueous phase. An aqueous-two-phase-system (ATPS) interface was prepared by mixing 8 w/w% of polyethylene glycol (PEG, $m_w = 7000 - 9000 \text{ Da}$, BioUltra, Sigma-Aldrich) and 15 w/w% of dextran (Dextran from *Leuconostoc* spp., $m_w = 450 - 650 \text{ kDa}$, Sigma-Aldrich) in ultra-pure water. The weight percentage is computed with respect to the final weight of the mixture. The mixture was prepared in a plastic test-tube and the interface was allowed to equilibrate overnight. The system phase separates, with a bottom phase that is rich with the more hydrophilic and denser dextran phase, and a top phase that is rich with the less dense and more hydrophobic PEG.^{223,224} The bottom phase was carefully extracted from a pierced hole at the bottom of the test tube, while the top phase was extracted using a pipette. The two phases were then centrifuged at 5000 r.p.m. for 15 min to remove counter-polymers excessively dissolved in each phase. The stock solutions of PEG and dextran phases were stored at 4°C .

We created a flat water-oil interface using a custom made fluid cell, with a design similar to the one shown in Chapter 3 (see section 3.A). The fluid cell consists of two circular aluminum rings. The outer ring, with a bottom hole to host a glass coverslide (19 mm diameter, Thermo ScientificTM), contains the inner ring with a central hole with sharp edges where the bottom phase pins. Prior to any measurement all the fluid cell components (inner rings and glass cover slides) were washed in a sonic bath for 10 min first in acetone and then in isopropanol, ethanol (Sigma Aldrich), and finally in ultra-pure water. For creation of a fluid-fluid interface, the top phase is gently deposited on top of the bottom phase. For a water-oil interface, we dispersed magnetic particles in the aqueous phase and brought the particles to the interface by shortly applying a vertical magnetic force with a permanent magnet. For an ATPS interface, particles were gently deposited in close proximity of the interface from the top phase, which then sedimented to the interface by gravity. The particles remained at the interface for the whole duration of the experiments. The position of the particles within the fluid cell was determined by the position of the focal plane of the microscope with micrometer accuracy.

5.2.2 Particle functionalization

We performed out-of-plane rotation experiments using ferromagnetic particles with a diameter of about $33 \mu\text{m}$ (CFM-300-5 carboxylic acid, ferromagnetic, nominal size $28 - 34.9 \mu\text{m}$, Spherotech). The particles were used both with the as-supplied surface functionalization (carboxyl-coated, which we abbreviate for convenience with **FM-C**), and with a surface functionalization using Protein G (Thermo Scientific, **FM-G**), tryptophan (Sigma Aldrich, **FM-T**) and with fluorescent nanoparticles (FluoSpheres, Invitrogen, biotinylated, yellow/green, $0.2 \mu\text{m}$ diameter; **FM-FL-G**).

We used EDC-NHS chemistry to functionalize carboxylated particles with **FM-G**

and **FM-T**. Particles were washed twice with 25 mM 2-N-morpholinoethanesulfonic acid (MES) at pH 5. To activate the carboxylic groups, the particles were suspended in 50 μL of 25 mM MES buffer containing 50 mg/mL of 1-Ethyl-3-(3-dimethylaminopropyl)carbodiimide (EDC) and 50 μL of 25 mM MES buffer containing 50 mg/mL of N-Hydroxysuccinimide (NHS), and incubated at room temperature for 30 min with slow tilt rotation. The excess of EDC and NHS were removed by washing the particles twice with MES buffer. Then, the surface of the particles were functionalized by adding 100 μL of 25 mM MES buffer containing $\sim 1 \mu\text{M}$ of ligand (e.g. protein G and tryptophan) and incubating the solution for 2 hours at 4°C under slow tilt rotation. To quench the reaction, the supernatant were removed and the particles were suspended in 100 μL of 150 mM phosphate buffered saline (PBS) solution at pH 8 containing 50 mM of ethanolamine for 1 hour. Finally, the particles were washed in PBS buffer containing 0.5 w/w% of BSA and 0.01 w/w% of Tween 20. All the chemicals were provided by Sigma Aldrich.

To functionalize particles with fluorescent nanoparticles (**FM-FL-G**), we used a two step protocol. We first functionalized the particles with anti-biotin IgG antibodies by incubating the particles for 50 min (1:40 volume) with a 150 mM PBS solution (7.4 pH) containing 13 pM anti-biotin IgG antibodies, 1 mg/mL of BSA and 0.01 w/w% of Tween 20. Then, an excess of biotinylated fluorescent nanoparticles were added to the solution for 20 min, which specifically bound to the antibody on the surface of the particles.

Prior to experiments, ferromagnetic particles were magnetized by applying a magnetic field of at least 100mT using a set of Helmholtz coils, enough to overcome the coercive magnetic field of the particle.

5.2.3 Out-of-plane rotation of particles

When a particle with magnetic moment \vec{m} is exposed to a spatially uniform magnetic field \vec{B} , it exerts a torque, according to the equation

$$\vec{\tau} = \vec{m} \times \vec{B} \quad (5.1)$$

Equation (5.1) shows that the torque will drive the magnetic moment to align with the direction of the applied magnetic field, as sketched in Fig. 5.1a,b. If a uniform and rotating magnetic field is applied with the rotation axis in the xy -plane, e.g. along the y -axis (Fig. 5.1b,c), then the particle surface is rotationally displaced across the fluid-fluid interface, with a portion of surface moving from phase 1 to phase 2, and another portion of the surface going from phase 2 to phase 1, so called *out-of-plane* rotation.

In order to reconstruct the trajectory of a magnetic particle subjected to an external magnetic field, it is necessary to track its *translational* and *rotational* motion. The translational *in-plane* motion of a particle (xy -plane) can be resolved with microscopic techniques. A translational motion may be present due to magnetic field gradients or fluid flow within the sample. For particles larger than the spatial resolution of the microscope, a common approach is to filter the image with a convolution kernel representing a theoretical image or a template image of the particle.⁸⁷ Then, the center is determined from the location of the maximum intensity of the convoluted image. An alternative approach is to use the Hough transform,⁸⁸ an algorithm that looks for a set of pixels belonging to

the same geometrical object (e.g. the circular shape of a particle in a 2D image), which was already introduced in Chapter 3. This approach has the advantage to be robust to fluctuations of pixel intensity and noise in the image data, and to the close proximity of other particles. The translational out-of-plane motion of particles (z -axis) can be determined using holographic imaging, where the z position is determined from the fitting of a diffraction image of the particle using a Mie-scattering model (e.g. see Fig. 2.4a of Chapter 2).⁵¹ In experiments performed at a fluid-fluid interface, the vertical motion of particles is usually limited to a few nm due to the strong interfacial forces (see Chapter 2), so that it is not necessary to track the z displacement in out-of-plane rotation experiments.

The *rotational* motion of a particle can be resolved if optical features are present on its surface. A common strategy is to couple fiduciary markers on the surface of the particles, such as with fluorescent nanoparticles as sketched in Fig. 5.1a,b.^{88,89} In the following, we will describe the theoretical framework as proposed by Irmscher *et al.*⁸⁸ The xy position of nanoparticles below the diffraction limit (≈ 200 nm) can be determined using centroid-tracking algorithms,⁸⁷ or by fitting the nanoparticles intensity profile with a two-dimensional Gaussian, a common approach used in super-resolution imaging techniques such as STORM and PALM.²²⁵ The z position of the nanoparticles can be determined indirectly by assuming a spherical geometry of the particle, so that

$$z = \left[(R+r)^2 - (X-x)^2 - (Y-y)^2 \right]^{\frac{1}{2}} \quad (5.2)$$

where (X, Y) and (x, y) are the center of the magnetic particle with radius R and of the nanoparticle with radius r respectively. Finally, the set of locations found in all the frames are correlated with an algorithm based on spatial and temporal correlation, so that the trajectory of each single nanoparticle is reconstructed.⁸⁷ We can then write the location of the n nanoparticles present at frame i with the matrix

$$\mathbf{x}_i = \begin{pmatrix} x_i^1 & \dots & x_i^n \\ y_i^1 & \dots & y_i^n \\ z_i^1 & \dots & z_i^n \end{pmatrix} \quad (5.3)$$

The nanoparticles on the surface of the particle represent a particle-fixed coordinate system, so that their locations can be used to map the rotation \mathbf{R}_i from frame i to frame $i+1$ as

$$\mathbf{x}_{i+1} = \mathbf{R}_i \mathbf{x}_i \quad (5.4)$$

According to Euler's theorem, the rotation matrix \mathbf{R} can be described by three successive rotations around the three coordinate system axis x , y and z , with angles ψ , θ and φ respectively (see Fig. 5.1c).

In this framework, we consider extrinsic rotations, so that the elementary rotations occur around the axis of the fixed coordinate system xyz , as described in Fig. 5.1c. In this way, the rotation of the particle-fixed coordinate system $x'y'z'$ is described by the matrix

$$\mathbf{R} = \mathbf{R}_\varphi \mathbf{R}_\theta \mathbf{R}_\psi \quad (5.5)$$

Usually the rotation matrix \mathbf{R} cannot be determined by inverting eqn (5.4), as uncertainties in the locations of the nanoparticles are usually present. An alternative approach is to compute the rotation at the i -th frame \mathbf{R}_i by solving the nonlinear least-squares problem

$$E = \|\mathbf{x}_{i+1} - \mathbf{R}_i \mathbf{x}_i\|^2 \quad (5.6)$$

Due to the nonlinearity of the problem, eqn (5.6) might not converge to a global minimum. To tackle this problem, the amplitude motion of the Euler angles could be restrained using the *a priori* knowledge of the actuation sequence used for the experiments.

5.2.4 Experiments

In the previous section, we described a general framework to perform out-of-plane rotation experiments, where fluorescent nanoparticles coupled to the surface of the particle are used to reconstruct the rotation of a magnetic particle under the influence of an external magnetic field.

In order to resolve the 6 degrees of freedom of the motion of a particle, it is necessary to visualize in the same image both the fluorescence particles as well as the outline of the larger magnetic particle. This requires to simultaneously combine fluorescence imaging and bright field imaging. In a conventional upright microscope (e.g. a Leica DM6000 B, the one used in this study), fluorescence imaging is obtained using a filter cube, mounted between the light source and the microscope objective, that allows only the light emitted from the fluorescent nanoparticles to reach the detector. However, most of the light from the excitation source (Leica EL6000) is blocked by the narrow bandpass filter of the filter cube, and the outline of the particle may not be visible. To circumvent this problem, transmitted light field microscopy can be used, but it requires the optical path of the microscope to be clear from any light-blocking object.

Out-of-plane rotation experiments can be performed by modulating the magnetic field between directions normal and parallel with respect to the plane of the interface (see Fig. 5.1a,b). With the electromagnet setup described in Chapter 3, horizontal and vertical magnetic fields can be obtained in principle using only 2 electromagnets (see Fig. 5.2a). This configuration has the advantage that transmitted and reflected light can be used simultaneously, thus allowing to combine in one image both bright field and fluorescent imaging. However, this configuration limits the magnitude of the applicable magnetic fields and introduces relatively strong magnetic field gradients towards the pole tips. With the addition of a bottom magnet (see Fig. 5.2b), higher magnetic fields are applicable with reduced field gradients. However, this configuration limits to the use of only reflected light microscopy as the bottom magnet blocks the optical path. As we will show in the next section, high magnetic fields are required in order to overcome interfacial forces and to observe particle rotation. Therefore, we choose the 3-electromagnet configuration for our experiments (see Fig. 5.2b).

Particles were imaged with a total magnification of 40 X using an air objective. Fluorescent microscopy was used to visualize Protein-G coated magnetic particles labeled with fluorescent nanoparticles (**FM-FL-G**, see section 5.2.2). We used a high density of fluorescent markers in order to enhance the contrast of the large magnetic carrier (Fig.

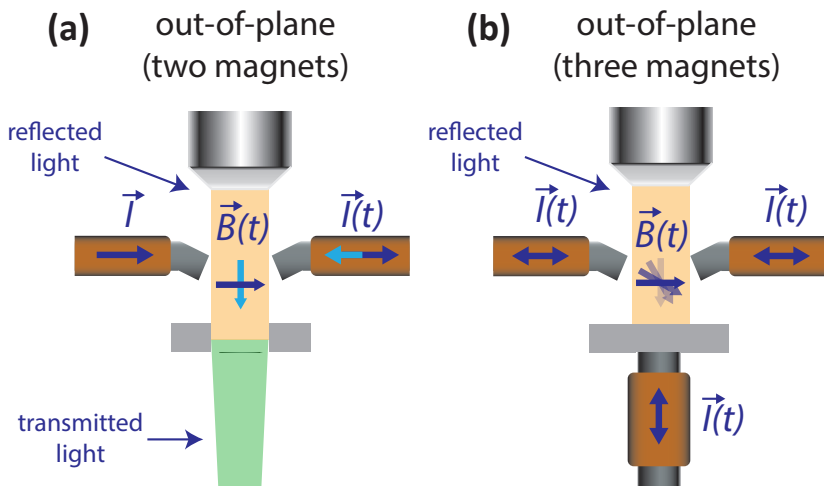


Figure 5.2: Setup for out-of-plane rotation experiments. An out-of-plane rotating magnetic field can be generated using (a) two or (b) three electromagnets.

5.3a), as the imaging system was limited to only one light source (see Fig. 5.2b). Dark field microscopy was used to image particles functionalized with carboxylic acid (**FM-C**), protein G (**FM-G**) and tryptophan (**FM-T**) (Fig. 5.3b), as no fluorescent tags were on the surface of the particle. The scattered light due to structures on or in the particle (see Fig. 5.1d) were sufficient to determine the rotational motion.

We performed out-of-plane rotation experiments utilizing the sequence shown in Fig. 5.3c. The rotation is performed around the y -axis with a sinusoidal modulation. With this actuation protocol, we can describe the particle rotation with the angle φ_P between the particle dipole moment and the position of the particle at equilibrium, which we assume to be aligned with the z -axis (see Fig. 5.1a,b).

5.3 Results

5.3.1 Water-decane interface

We performed out-of-plane rotation experiments at a water-decane interface using particles coated with protein G and labeled with fluorescent nanoparticles (**FM-FL-G**, Fig. 5.3a). Particles were positioned at the interface using a cylindrical permanent magnet, so that the magnetic moment is oriented normal with respect to the plane of the interface (Fig. 5.1a). Particles exposed to an external rotating magnetic field (Fig. 5.3c), did not show out-of-plane rotation. Only an in-plane rotation was observed. A small deviation of the magnetic moment from normality with respect to the plane of the interface would result in an in-plane component of the magnetic moment. This would be enough to apply a torque and rotate the particle in the plane of the interface.

We performed experiments at a lower surface tension of the water-decane interface by

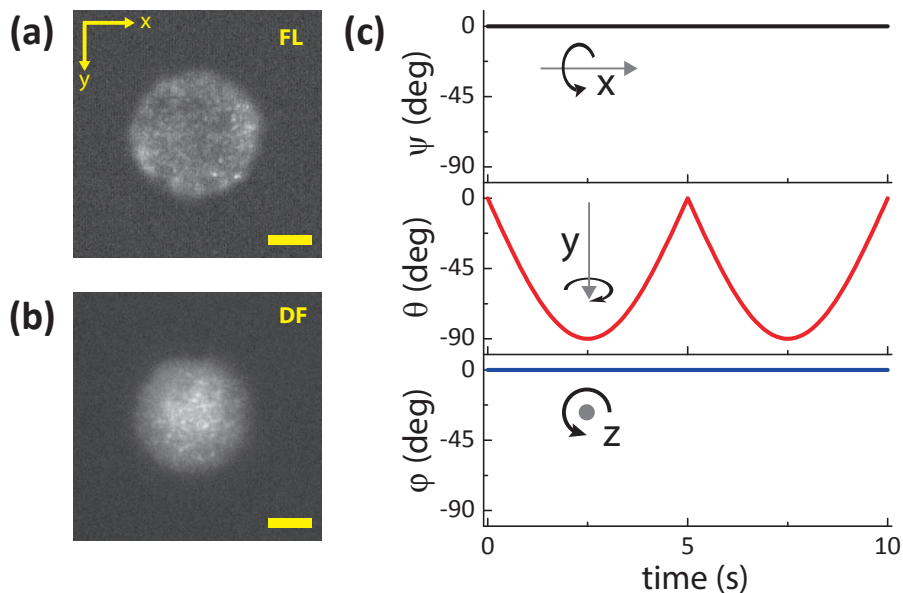


Figure 5.3: Actuation protocol for out-of-plane rotation experiments. **(a)** Fluorescence imaging (FL) of a $33\ \mu\text{m}$ ferromagnetic particle functionalized with protein G and 200 nm fluorescent nanoparticles at a water-decane interface. The bright spots correspond to the fluorescent light from the nanoparticles. **(b)** Dark field (DF) imaging of a $33\ \mu\text{m}$ ferromagnetic particle functionalized with protein G at a PEG-DEX interface. The brighter spots correspond to the scattered light due to structures on or in the particle. Scale bars correspond to $10\ \mu\text{m}$. **(c)** Rotation of an external magnetic field expressed with Euler angles as defined in eqn (5.5).

adding different concentrations of an anionic surfactant (sodium dodecyl sulphate, SDS, Sigma Aldrich) in the aqueous phase. Again, the results showed no out-of-plane rotation motion, suggesting that interfacial forces dominate over magnetic forces.

5.3.2 Aqueous two-phase system

Experiments performed at a water-decane interface showed that an external magnetic torque is not sufficient to induce an out-of-plane rotation of the particle. A water-decane interface has a high energy density ($\approx 10\ \text{k}_B\text{T}/\text{nm}^2$). An interesting alternative is to use aqueous-two-phase system (ATPS) interface, which represents a low-surface tension system.

ATPS interfaces, such as the one obtained by mixing polyethylene glycol (PEG) and dextran (DEX), have been previously used to partition macromolecules such as proteins, nucleic acids and cells organelles in one of the two phases.²²⁶ The driving mechanism of phase separation is determined by the interactions between the monomeric units of the two polymer used, where a small repulsion between the units of different polymers is sufficient for phase separation.²²⁷ If a macromolecule, e.g. a protein, is added to the mixture, it will partition in one of the two phases depending on several factors, such as on

its charge, the ionic composition of the phase system and type and molecular weights of the polymers. Liu *et al.* recently measured the surface tension of an ATPS system using a spinning drop tensiometer.²²⁸ The authors found that the surface tension depends on the mass fraction of the polymer used, with values ranging from 10^{-7} to 10^{-4} N/m, which corresponds to an energy density of $\approx 10^{-3} - 1$ k_BT/nm².

We performed out-of-plane rotation experiments using particles functionalized with protein G, tryptophan and with the as-supplied carboxylic acid surface. Particles were deposited at a PEG-DEX interface (see section 5.2.1) and thereafter exposed to an external rotating magnetic field, with an orientation as described in Fig. 5.3c. Particles were imaged using dark field microscopy (Fig. 5.3b), since no fluorescent nanoparticles were used to label the surface of the particle. The motivation of this particular choice is twofold. From a fundamental standpoint, we wanted to compare the motion of particles with a different surface functionalization. The presence of nanoparticles would have altered the surface properties of the magnetic particle depending on the surface properties and the density of the nanoparticles. From an experimental standpoint, the labeling of the magnetic particles would have required different chemical strategies depending on the desired final surface chemistry, which was out of the scope of the present study. Although no tags were present, it was possible to track the particle rotation by observing the scattered light from the irregularities of the surface of the particles. However, the lack of reference points on the surface of the particle complicated significantly the development of an image processing algorithm for automated tracking of the particle trajectory. Therefore, the fixed locations on the surface of the particle were determined by a manual visual analysis of the recorded images. We determined the position of three fixed points on the surface of the particle at frames i and $i + \delta t$. Then, the tracked points were used to calculate the rotation matrix R using eqn (5.6). The errors associated to the estimate of R were determined from the fitting routine. The trajectory was then computed by summing each incremental step between the measured points. In this way, the error of the estimated rotation propagates through the measurement times (see the increasing error bars in Fig. 5.4). Nonetheless, this method provided a good estimate of the particle rotation trajectories (Fig. 5.4).

The results in Fig. 5.4 show an out-of-plane rotation that is in phase with the external applied magnetic field for all the particles. The maximum amplitude motion of the particles depended on the surface functionalization. The trajectory of the **FM-C** functionalized particle shows a maximum amplitude motion of $\varphi_P \approx 120^\circ$, which exceeded the maximum angular difference used for the experiments of $\Delta\varphi_B = 90^\circ$ (see Fig. 5.3c). This extra rotation can be explained with a magnetic moment of the particle not aligned with the initial direction of the external magnetic field.

5.4 Discussion

In the previous section, we observed that the out-of-plane rotation of a particle under the influence of an external magnetic torque is dependent on the fluid-fluid interface used and on the surface functionalization of the particle. For a water-decane interface we did not observe any out-of-plane motion. For a PEG-DEX interface we observed out-of-plane rotation, with an absolute amplitude motion that depended on the surface functionalization

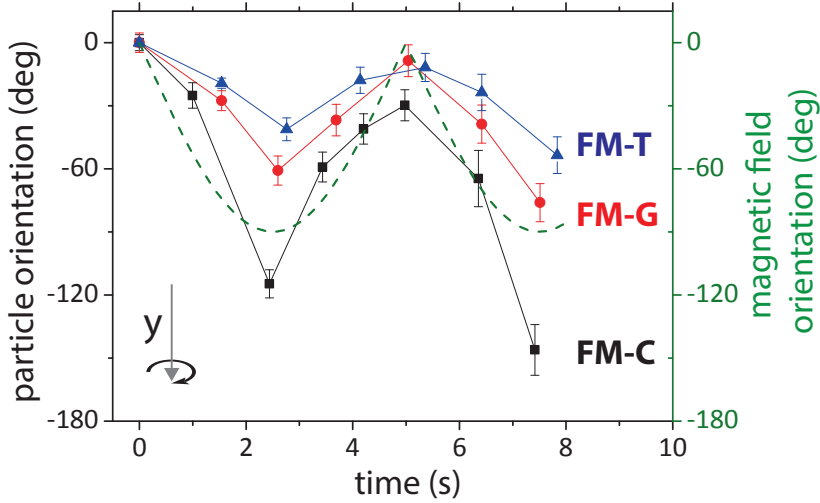


Figure 5.4: Results of out-of-plane rotation experiments for particles at a PEG-DEX interface (see section 5.2.1). Experiments were performed using particles functionalized with carboxylic acid (FC-C), protein G (FC-G) and tryptophan (FC-T). An external magnetic field is applied according the actuation sequence of Fig. 5.3c, so that the rotational axis of the magnetic field is parallel to the plane of the interface and aligned with the y -axis of the image coordinate system (see Fig. 5.1c). We define the particle orientation φ_P and the magnetic field angular orientation φ_B as the angle that the magnetic moment and the magnetic field forms with the vertical axis z respectively.

of the particle. In this section we propose a model to describe particle rotation at a fluid-fluid interface. We then discuss our experimental findings and we propose experiments to further investigate wetting phenomena of single particles at fluid-fluid interfaces.

In Fig. 5.1a,b we sketched how contact angle and interface deformation might play a role in particle out-of-plane rotation under the influence of an external magnetic field. From such experiments, we expect to observe different behaviors (Fig. 5.5a). First, the particle will deform the interface (region I) until the torque is sufficient to overcome the contact-line pinning, which depends on the particle surface properties and fluid surface tension (see Chapter 2). Then, for higher torques we expect a displacement of the contact line at different rotational speed (regions II and III). These experiments represent the analogue of dynamic wetting experiments performed on planar substrates (see section 2.2.5 of Chapter 2), but now performed on colloidal particles trapped at a fluid-fluid interface.

We describe the torque applied to the particle with the equation

$$\vec{\tau}_B + \vec{\tau}_{int} + \vec{\tau}_{hydro} + \vec{\tau}_{cl} = 0 \quad (5.7)$$

where $\vec{\tau}_B$ is the magnetic torque due to the external magnetic field \vec{B} as defined by eqn (5.1). The magnetic torque is opposed by the interfacial torque $\vec{\tau}_{int}$ due to interface deformation, the hydrodynamic torque $\vec{\tau}_{hydro}$, and the torque generated by the contact line friction $\vec{\tau}_{cl}$. In the following we will describe the different components of eqn (5.7).

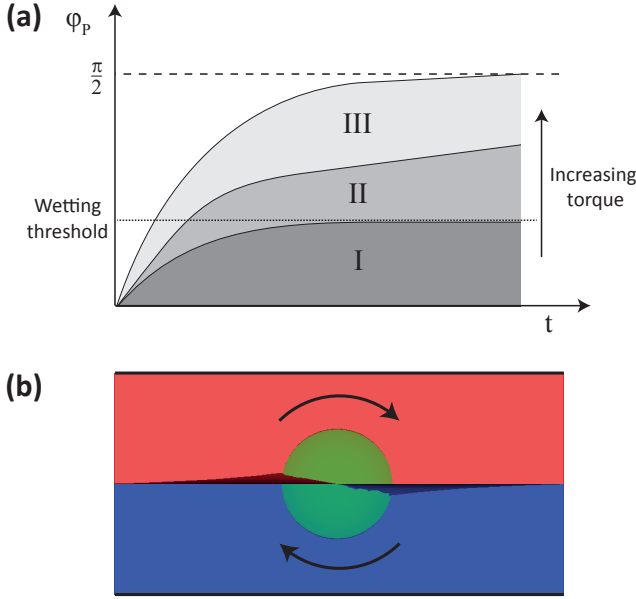


Figure 5.5: **(a)** Sketch of hypothetical outcome of an out-of-plane rotation experiment. Particle orientation as a function of time, for increasing applied torques. Below a wetting threshold, the particle deforms the interface but cannot freely rotate, so the magnetic moment cannot align with the field (region I); above the wetting threshold, dynamic wetting takes place and the three-phase contact line is displaced over the particle (regions II and III). **(b)** Snapshot of a numerical simulation of a particle at a fluid-fluid interface exposed to a constant torque mimicking a rotating magnetic field. The deformation of the interface due to the interactions between particle surface and fluids can clearly be observed. Figures have been adapted and reprinted from Ref.,⁹⁴ copyright (2015), with permission from Elsevier.

5.4.1 Torque required to deform a fluid-fluid interface

Let's assume that the three-phase contact line of a particle trapped to a fluid-fluid interface is pinned to the surface of the particle. If the particle is rotated with an angle φ_p (as sketched in Fig. 5.1b) the interface will deform in a dipolar shape.^{141,142} This shape is determined by the boundary conditions imposed by the Young's equation and can be described by $\nabla^2 h = 0$, which can be solved for the interface height h using a multipolar analysis, as described in section 2.3.4 of Chapter 2.³⁹

The torque required to induce such a deformation is related to the surface free energy ΔE with the equation

$$\Delta E = \int_0^{\varphi_p} \tau_{im} d\varphi \quad (5.8)$$

The modeling of the shape of the interface and of the position of the contact angle for an arbitrary deformation is rather complex and there is no exact analytical expression.

Recently Xie *et al.* derived an analytical solution for the free energy associated to the dipolar deformation of a fluid-fluid interface around a Janus particle, as a function of

particle orientation.¹⁴² A symmetric Janus particle is characterized by a hydrophilic and a hydrophobic hemisphere. When each of the hemispheres is immersed in their favourite fluid phase (e.g. water and oil), the particle is strongly bound to a flat interface. Due to this high binding affinity, the contact line is strongly pinned along the line joining the two hemispheres, so that when the particle is rotated the interface will deform without the slip motion of the three-phase contact line.

The particles used in this study have a homogeneous surface functionalization. However, the contact line may be pinned to surface heterogeneities of the particle (e.g. chemical or surface roughness as shown in Fig. 5.1d). Therefore, in order to estimate the torque required to deform the interface, we use the result from Xie *et al.* in the limit of small tilt angles ($\varphi_P < 30^\circ$) of the particle:

$$\tau_{int} \propto \frac{d(\Delta E)}{d\varphi_P} = \pi\gamma R^2\alpha \quad (5.9)$$

where α is the angle between the plane of the interface and the maximal interface height at the contact line (see Fig. 5.1b). Here, α is expected to vary between 0° – no interface deformation – to a maximum deformation $\alpha = |\theta_D - \theta_{eq}|$ – the moment the contact line starts to move on the surface of the particle. Therefore, α depends on the history of the particle motion. Interestingly, eqn (5.9) shows that the dipolar deformations of the interface can be described as a torsional spring, with a torsion coefficient that depends on the product of the square of the radius R and the surface tension γ . This result was obtained in the limit of small interface deformations and for a system in thermodynamic equilibrium.

In Fig. 5.6 we show calculations of the torque required to deform a fluid-fluid interface as a function of surface tension and different particle radii using eqn (5.9). The permanent magnetic moment of the ferromagnetic particle used in this study (CFM-300) is not known. As a lower limit, we use the value of the magnetic moment of smaller ferromagnetic particles (CFM-040, Spherotech) that are produced in the same way as the larger particles. As an upper limit, if we assume that the magnetic moment scales linearly with the amount of chromium dioxide on the surface of the particle, we estimate a maximum torque that is 2 orders of magnitude larger than the CFM-040, $\tau_{CFM-300} \approx 10^{-13}$ Nm/rad. This estimation suggests that out-of-plane rotation experiments could be in principle performed using an interface with a maximum surface tension of about 1 mN/m. These results are in agreement with the lack of rotation observed for experiments of particles at a water-decane interface, where the surface tension is ≈ 50 mN/m and interfacial forces dominates over magnetic forces. Moreover, these calculations show that it is possible to deform the interface for particles at an ATPS interface, where the surface tension is orders of magnitude lower as compared to a water-decane interface.²²⁸

5.4.2 Dissipative contributions to the rotation of a particle at a fluid-fluid interface

In eqn (5.7) there are 2 terms associated with dissipative effects that oppose to the rotation of the particle: the hydrodynamic torque $\vec{\tau}_{hydro}$ and the torque associated to the contact line friction $\vec{\tau}_{cl}$. While the latter contribution is present only when the particle starts to

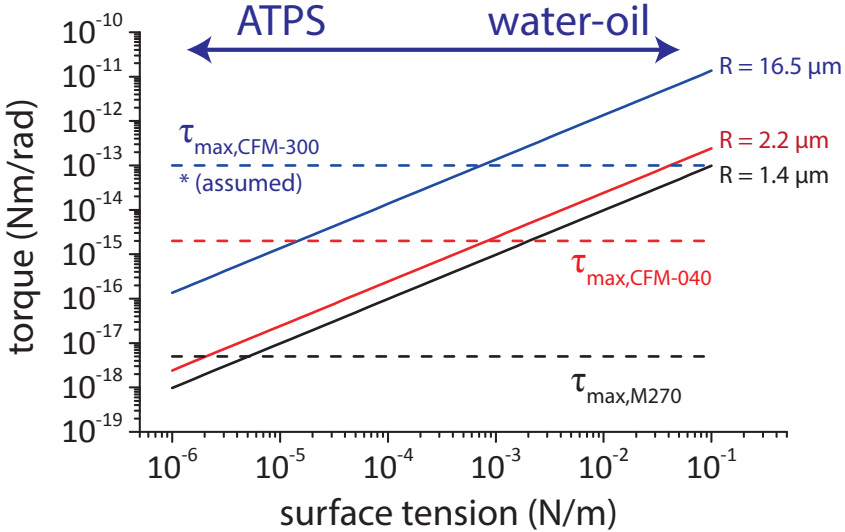


Figure 5.6: Torque required to deform a fluid-fluid interface as a function of surface tension. Calculations were performed using eqn (5.9).¹⁴² We show calculations for particles relevant for this thesis, namely M270 ($R = 1.4 \mu\text{m}$, $m \sim 2 \cdot 10^{-16} \text{ Am}^2$, van Reenen *et al.*⁸⁹), CFM-040 (ferromagnetic, $R = 2.2 \mu\text{m}$, $m \sim 2.2 \cdot 10^{-13} \text{ Am}^2$, Irmischer *et al.*⁸⁸) and CFM-300 (ferromagnetic, $R = 16.5 \mu\text{m}$, assumed $m \approx 10^{-11} \text{ Am}^2$). The dashed lines are the maximum torque that can be applied to M270 particles (black line), to $4.4 \mu\text{m}$ ferromagnetic particles (red line), and assumed for $33 \mu\text{m}$ ferromagnetic particles (blue line) for a magnetic field with magnitude 36 mT.

rotate, the former contribution is always present. For a spherical particle rotating in a fluid with shear viscosity η , the hydrodynamic torque is related to the Stokes drag with the equation

$$\vec{\tau}_{hydro} = 8\pi C_{drag} \eta R^3 \frac{d\vec{\varphi}}{dt} \quad (5.10)$$

where $C_{drag} > 1$ for a particle in the vicinity of a solid substrate.¹³⁶ For a particle rotating at a fluid-fluid interface the rotational drag coefficient is not known and depends on the non-trivial flow field around the particle, which might be further complicated by an asymmetric interface dipolar deformation. Moreover, if one of the two phases or both behaves as a viscoelastic fluid, eqn (5.10) is not valid anymore and the drag coefficient would depend on the frequency or on the history of deformation.

When the applied torque is large enough to overcome the contact-line pinning energy, the particle will start to rotate and contact line friction forces will oppose the particle rotation. According to the molecular kinetic theory presented in section 2.2.7 of Chapter 2, the motion of the contact-line can be described by a stochastic process that depends on the energy landscape provided by the atoms of the substrate. This process can be approximated by a friction force that depends linearly on the contact-line velocity (see eqn (2.10) of Chapter 2). According to the molecular kinetic theory, we can approximate

the torque due to contact line friction as

$$\tau_{cl} = f_{cl} R \frac{d\varphi}{dt} \cdot f(r, \theta_D) = K_{cl} \cdot \frac{d\varphi}{dt} \approx \gamma (\cos \theta_{eq} - \cos \theta_D) \cdot l \cdot R \cdot f(r, \theta_D) \quad (5.11)$$

where $Rd\varphi/dt$ is the tangential velocity, f_{cl} is a friction coefficient (with units Ns/m), l is the contact line perimeter and $f(r, \theta_D)$ is an adimensional function that is expected to be dependent on the radial dipolar deformation of the meniscus around the particle.

Under these assumptions, the dissipative effects of a particle rotating at a fluid-fluid interface could be described by a linear dependence on the rotational velocity $d\varphi/dt$ of the particle, with a coefficient $K_{cl} = f_{cl} \cdot l \cdot R \cdot f(r, \theta_D)$. In Fig. 5.7 we show calculations of the particle angular orientation under the influence of an oscillating magnetic field using eqn (5.1), eqn (5.10) and eqn (5.11). These calculations show that an increasing value of

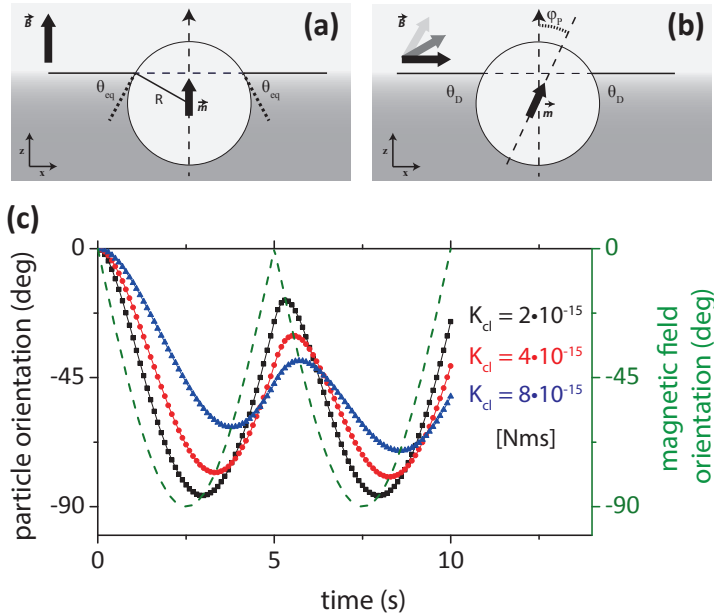


Figure 5.7: Dissipative contributions to the out-of-plane rotation of a particle at a fluid-fluid interface. **(a)** A magnetic particle is at rest at the interface, with the magnetic moment \vec{m} aligned with the external magnetic field \vec{B} . **(b)** The particle rotates under the influence of an external magnetic torque (eqn (5.1)). The rotation of the particle is opposed by friction forces as described by eqn (5.10) and eqn (5.11). Interfacial deformations are neglected, so that $\theta_D = \theta_{eq}$. **(c)** Particle orientation φ_P as a function of time for different values of K_{cl} (Nms). Calculations were performed by considering $B = 20$ mT, $m = 2.2 \cdot 10^{-13}$ Am² and $R = 16.5$ μ m.

the effective friction coefficient (either hydrodynamic drag or contact-line friction) results in an increase of the phase lag between the orientation of the applied magnetic field φ_B and the orientation of the particle φ_P . Moreover, also the amplitude motion is reduced, as the particle cannot follow the rotation of the oscillating magnetic field.

5.4.3 Interpretation and discussion

In section 5.3 we showed that when a particle at a water-decane interface is interrogated with an external magnetic torque, no out-of-plane rotation was observed. According to the model described by eqn (5.9), the applied external torque is not sufficient to overcome interfacial forces (Fig. 5.6). For particles at a PEG-DEX interface, we observed out-of-plane rotation. Here, the low surface tension of the interface reduces greatly the magnetic torque required to overcome interfacial forces (Fig. 5.6).

Several experimental issues limited the analysis of the out-of-plane rotation motion for experiments performed at a water-decane interface. First, the presence of a relatively large translational motion of the particles limited the measurement time as the particles diffused away from the field-of-view. Due to the configuration of the magnetic setup (Fig. 5.2), magnetic field gradients are present along the plane of the interface, with an intensity that increases closer to the pole tips of the electromagnets. The high magnetic content of the ferromagnetic particles used in this study, combined with a low interfacial viscosity of a water-decane interface,²⁰⁰ would be enough to generate speeds up to a few $\mu\text{m/s}$ in the experiment. Moreover, a translation motion might occur for slightly deformed interfaces due to gravity, or if convection is present within the fluid cell. Secondly, this translational motion limited also the maximum magnification applicable, as higher magnifications would further limit the field-of-view. This in turn translates in a poorer resolution of the magnetic particles. The addition of surfactant had the side effect to strongly reduce the adsorption of particles at interface as the result of a steric barrier for adsorption.

Results of experiments performed at a PEG-DEX interface (Fig. 5.4) show that all the motion trajectories are in phase with the applied magnetic field, with a maximum amplitude motion that depends on the surface properties of the particle. According to the model proposed in the previous section, a description of the motion based only on dissipative effects (see eqn (5.10) and eqn (5.11)) predicts that an increase of the overall friction force would decrease the maximum amplitude motion of the particle, but would also introduce a significant phase lag between the direction of the applied magnetic field φ_B and the orientation of the particle φ_P . The data of Fig. 5.4 show that within the resolution of the experiments there is no significant phase lag between the trajectories and the orientation of the magnetic field. This suggests that other contributions to the out-of-plane rotation of particles might be present, such as an elastic deformation of the interface as described by eqn (5.9).

We can interpret qualitatively the difference in the maximum amplitude motion between different coated particles. The ATPS interface has been used to partition macromolecules, e.g. proteins, where the partition coefficient depends on the relative affinity of the macromolecule with one of the two phases. In our experiments, a different surface functionalization might translate in a different contact angle. This in turn would translate in a different contact line perimeter, hence a different contact line friction (eqn (5.11)). Moreover, the magnitude of the dynamic contact angle is expected to depend on the particle surface properties, thereby changing the contribution of the elastic deformation of the interface (eqn (5.9)).

In order to be able to fully capture the dynamics of particle rotation, further research is required. In particular, it is necessary to understand how the rotational frequency of the particle, the magnitude of the external torque, the history of the interface deformation and the motion of the contact-line are related to each other in a time-dependent fashion. In the following we propose experimental and numerical approaches that might help to tackle some of these issues.

From an experimental perspective there are several avenues that could be undertaken in order to get a deeper insight in the rotation dynamics of particles at fluid-fluid interface. For example, (i) an external torque could be applied to induce small rotations of the particle. After removing the external field, the relaxation to the equilibrium position could be measured, thus revealing the elastic response of the interface. For a particle with radius $R = 16.5 \mu\text{m}$, an angular displacement $\Delta\varphi = 1^\circ$ would correspond to a displacement of a fixed point on the surface of the particle of about $0.3 \mu\text{m}$ in the xy -plane of the image of the particle, which correspond to a resolution that can be easily resolved with conventional microscopy. (ii) The particle could be further rotate so that the contact-line would start to slip on the surface of the particle. This experiment, combined with the results obtained in (i) could be used to extract information about the contact-line pinning. (iii) The rotation of the particle at different frequencies might help in understanding the underlying physical mechanism of wetting, thus testing the validity of the proposed eqn (5.11). (iv) Finally, wetting could be studied as a function of full revolutions of the particles, so that hysteresis effects might be revealed.

In order to be able to perform the proposed experiments, some experimental features need to be improved. The success of these experiments relies on the ability of tracking accurately the 3D rotation of particles. The use of external fluorescent tags might limit the flexibility of surface functionalization, both chemical and topological. An envisaged strategy would be to produce particles with embedded optical anisotropies in the core of the particle, so that it would not affect the outer surface properties. Moreover, the availability of particles with a tailored surface roughness would help to disentangle the contribution of topological and chemical surface features to both the contact line friction at hydrodynamic contribution to the rotation of the particle. Finally, the force needed to drive particles out of equilibrium depends a.o. on the presence of contact line pinning and surface tension. A water-decane interface has a surface tension of roughly 50 mN/m , or $10 k_B T/\text{nm}^2$, which represents a large energy density. Therefore, to make all modes of particle motion accessible in a magnetic tweezers experiment, it is preferred to have high magnetic fields and particles with high magnetic moments available, ideally with a wide variety of particle surface properties such as roughness and surface functionalization. With this available, contact-line pinning energies and contact angle hysteresis can be quantified as a function of microscale surface features, for example, roughness and chemical properties, and different combinations of fluids. The quantification of the deformation of the interface for a known torque can be used to determine the surface tension, or to study capillary-dipole interactions. Moreover, wetting dynamics can be studied on a microscale level for different Capillary numbers, and a large number of parameters.

These experiments can be accompanied by computer simulations. For example, Razavi et al.¹⁶⁷ use molecular dynamics simulations to investigate the effect of localized features

on the rotational dynamics of nanoparticles straddling a fluid-fluid interface, based on Kramers' model. They show the presence of long-lived metastable states where the particle remains locked in angular orientations. Alternatively, simulations based on combined lattice Boltzmann and molecular dynamics methods can be applied.¹⁴² Fig. 5.5b shows an example snapshot from such a simulation: a magnetic particle is trapped at a fluid-fluid interface and a constant torque is applied. Due to the resulting rotation of the particle and the interaction of the particle surface with the fluids, the interface deforms and the dynamic contact angle on the particle surface can be measured. The advantage of this kind of simulations is that parameters such as surface tension, particle surface morphology and time dependence of the magnetic field can be varied systematically and independently.

Another interesting approach is to use anisotropic particles. Although many experimental studies have been done with spherical particles, computer simulation on particles with different shapes (e.g. ellipsoids, cylinders, dumbbells, etc.), or surface properties (e.g. Janus particles), or a combination of shape and surface properties (e.g. Janus ellipsoids), reveal unique properties that may be exploited for particle self-assembly at interfaces or as a platform for the design of novel colloid-based materials.

5.5 Conclusions

The equilibrium shape of a fluid interface and the displacement of a fluid over a surface are the result of fluid molecules interacting with another phase. The specific properties of the involved fluids and surface result in macroscopic effects which are typically characterized by experimentally accessible parameters such as viscosity, surface tension, wetting speed and dynamic contact angle. However, these parameters give only indirect information about the underlying microscopic and molecular-scale processes, and this indirectness complicates the development and validation of model descriptions. Studying the wetting of single colloidal particles trapped at fluid-fluid interfaces may offer novel avenues, where small scale effects are dominant and quantitatively observable.

In this Chapter we have presented a novel methodology to study dynamic wetting on single colloidal particles at fluid-fluid interfaces. Particles were interrogated with an oscillating out-of-plane magnetic field. Experimental results showed that the particle angular orientation depended on the surface tension of the interface and on the particle surface properties. We discussed the results in relation to a model that includes elastic contributions due to interface deformation and dissipative effects due to contact line friction.

The novel experimental approach reported in this Chapter opens new avenues to study dynamic wetting at the microscale. With single particle based methodologies, pinning energies and wetting hysteresis may be studied as a function of morphological and chemical surface features for particles at different fluid interfaces, in order to test different models under a wide range of parameters. The quantification of interface deformation for a known torque can be used to quantify surface tension, or to study capillary-dipole interactions. Moreover, wetting dynamics can be studied on a microscale level for different Capillary numbers and fluids. Computer simulations based on combined lattice Boltzmann and molecular dynamics methods¹⁴² might be used to complement experiments since they allow to model the impact of varying molecular interactions or microscopic

surface properties such as roughness, elasticity, charges, or hydrophobic/hydrophilic interactions individually.

These experimental approaches in combination with numerical tools should help scientists and engineers to tackle a wide range of challenges that require to be predictive and to have exquisite control on the wetting behavior at different spatial and temporal scales. We expect that the resulting understanding and materials control should lead to novel bottom-up approaches in the field of colloidal self-assembly and novel particle-based concepts for miniaturized (bio)analytical tools.



6

Conclusions and Outlook

6.1 Introduction

The aim of the work presented in this thesis was to develop new methodologies using magnetic particles in order to capture different wetting phenomena occurring at fluid-fluid interfaces. In particular, we focused on the study of microrheology, capillary interactions between particles and dynamic wetting of single particles at fluid-fluid interfaces. In this concluding Chapter we synthesize the main findings regarding each topic and propose future prospects.

First we review the reasoning for using magnetic particles at fluid-fluid interfaces. Magnetic particles are nowadays available in a wide range of sizes, material and optical properties, and offer many bio-functionalization options, thus making them suited to study a wide range of material systems and applications.¹² Moreover, magnetic tweezers have the advantage of low interference, because organic materials are fully permeable and insensitive to magnetic fields. In this thesis, we developed methodologies based on the use of two classes of magnetic colloids at fluid-fluid interfaces, namely superparamagnetic and ferromagnetic particles. We summarize some of the key features of using magnetic particles that helped us in developing the experimental work described in this thesis.

(i) *Actuation properties.* In the presence of an external magnetic field, superparamagnetic particles acquire an induced magnetic dipole moment along the direction of the field. When particles are in close proximity of each other, the resulting dipole-dipole force can be used to displace particles over several micrometers in a few seconds and to apply well-defined forces from a few pN to several nN, depending on the magnetic properties of the particles and the source of the magnetic fields.^{81,189} By alternating the orientation of the magnetic field it is possible to induce magnetic separation and attraction, so called Intra-Pair Magnetophoresis (IPM).¹⁸⁹ The IPM approach was used in Chapter 3 to quantify the drag coefficient of particles at a water-oil interface in the presence of polymer adsorbing to the interface. In the absence of an external magnetic field, superparamagnetic particles have no net magnetization. This allowed us in Chapter 4 to measure repeated motion

trajectories of inter-particle capillary attraction. Ferromagnetic particles are characterized by a permanent magnetic moment that can be used to exert a magnetic torque. This approach was used in Chapter 5 to study dynamic wetting of single particles at fluid-fluid interfaces.

(ii) *Surface properties.* The surface of magnetic particles can be conveniently modified to study a wide range of material systems. In Chapter 3 we studied a material system where polymers with positive charges interacted electrostatically with the negative surface of magnetic particles at a water-oil interface. This in turn changed the affinity of the particle to the oil phase and for a sufficiently high concentration of polymer the particles transited into the oil-phase. The same principle was used in Chapter 4 to modulate the particle contact angle, which then resulted in a change of capillary attractive forces. In Chapter 5 we studied dynamic wetting as a function of particle surface functionalization.

(iii) *Optical properties.* Micrometer sized particles are directly accessible using video-microscopy techniques,^{87,88} which are used to visualize and reconstruct the translational motion trajectories of particles (see Chapters 3 and 4). The rotational motion of particles can be determined by conveniently coupling optical features on the surface of the particles, such as fluorescent nanoparticles^{88,89} (see Chapter 5).

6.2 Phenomena investigated using magnetic particles at fluid-fluid interfaces

6.2.1 Interfacial micro-rheometry

Amphiphilic molecules, such as surfactants, proteins and certain polymers, have the tendency to populate fluid-fluid interfaces due to their strong affinity to both phases. Upon adsorption, the time-dependent evolution of the microstructure of the adsorbed species is responsible for changes of the mechanical properties of the interface.^{6,7,25,47,48} Studies of these processes require rheometry techniques that are suited for small amounts of materials, small length scales, short and long timescales, and that are easy to use.

In Chapter 3 we used IPM to quantify interfacial drag coefficient of particles in the presence of an amino-modified silicon polymer adsorbing to a water-oil interface. With this method we were able to simultaneously record many particles in parallel over short (\sim s) and long (\sim hours) timescales, and to measure drag coefficients spanning more than three orders of magnitude (10^{-7} to 10^{-4} Ns/m). The results showed that the particle drag strongly depended on polymer concentration, on time, and on the ionic strength of the aqueous phase. Moreover, for a low ionic strength of the aqueous phase the rate at which the drag increased depended on the initial polymer concentration, suggesting a history-dependent ageing of the interface determined by the dynamics and interactions of the adsorbed polymer at early stages.

The use of active microrheology allows one to measure higher interfacial viscosities as compared to passive methods and has the potential to study the nonlinear rheological response of the interface. Examples from literature include the use of rotating magnetic micro-needles,⁶² oscillating probes driven by magnetic fields⁶⁴ or optical tweezers.¹⁸⁶ The experiments performed in Chapter 3 showed that the response of the interface to the

motion of magnetic particles was essentially Newtonian. Interestingly, for long polymer adsorption times and small particle separations a very small deviation appeared, pointing to a nonlinear response of the interface. In these experiments large displacement amplitudes were used, which might perturb an elastic structure forming at the interface. Alternatively, the IPM technique may be applied with small amplitude oscillatory motions and frequencies of tens of Hz, thus revealing viscoelasticity. Another interesting feature of the IPM method is that particles can be separated and attracted, thus allowing to study potential differences between interface elongation and compression.

Care must be taken when interpreting microrheology data obtained from the forced motion of a probe, as different dynamic modes, e.g. shear and dilatation, could be mixed in one single measurement.⁶⁷ Here, the interpretation of interfacial rheology depends on the hydrodynamic model used.^{26,68,69} This could be further investigated by comparing experiments of particle translation using IPM and particle in-plane rotation, using the same setup described in this thesis.

Another known issue of particle-based microrheology is to obtain reliable data from measurements performed on systems with a low Boussinesq number. The drag of a particle at fluid-fluid interfaces depends on the viscosities of the two fluids and on the particle contact angle. At low Boussinesq number, the motion of the particle is dominated by the sub-phase viscosity and changes of the particle drag coefficient may be caused by variations of the particle contact angle, thus providing only apparent rheological data.^{26,36,67} To this purpose, variations of the particle contact angle could be determined by measuring the vertical displacement of particles using holographic imaging,⁵¹ or by indirectly monitoring changes of inter-particle capillary interactions, as proposed in Chapter 4. Another approach would be to perform IPM experiments using magnetic particles with different sizes, since an intrinsic material property like the interfacial viscosity must not depend on particle size.

6.2.2 Inter-particle capillary interactions

The understanding and the control of inter-particle interactions at fluid-fluid interfaces is of theoretical and practical interest. Electrostatic and capillary interactions are the dominant forces between particles at fluid-fluid interfaces. Electrostatic interactions originate from the asymmetric distribution of charges on the particle surface across the interface; capillary interactions are determined by interface deformations, where inter-particle forces are driven by surface minimization.⁴⁰ The adsorption of particles to fluid interfaces may result in an irregular meniscus due to the pinning of the three-phase contact line to surface heterogeneities, such as chemical or surface roughness.⁷⁰ This results in long-ranged capillary forces associated to a quadrupolar deformation of the interface.³⁹

In Chapter 4 we investigated inter-particle capillary forces at a water-oil interface in the presence of strong polymer-induced ageing. To this aim we expanded the use of IPM to record multiple motion trajectories of particle attraction. Pairs of magnetic particles were first separated by a few particle diameters by shortly applying an out-of-plane magnetic field and then, after removing the field, the field-free motion trajectories were recorded. This approach provided us with an independent quantification and a direct correlation of the interfacial drag coefficient and the non-viscous inter-particle forces.

The results showed that capillary forces depended on the initial polymer concentration. Thereafter the polymer still contributed to changes of interfacial viscosity without further changes of the attractive capillary forces. This suggests that the polymer dynamics at the early stages of interfacial ageing is responsible for the equilibration of capillary forces. The measured force is consistent with a model description based on quadrupolar deformations of the fluid-fluid interface caused by particle surface roughness, and is modulated by changes of the particle contact angle.

Current methods to study inter-particle capillary forces include particle tracking based on video-microscopy^{73,74,78,79} and optical tweezers experiments.^{40,80,82} Our method represents an interesting alternative where both conservative and dissipative effects can be quantified and the motion of many particles can be recorded in parallel. For further studies it would be interesting to study inter-particle capillary force for particles with a tailored surface roughness. The far-field interaction, i.e. for inter-particle separations greater than several particle radii, is well described as a superposition of leading-order capillary multipoles, where the interaction is almost universally determined by the quadrupolar term (see Chapter 4).^{39,70,74} The near-field interaction is dominated by the shape details of the undulated meniscus and the superposition approximation fails. The IPM method could be used to study capillary interactions at different inter-particle separations by modulating the repulsive magnetic force. Moreover, the coupling of optical features on the surface of the particle would allow one to investigate the rotational dynamics at different length scales. This knowledge will help scientists to understand the dynamics of colloidal self-assembly and to predict new structures.

6.2.3 Dynamic wetting of single particles

The interactions between fluids and substrates are mostly described by macroscopic observables which are easily accessible, such as viscosity, surface tension and dynamic contact angle. However, these parameters provide only an indirect description of the underlying microscopic and molecular-scale processes. Despite much research, a consensus on the underlying physical mechanism of wetting is still a matter of debate.⁵⁰ An attractive alternative is to use micrometer sized colloidal particles trapped at fluid-fluid interfaces, where small scale effects are dominant and quantitatively observable.

In Chapter 5 we proposed an alternative approach to study dynamic wetting of single particles at fluid-fluid interfaces, where ferromagnetic particles were interrogated with an oscillating out-of-plane magnetic field. Results showed wetting patterns that depended on the particle surface properties and surface tension of the interface. We interpreted these results with a model that includes interfacial elastic deformations and contact line friction. Previous experiments of dynamic wetting on single particles were based on optical tweezers⁵¹ and colloidal probe AFM.⁵² Both methods allow to resolve the vertical motion of particles adsorbing to fluid interfaces with a spatial and temporal resolution of a few nanometers and μs , but are limited to the translational motion of the probes. With the addition of 3 rotational degrees of freedom, new avenues could be taken to study contact line pinning, contact angle hysteresis, dipolar-capillary deformations, wetting hysteresis effects, and the hydrodynamics of rotating particles at fluid-fluid interfaces.

To make these experiments accessible, an improvement of the tracking sensitivity of

the rotational motion of the particles is required. A possible strategy is to embed optical features in the core of the particles and to design a setup that allows to combine different imaging modes, such as transmitted and fluorescent imaging. The use of high magnetic fields and particles with high magnetic moments are preferred, so that high surface tension interfaces could be studied. Particles with well defined surface properties, such as roughness and surface functionalization, would allow to explore wetting phenomena in a wide range of material systems. These experimental improvements accompanied by reliable numerical tools to study dynamic wetting effects on colloidal particles at micro- and molecular scale, will help scientists and engineers form diverse disciplines to tackle a wide range of problems and develop new applications.

6.3 Future work

The research performed in this thesis has shown the potential of using magnetic particles to address questions regarding wetting phenomena at fluid-fluid interfaces. Fluid-fluid interfaces are an intrinsically complex problem, even for mono-component phases. This complexity is further increased by the adsorption of macromolecules to the interface, which is accompanied by structural changes on very different spatial and temporal scales. We foresee that the availability of new experimental and numerical tools will allow scientists from different areas to study gradually more complex material systems, which will eventually lead to a deeper theoretical understanding of the relevant molecular processes.

Mastering this complexity will have an important impact for several technologies. In the upcoming generations of lab-on-a-chip systems, complex fluids (e.g. blood, saliva, urine) come in contact with solid surfaces and secondary phases. The miniaturization of such devices implicates very large surface-to-volume ratios, where dynamic wetting effects are relevant, particularly in systems where small droplets or colloidal particles are used for sample manipulation, target extraction, purification, detection, etc.¹² The control of the interactions of particles at fluid-fluid interfaces will open novel bottom-up approaches for the creation of new functional materials with unique properties.³² As an example, magnetic nanoparticles could be used to create micro-capsules for targeted drug delivery, where an external magnetic field is used to trigger the release of the therapeutic cargo.¹⁹⁰ In next generations of in-vivo diagnostics, the use of nanoparticles will play an important role. Particles can be conveniently functionalized to target specific biological components, e.g. proteins, viruses and cancer cells, for imaging and therapy. The success of these applications relies on the interactions of the nanoparticles with their biological environment that contains numerous complex soft-matter interfaces.

Bibliography

- [1] Y. T. Cheng, D. E. Rodak, C. A. Wong, and C. A. Hayden. Effects of micro- and nano-structures on the self-cleaning behaviour of lotus leaves. *Nanotechnology*, 17(5):1359–1362, 2006.
- [2] S. Shin, J. Seo, H. Han, S. Kang, H. Kim, and T. Lee. Bio-Inspired Extreme Wetting Surfaces for Biomedical Applications. *Materials*, 9(2):116, 2016.
- [3] D. Bonn, J. Eggers, J. Indekeu, J. Meunier, and E. Rolley. Wetting and spreading. *Reviews of Modern Physics*, 81(2):739–805, 2009.
- [4] H.-J. Butt, K. Graf, and M. Kappl. *Physics and Chemistry of Interfaces*. Wiley-VCH Verlag GmbH & Co. KGaA, Weinheim, FRG. ISBN 3527404139, 2003.
- [5] M. Ma and R. M. Hill. Superhydrophobic surfaces. *Current Opinion in Colloid & Interface Science*, 11(4):193–202, 2006.
- [6] B. S. Murray and E. Dickinson. Interfacial Rheology and the Dynamic Properties of Adsorbed Films of Food Proteins and Surfactants. *Food Science and Technology International, Tokyo*, 2(3):131–145, 1996.
- [7] M. A. Bos and T. van Vliet. Interfacial rheological properties of adsorbed protein layers and surfactants: a review. *Advances in Colloid and Interface Science*, 91(3):437–471, 2001.
- [8] I. Tavernier, W. Wijaya, P. Van der Meeren, K. Dewettinck, and A. R. Patel. Food-grade particles for emulsion stabilization. *Trends in Food Science & Technology*, 50:159–174, 2016.
- [9] I. Kralova and J. Sjöblom. Surfactants Used in Food Industry: A Review. *Journal of Dispersion Science and Technology*, 30(9):1363–1383, 2009.
- [10] A. Ammala. Biodegradable polymers as encapsulation materials for cosmetics and personal care markets. *International Journal of Cosmetic Science*, 35(2):113–124, 2013.
- [11] L. Isa, K. Kumar, M. Müller, J. Grolig, M. Textor, and E. Reimhult. Particle Lithography from Colloidal Self-Assembly at Liquid-Liquid Interfaces. *ACS Nano*, 4(10):5665–5670, 2010.
- [12] A. van Reenen, A. M. de Jong, J. M. J. den Toonder, and M. W. J. Prins. Integrated lab-on-chip biosensing systems based on magnetic particle actuation - a comprehensive review. *Lab on a Chip*, 14(12):1966, 2014.
- [13] B. Su, Y. Tian, and L. Jiang. Bioinspired Interfaces with Superwettability: From Materials to Chemistry. *Journal of the American Chemical Society*, 138(6):1727–1748, 2016.

- [14] V. Dutschk and M. Abraham. The contact angle as an analytical tool. In P. Kralchevsky, R. Miller, and F. Ravera, editors, *Colloid and Interface Chemistry for Nanotechnology*, chapter 12, 2013.
- [15] P.-G. de Gennes, F. Brochard-Wyart, and D. Quere. *Capillarity and Wetting Phenomena: Drops, Bubbles, Pearls, Waves*. ISBN 0387005927, 2004.
- [16] T. Young. An Essay on the Cohesion of Fluids. *Philosophical Transactions of the Royal Society of London*, 95(1805):65–87, 1805.
- [17] J. Drelich, E. Chibowski, D. D. Meng, and K. Terpilowski. Hydrophilic and superhydrophilic surfaces and materials. *Soft Matter*, 7(21):9804, 2011.
- [18] P. A. Kralchevsky and K. Nagayama. *Particles at Fluid Interfaces and Membranes*. Elsevier, first edit edition. ISBN 978-0-444-50234-6, 2001.
- [19] D. L. Hu and J. W. M. Bush. Meniscus-climbing insects. *Nature*, 437(7059):733–736, 2005.
- [20] M. Andersson Trojer, L. Nordstierna, J. Bergeek, H. Blanck, K. Holmberg, and M. Nydén. Use of microcapsules as controlled release devices for coatings. *Advances in Colloid and Interface Science*, 222:18–43, 2015.
- [21] S. Rebello, A. K. Asok, S. Mundayoor, and M. S. Jisha. Surfactants: toxicity, remediation and green surfactants. *Environmental Chemistry Letters*, 12(2):275–287, 2014.
- [22] M. Rayner, D. Marku, M. Eriksson, M. Sjöo, P. Dejmeek, and M. Wahlgren. Biomass-based particles for the formulation of Pickering type emulsions in food and topical applications. *Colloids and Surfaces A: Physicochemical and Engineering Aspects*, 458(1):48–62, 2014.
- [23] S. Je Lee and M. Rosenberg. Whey Protein-based Microcapsules Prepared by Double Emulsification and Heat Gelation. *LWT - Food Science and Technology*, 33(2):80–88, 2000.
- [24] B. P. Binks and T. S. Horozov. *Colloidal particles at liquid interfaces*. Cambridge University Press, New York. ISBN 9780521071314, 2008.
- [25] A. J. Mendoza, E. Guzmán, F. Martínez-Pedrero, H. Ritacco, R. G. Rubio, F. Ortega, V. M. Starov, and R. Miller. Particle laden fluid interfaces: Dynamics and interfacial rheology. *Advances in Colloid and Interface Science*, 206:303–319, 2014.
- [26] J. R. Samaniuk and J. Vermant. Micro and macrorheology at fluid-fluid interfaces. *Soft Matter*, 10(36):7023–7033, 2014.
- [27] W. Ramsden. Separation of Solids in the Surface-Layers of Solutions and 'Suspensions' (Observations on Surface-Membranes, Bubbles, Emulsions, and Mechanical Coagulation). – Preliminary Account. *Proceedings of the Royal Society of London*, 72(477-486):156–164, 1903.
- [28] S. U. Pickering. Emulsions. *Journal of the Chemical Society, Transactions*, 91:2001, 1907.
- [29] F. Bresme and M. Oettel. Nanoparticles at fluid interfaces. *Journal of Physics: Condensed Matter*, 19(41):413101, 2007.
- [30] P. Pieranski. Two-Dimensional Interfacial Colloidal Crystals. *Physical Review Letters*, 45(7):569–572, 1980.
- [31] S. Kinge, M. Crego-Calama, and D. N. Reinhoudt. Self-Assembling Nanoparticles at Surfaces and Interfaces. *ChemPhysChem*, 9(1):20–42, 2008.
- [32] Y. H. Lee, W. Shi, H. K. Lee, R. Jiang, I. Y. Phang, Y. Cui, L. Isa, Y. Yang, J. Wang, S. Li, and X. Y. Ling. Nanoscale surface chemistry directs the tunable assembly of silver octahedra into three two-dimensional plasmonic superlattices. *Nature Communications*, 6:6990, 2015.

- [33] H. A. Atwater and A. Polman. Plasmonics for improved photovoltaic devices. *Nature Materials*, 9(3):205–213, 2010.
- [34] Q. A. Pankhurst, J. Connolly, S. K. Jones, and J. Dobson. Applications of magnetic nanoparticles in biomedicine. *Journal of Physics D: Applied Physics*, 36(13):R167–R181, 2003.
- [35] G. Kaufman, S. Nejati, R. Sarfati, R. Boltyanskiy, M. Loewenberg, E. R. Dufresne, and C. O. Osuji. Soft microcapsules with highly plastic shells formed by interfacial polyelectrolyte-nanoparticle complexation. *Soft Matter*, 11(38):7478–7482, 2015.
- [36] A. Maestro, E. Guzmán, F. Ortega, and R. G. Rubio. Contact angle of micro- and nanoparticles at fluid interfaces. *Current Opinion in Colloid & Interface Science*, 19(4):355–367, 2014.
- [37] J. Israelachvili. *Intermolecular and Surface Forces*. Academic Press, 3rd edition. ISBN 978-0-12-391927-4, 2011.
- [38] M. Oettel and S. Dietrich. Colloidal Interactions at Fluid Interfaces. *Langmuir*, 24(4):1425–1441, 2008.
- [39] K. D. Danov and P. A. Kralchevsky. Capillary forces between particles at a liquid interface: general theoretical approach and interactions between capillary multipoles. *Advances in colloid and interface science*, 154(1-2):91–103, 2010.
- [40] B. J. Park, D. Lee, and E. M. Furst. Chapter 2. Interactions and Conformations of Particles at Fluid-Fluid Interfaces. In *Particle-Stabilized Emulsions and Colloids: Formation and Applications*, 3, chapter 2, pages 8–44. ISBN 978-1-84973-881-1, 2015.
- [41] D. Ershov, J. Sprakel, J. Appel, M. A. Cohen Stuart, and J. van der Gucht. Capillarity-induced ordering of spherical colloids on an interface with anisotropic curvature. *Proceedings of the National Academy of Sciences*, 110(23):9220–9224, 2013.
- [42] M. Grzelczak, J. Vermant, E. M. Furst, and L. M. Liz-Marzán. Directed Self-Assembly of Nanoparticles. *ACS Nano*, 4(7):3591–3605, 2010.
- [43] R. C. den Dulk, K. A. Schmidt, G. Sabatté, S. Liébana, and M. W. J. Prins. Magneto-capillary valve for integrated purification and enrichment of nucleic acids and proteins. *Lab Chip*, 13(1):106–118, 2013.
- [44] J. Eastoe and J. Dalton. Dynamic surface tension and adsorption mechanisms of surfactants at the air-water interface. *Advances in Colloid and Interface Science*, 85(2-3):103–144, 2000.
- [45] P. de Gennes. Polymers at an interface; a simplified view. *Advances in Colloid and Interface Science*, 27(3-4):189–209, 1987.
- [46] A. Maestro, H. M. Hilles, F. Ortega, R. G. Rubio, D. Langevin, and F. Monroy. Reptation in langmuir polymer monolayers. *Soft Matter*, 6(18):4407, 2010.
- [47] S. Barman and G. F. Christopher. Simultaneous Interfacial Rheology and Microstructure Measurement of Densely Aggregated Particle Laden Interfaces Using a Modified Double Wall Ring Interfacial Rheometer. *Langmuir*, 30(32):9752–9760, 2014.
- [48] O. S. Deshmukh, D. van den Ende, M. C. Stuart, F. Mugele, and M. H. Duits. Hard and soft colloids at fluid interfaces: Adsorption, interactions, assembly & rheology. *Advances in Colloid and Interface Science*, 222:215–227, 2015.
- [49] J. Berthier. Theory of Wetting. In *Micro-Drops and Digital Microfluidics*, pages 7–73. Elsevier. ISBN 978-0-8155-1544-9, 2008.

- [50] T. D. Blake. The physics of moving wetting lines. *Journal of colloid and interface science*, 299(1):1–13, 2006.
- [51] D. M. Kaz, R. McGorty, M. Mani, M. P. Brenner, and V. N. Manoharan. Physical ageing of the contact line on colloidal particles at liquid interfaces. *Nature materials*, 11(2):138–42, 2012.
- [52] L. Chen, L.-O. Heim, D. S. Golovko, and E. Bonaccorso. Snap-in dynamics of single particles to water drops. *Applied Physics Letters*, 101(3):031601, 2012.
- [53] J. van der Gucht, N. A. M. Besseling, W. Knoben, L. Bouteiller, and M. A. Cohen Stuart. Brownian particles in supramolecular polymer solutions. *Physical Review E*, 67(5):051106, 2003.
- [54] T. G. Mason and D. A. Weitz. Optical Measurements of Frequency-Dependent Linear Viscoelastic Moduli of Complex Fluids. *Physical Review Letters*, 74(7):1250–1253, 1995.
- [55] T. M. Squires and T. G. Mason. Fluid Mechanics of Microrheology. *Annual Review of Fluid Mechanics*, 42(1):413–438, 2010.
- [56] G. G. Fuller and J. Vermant. Complex Fluid-Fluid Interfaces: Rheology and Structure. *Annual Review of Chemical and Biomolecular Engineering*, 3(1):519–543, 2012.
- [57] P. Cicuta and A. M. Donald. Microrheology: a review of the method and applications. *Soft Matter*, 3(12):1449, 2007.
- [58] A. Maestro, L. J. Bonales, H. Ritacco, T. M. Fischer, R. G. Rubio, and F. Ortega. Surface rheology: macro- and microrheology of poly(tert-butyl acrylate) monolayers. *Soft Matter*, 7(17):7761, 2011.
- [59] M. H. Lee, S. P. Cardinali, D. H. Reich, K. J. Stebe, and R. L. Leheny. Brownian dynamics of colloidal probes during protein-layer formation at an oil-water interface. *Soft Matter*, 7(17):7635, 2011.
- [60] T. M. Squires and J. F. Brady. A simple paradigm for active and nonlinear microrheology. *Physics of Fluids*, 17(7):073101, 2005.
- [61] A. M. Puertas and T. Voigtmann. Microrheology of colloidal systems. *Journal of Physics: Condensed Matter*, 26(24):243101, 2014.
- [62] D. B. Allan, D. M. Firester, V. P. Allard, D. H. Reich, K. J. Stebe, and R. L. Leheny. Linear and nonlinear microrheology of lysozyme layers forming at the air-water interface. *Soft Matter*, 10(36):7051–7060, 2014.
- [63] A. Brasovs, J. Cīmurs, K. Ērglis, A. Zeltins, J.-F. Berret, and A. Cēbers. Magnetic microrods as a tool for microrheology. *Soft Matter*, 11(13):2563–2569, 2015.
- [64] S. Choi, S. Steltenkamp, J. Zasadzinski, and T. Squires. Active microrheology and simultaneous visualization of sheared phospholipid monolayers. *Nature Communications*, 2(May):312, 2011.
- [65] P. Dhar, Y. Cao, T. M. Fischer, and J. A. Zasadzinski. Active Interfacial Shear Microrheology of Aging Protein Films. *Physical Review Letters*, 104(1):016001, 2010.
- [66] M. H. Lee, D. H. Reich, K. J. Stebe, and R. L. Leheny. Combined Passive and Active Microrheology Study of Protein-Layer Formation at an Air-Water Interface. *Langmuir*, 26(4):2650–2658, 2010.

- [67] Z. A. Zell, A. Nowbahar, V. Mansard, L. G. Leal, S. S. Deshmukh, J. M. Mecca, C. J. Tucker, and T. M. Squires. Surface shear inviscidity of soluble surfactants. *Proceedings of the National Academy of Sciences*, 111(10):3677–3682, 2014.
- [68] K. Danov, R. Aust, F. Durst, and U. Lange. Influence of the Surface Viscosity on the Hydrodynamic Resistance and Surface Diffusivity of a Large Brownian Particle. *Journal of Colloid and Interface Science*, 175(1):36–45, 1995.
- [69] T. M. Fischer, P. Dhar, and P. Heinig. The viscous drag of spheres and filaments moving in membranes or monolayers. *Journal of Fluid Mechanics*, 558:451, 2006.
- [70] D. Stamou, C. Duschl, and D. Johannsmann. Long-range attraction between colloidal spheres at the air-water interface: The consequence of an irregular meniscus. *Physical Review E*, 62(4):5263–5272, 2000.
- [71] P. A. Kralchevsky and K. Nagayama. Capillary interactions between particles bound to interfaces, liquid films and biomembranes. *Advances in Colloid and Interface Science*, 85(2-3):145–192, 2000.
- [72] M. P. Boneva, N. C. Christov, K. D. Danov, and P. A. Kralchevsky. Effect of electric-field-induced capillary attraction on the motion of particles at an oil-water interface. *Physical Chemistry Chemical Physics*, 9(48):6371, 2007.
- [73] J. C. Loudet, A. M. Alsayed, J. Zhang, and A. G. Yodh. Capillary Interactions Between Anisotropic Colloidal Particles. *Physical Review Letters*, 94(1):018301, 2005.
- [74] L. Botto, E. P. Lewandowski, M. Cavallaro, and K. J. Stebe. Capillary interactions between anisotropic particles. *Soft Matter*, 8(39):9957, 2012.
- [75] G. B. Davies, T. Krüger, P. V. Coveney, J. Harting, and F. Bresme. Interface deformations affect the orientation transition of magnetic ellipsoidal particles adsorbed at fluid-fluid interfaces. *Soft Matter*, 10(35):6742, 2014.
- [76] G. B. Davies, T. Krüger, P. V. Coveney, J. Harting, and F. Bresme. Assembling Ellipsoidal Particles at Fluid Interfaces using Switchable Dipolar Capillary Interactions. *Advanced materials (Deerfield Beach, Fla.)*, pages 1–5, 2014.
- [77] K. D. Danov, P. A. Kralchevsky, B. N. Naydenov, and G. Brenn. Interactions between particles with an undulated contact line at a fluid interface: Capillary multipoles of arbitrary order. *Journal of Colloid and Interface Science*, 287(1):121–134, 2005.
- [78] B. Madivala, J. Franssaer, and J. Vermant. Self-Assembly and Rheology of Ellipsoidal Particles at Interfaces. *Langmuir*, 25(5):2718–2728, 2009.
- [79] M. Cavallaro, L. Botto, E. P. Lewandowski, M. Wang, and K. J. Stebe. Curvature-driven capillary migration and assembly of rod-like particles. *Proceedings of the National Academy of Sciences of the United States of America*, 108(52):20923–8, 2011.
- [80] R. Aveyard, B. P. Binks, J. H. Clint, P. D. I. Fletcher, T. S. Horozov, B. Neumann, V. N. Paunov, J. Annesley, S. W. Botchway, D. Nees, A. W. Parker, A. D. Ward, and A. N. Burgess. Measurement of Long-Range Repulsive Forces between Charged Particles at an Oil-Water Interface. *Physical Review Letters*, 88(24):246102, 2002.
- [81] K. C. Neuman and A. Nagy. Single-molecule force spectroscopy: optical tweezers, magnetic tweezers and atomic force microscopy. *Nature Methods*, 5(6):491–505, 2008.
- [82] B. J. Park and E. M. Furst. Attractive interactions between colloids at the oil-water interface. *Soft Matter*, 7(17):7676, 2011.

- [83] C. J. van Oss. *Interfacial Forces in Aqueous Media*. New York. ISBN 0824791681, 1994.
- [84] E. Bormashenko. Wetting of real solid surfaces: new glance on well-known problems. *Colloid and Polymer Science*, 291(2):339–342, 2012.
- [85] H. B. Eral, D. J. C. M. 't Mannetje, and J. M. Oh. Contact angle hysteresis: a review of fundamentals and applications. *Colloid and Polymer Science*, 291(2):247–260, 2012.
- [86] J. H. Snoeijer and B. Andreotti. Moving Contact Lines: Scales, Regimes, and Dynamical Transitions. *Annual Review of Fluid Mechanics*, 45(1):269–292, 2013.
- [87] J. C. Crocker and D. G. Grier. Methods of Digital Video Microscopy for Colloidal Studies. *Journal of Colloid and Interface Science*, 179(1):298–310, 1996.
- [88] M. Irmscher, A. M. de Jong, H. Kress, and M. W. J. Prins. Probing the Cell Membrane by Magnetic Particle Actuation and Euler Angle Tracking. *Biophysical Journal*, 102(3):698–708, 2012.
- [89] A. van Reenen, F. Gutiérrez-Mejía, L. J. van IJzendoorn, and M. W. J. Prins. Torsion Profiling of Proteins Using Magnetic Particles. *Biophysical Journal*, 104(5):1073–1080, 2013.
- [90] V. Garbin, J. C. Crocker, and K. J. Stebe. Nanoparticles at fluid interfaces: exploiting capping ligands to control adsorption, stability and dynamics. *Journal of colloid and interface science*, 387(1):1–11, 2012.
- [91] K. Stratford, R. Adhikari, I. Pagonabarraga, J.-C. Desplat, and M. E. Cates. Colloidal jamming at interfaces: a route to fluid-bicontinuous gels. *Science (New York, N.Y.)*, 309(5744):2198–201, 2005.
- [92] E. M. Herzig, K. A. White, A. B. Schofield, W. C. K. Poon, and P. S. Clegg. Bicontinuous emulsions stabilized solely by colloidal particles. *Nature materials*, 6(12):966–71, 2007.
- [93] M. N. Lee, J. H. J. Thijssen, J. A. Witt, P. S. Clegg, and A. Mohraz. Making a Robust Interfacial Scaffold: Bijel Rheology and its Link to Processability. *Advanced Functional Materials*, 23(4):417–423, 2013.
- [94] S. Cappelli, Q. Xie, J. Harting, A. M. de Jong, and M. W. J. Prins. Dynamic wetting: status and prospective of single particle based experiments and simulations. *New Biotechnology*, 32(5):420–432, 2015.
- [95] R. Giese, P. Costanzo, and C. Oss. The surface free energies of talc and pyrophyllite. *Physics and Chemistry of Minerals*, 17(7):611–616, 1991.
- [96] J. H. Clint and S. E. Taylor. Particle size and interparticle forces of overbased detergents: A Langmuir trough study. *Colloids and Surfaces*, 65(1):61–67, 1992.
- [97] N. Yan, Y. Maham, J. Masliyah, M. Gray, and A. Mather. Measurement of Contact Angles for Fumed Silica Nanospheres Using Enthalpy of Immersion Data. *Journal of colloid and interface science*, 228(1):1–6, 2000.
- [98] B. P. Binks, J. H. Clint, A. K. F. Dyab, P. D. I. Fletcher, M. Kirkland, and C. P. Whitby. Ellipsometric Study of Monodisperse Silica Particles at an Oil-Water Interface. *Langmuir*, 19(21):8888–8893, 2003.
- [99] A. Agod, A. Deák, E. Hild, Z. Hórvölgyi, E. Kálmán, G. Tolnai, and A. L. Kovács. Contact angle determination of nanoparticles: real experiments and computer simulations. *The Journal of Adhesion*, 80(10-11):1055–1072, 2004.
- [100] Z.-G. Cui, B. P. Binks, and J. H. Clint. Determination of contact angles on microporous particles using the thin-layer wicking technique. *Langmuir*, 21(18):8319–25, 2005.

- [101] J. Mingins and A. Scheludko. Attachment of spherical particles to the surface of a pendant drop and the tension of the wetting perimeter. *Journal of the Chemical Society, Faraday Transactions 1: Physical Chemistry in Condensed Phases*, 75:1, 1979.
- [102] Z. Hórvölgyi, S. Németh, and J. Fendler. Spreading of hydrophobic silica beads at water-air interfaces. *Colloids and Surfaces A: Physicochemical and Engineering Aspects*, 71(3):327–335, 1993.
- [103] A. Hadjiiski, R. Dimova, N. D. Denkov, I. B. Ivanov, and R. Borwankar. Film Trapping Technique: Precise Method for Three-Phase Contact Angle Determination of Solid and Fluid Particles of Micrometer Size. *Langmuir*, 12(26):6665–6675, 1996.
- [104] M. Preuss and H. Butt. Measuring the Contact Angle of Individual Colloidal Particles. *Journal of colloid and interface science*, 208(2):468–477, 1998.
- [105] V. N. Paunov. Novel Method for Determining the Three-Phase Contact Angle of Colloid Particles Adsorbed at Air-Water and Oil-Water Interfaces. *Langmuir*, 19(19):7970–7976, 2003.
- [106] R. Mohammadi and A. Amirfazli. Contact Angle Measurement for Dispersed Microspheres Using Scanning Confocal Microscopy. *Journal of Dispersion Science and Technology*, 25(5):567–574, 2005.
- [107] T. S. Horozov, D. A. Braz, P. D. I. Fletcher, B. P. Binks, and J. H. Clint. Novel film-calliper method of measuring the contact angle of colloidal particles at liquid interfaces. *Langmuir*, 24(5):1678–81, 2008.
- [108] L. Isa, F. Lucas, R. Wepf, and E. Reimhult. Measuring single-nanoparticle wetting properties by freeze-fracture shadow-casting cryo-scanning electron microscopy. *Nature communications*, 2:438, 2011.
- [109] N. Vogel, J. Ally, K. Bley, M. Kappl, K. Landfester, and C. K. Weiss. Direct visualization of the interfacial position of colloidal particles and their assemblies. *Nanoscale*, 6(12):6879–85, 2014.
- [110] A. Wang, D. M. Kaz, R. McGorty, and V. N. Manoharan. Relaxation dynamics of colloidal particles at liquid interfaces. 336:336–343, 2013.
- [111] H. Kusumaatmaja and J. M. Yeomans. Modeling contact angle hysteresis on chemically patterned and superhydrophobic surfaces. *Langmuir*, 23(11):6019–32, 2007.
- [112] J. Hyväluoma, A. Koponen, P. Raiskinmäki, and J. Timonen. Droplets on inclined rough surfaces. *The European physical journal. E, Soft matter*, 23(3):289–93, 2007.
- [113] C. Kunert, J. Harting, and O. I. Vinogradova. Random-Roughness Hydrodynamic Boundary Conditions. *Physical Review Letters*, 105(1):016001, 2010.
- [114] J. H. Weijjs, B. Andreotti, and J. H. Snoeijer. Elasto-capillarity at the nanoscale: on the coupling between elasticity and surface energy in soft solids. *Soft Matter*, 9(35):8494, 2013.
- [115] C. Cottin-Bizonne, C. Barentin, E. Charlaix, L. Bocquet, and J.-L. Barrat. Dynamics of simple liquids at heterogeneous surfaces: molecular-dynamics simulations and hydrodynamic description. *The European physical journal. E, Soft matter*, 15(4):427–38, 2004.
- [116] M. Cieplak, J. Koplik, and J. Banavar. Boundary Conditions at a Fluid-Solid Interface. *Physical Review Letters*, 86(5):803–806, 2001.

- [117] N. Priezjev, A. Darhuber, and S. Troian. Slip behavior in liquid films on surfaces of patterned wettability: Comparison between continuum and molecular dynamics simulations. *Physical Review E*, 71(4):041608, 2005.
- [118] M. Sbragaglia, R. Benzi, L. Biferale, S. Succi, and F. Toschi. Surface Roughness-Hydrophobicity Coupling in Microchannel and Nanochannel Flows. *Physical Review Letters*, 97(20):204503, 2006.
- [119] D. G. A. L. Aarts, M. Schmidt, and H. N. W. Lekkerkerker. Direct visual observation of thermal capillary waves. *Science (New York, N.Y.)*, 304(5672):847–50, 2004.
- [120] S. S. H. Tsai, J. S. Wexler, J. Wan, and H. A. Stone. Microfluidic ultralow interfacial tensiometry with magnetic particles. *Lab Chip*, 13(1):119–125, 2013.
- [121] J. H. Weijjs, A. Marchand, B. Andreotti, D. Lohse, and J. H. Snoeijer. Origin of line tension for a Lennard-Jones nanodroplet. *Physics of Fluids*, 23(2):022001, 2011.
- [122] S. Schmieschek and J. Harting. Contact Angle Determination in Multicomponent Lattice Boltzmann Simulations. *Communications in Computational Physics*, 9:1165–1178, 2011.
- [123] M. J. P. Nijmeijer, C. Bruin, A. B. van Woerkom, A. F. Bakker, and J. M. J. van Leeuwen. Molecular dynamics of the surface tension of a drop. *The Journal of Chemical Physics*, 96(1):565, 1992.
- [124] S. Frijters, F. Günther, and J. Harting. Effects of nanoparticles and surfactant on droplets in shear flow. *Soft Matter*, 8(24):6542, 2012.
- [125] H. Liu, Q. Kang, C. R. Leonardi, S. Schmieschek, A. Narváez, B. D. Jones, J. R. Williams, A. J. Valocchi, and J. Harting. Multiphase lattice Boltzmann simulations for porous media applications. *Computational Geosciences*, pages 1–51, 2015.
- [126] A. Marmur. Solid-Surface Characterization by Wetting. *Annual Review of Materials Research*, 39(1):473–489, 2009.
- [127] E. Bormashenko, Y. Bormashenko, G. Whyman, R. Pogreb, A. Musin, R. Jager, and Z. Barkay. Contact angle hysteresis on polymer substrates established with various experimental techniques, its interpretation, and quantitative characterization. *Langmuir*, 24(8):4020–5, 2008.
- [128] Y. Ba, H. Liu, J. Sun, and R. Zheng. Color-gradient lattice Boltzmann model for simulating droplet motion with contact-angle hysteresis. *Physical Review E*, 88(4):043306, 2013.
- [129] N. Moradi, F. Varnik, and I. Steinbach. Roughness-gradient-induced spontaneous motion of droplets on hydrophobic surfaces: A lattice Boltzmann study. *EPL (Europhysics Letters)*, 89(2):26006, 2010.
- [130] T. D. Blake, A. Clarke, J. De Coninck, and M. J. de Ruijter. Contact Angle Relaxation during Droplet Spreading: Comparison between Molecular Kinetic Theory and Molecular Dynamics. *Langmuir*, 13(7):2164–2166, 1997.
- [131] J. D. Halverson, C. Maldarelli, A. Couzis, and J. Koplik. A molecular dynamics study of the motion of a nanodroplet of pure liquid on a wetting gradient. *The Journal of chemical physics*, 129(16):164708, 2008.
- [132] T. Koishi, K. Yasuoka, S. Fujikawa, and X. C. Zeng. Measurement of contact-angle hysteresis for droplets on nanopillared surface and in the Cassie and Wenzel states: a molecular dynamics simulation study. *ACS nano*, 5(9):6834–42, 2011.

- [133] R. G. Cox. The dynamics of the spreading of liquids on a solid surface. Part 1. Viscous flow. *Journal of Fluid Mechanics*, 168(-1):169, 2006.
- [134] D. Duivivier, T. D. Blake, and J. De Coninck. Toward a predictive theory of wetting dynamics. *Langmuir*, 29(32):10132–40, 2013.
- [135] K. G. Winkels, J. H. Weijs, A. Eddi, and J. H. Snoeijer. Initial spreading of low-viscosity drops on partially wetting surfaces. *Physical Review E*, 85(5):055301, 2012.
- [136] H. Brenner. The slow motion of a sphere through a viscous fluid towards a plane surface. *Chemical Engineering Science*, 16(3-4):242–251, 1961.
- [137] E. Bart. The slow unsteady settling of a fluid sphere toward a flat fluid interface. *Chemical Engineering Science*, 23(3):193–210, 1968.
- [138] E. C. Mbamala and H. H. von Grünberg. Effective interaction of a charged colloidal particle with an air-water interface. *Journal of Physics: Condensed Matter*, 14(19):4881–4900, 2002.
- [139] M. Borkovec, I. Szilagyi, I. Popa, M. Finessi, P. Sinha, P. Maroni, and G. Papastavrou. Investigating forces between charged particles in the presence of oppositely charged polyelectrolytes with the multi-particle colloidal probe technique. *Advances in Colloid and Interface Science*, 179-182:85–98, 2012.
- [140] A. J. Hurd. The electrostatic interaction between interfacial colloidal particles. *Journal of Physics A: Mathematical and General*, 18(16):L1055–L1060, 1985.
- [141] H. Rezvantab and S. Shojaei-Zadeh. Capillary interactions between spherical Janus particles at liquid-fluid interfaces. *Soft Matter*, 9(13):3640, 2013.
- [142] Q. Xie, G. B. Davies, F. Günther, and J. Harting. Tunable dipolar capillary deformations for magnetic Janus particles at fluid-fluid interfaces. *Soft Matter*, 11(18):3581–3588, 2015.
- [143] N. Sharifi-Mood, I. B. Liu, and K. J. Stebe. Curvature capillary migration of microspheres. *Soft Matter*, 11(34):6768–6779, 2015.
- [144] K. D. Danov and P. A. Kralchevsky. Interaction between like-charged particles at a liquid interface: Electrostatic repulsion vs. electrocapillary attraction. *Journal of Colloid and Interface Science*, 345(2):505–514, 2010.
- [145] K. D. Danov, P. A. Kralchevsky, and M. P. Boneva. Electrodipping Force Acting on Solid Particles at a Fluid Interface. *Langmuir*, 20(15):6139–6151, 2004.
- [146] L. N. Arnaudov, O. J. Cayre, M. A. Cohen Stuart, S. D. Stoyanov, and V. N. Paunov. Measuring the three-phase contact angle of nanoparticles at fluid interfaces. *Physical chemistry chemical physics : PCCP*, 12(2):328–31, 2010.
- [147] J. Bleibel, S. Dietrich, A. Domínguez, and M. Oettel. Shock Waves in Capillary Collapse of Colloids: A Model System for Two-Dimensional Screened Newtonian Gravity. *Physical Review Letters*, 107(12):128302, 2011.
- [148] C. Zeng, F. Brau, B. Davidovitch, and A. D. Dinsmore. Capillary interactions among spherical particles at curved liquid interfaces. *Soft Matter*, 8(33):8582, 2012.
- [149] J. Guzowski, M. Tasinkevych, and S. Dietrich. Capillary interactions in Pickering emulsions. *Physical Review E*, 84(3):031401, 2011.
- [150] H. Lehle, E. Noruzifar, and M. Oettel. Ellipsoidal particles at fluid interfaces. *The European physical journal. E, Soft matter*, 26(1-2):151–60.

- [151] A. Maestro, L. J. Bonales, H. Ritacco, R. G. Rubio, and F. Ortega. Effect of the spreading solvent on the three-phase contact angle of microparticles attached at fluid interfaces. *Physical chemistry chemical physics : PCCP*, 12(42):14115–20, 2010.
- [152] S. Komura, Y. Hirose, and Y. Nonomura. Adsorption of colloidal particles to curved interfaces. *The Journal of chemical physics*, 124(24):241104, 2006.
- [153] J. de Graaf, M. Dijkstra, and R. van Roij. Adsorption trajectories and free-energy separatrixes for colloidal particles in contact with a liquid-liquid interface. *The Journal of chemical physics*, 132(16):164902, 2010.
- [154] K. Schwenke, L. Isa, and E. Del Gado. Assembly of nanoparticles at liquid interfaces: crowding and ordering. *Langmuir*, 30(11):3069–74, 2014.
- [155] F. Bresme and J. Faraudo. Orientational transitions of anisotropic nanoparticles at liquid-liquid interfaces. *Journal of Physics: Condensed Matter*, 19(37):375110, 2007.
- [156] B. J. Park and D. Lee. Equilibrium orientation of nonspherical Janus particles at fluid-fluid interfaces. *ACS nano*, 6(1):782–90, 2012.
- [157] A. Fortini. Clustering and gelation of hard spheres induced by the Pickering effect. *Physical Review E*, 85(4):040401, 2012.
- [158] Q. Ehlinger, L. Joly, and O. Pierre-Louis. Giant Slip at Liquid-Liquid Interfaces Using Hydrophobic Ball Bearings. *Physical Review Letters*, 110(10):104504, 2013.
- [159] Y. J. Choi and P. D. Anderson. Cahn-Hilliard modeling of particles suspended in two-phase flows. *International Journal for Numerical Methods in Fluids*, 69(5):995–1015, 2012.
- [160] S. Frijters and J. Harting. Self-assembled porous media from particle-stabilized emulsions. *arXiv:1408.2974 [cond-mat.soft]*, 2014.
- [161] F. Jansen and J. Harting. From bijels to Pickering emulsions: A lattice Boltzmann study. *Physical Review E*, 83(4):046707, 2011.
- [162] F. Günther, S. Frijters, and J. Harting. Timescales of emulsion formation caused by anisotropic particles. *Soft matter*, 10(27):4977–89, 2014.
- [163] E. G. Kim, K. Stratford, P. S. Clegg, and M. E. Cates. Field-induced breakup of emulsion droplets stabilized by colloidal particles. *Physical Review E*, 85(2):020403, 2012.
- [164] A. Joshi and Y. Sun. Multiphase lattice Boltzmann method for particle suspensions. *Physical Review E*, 79(6):066703, 2009.
- [165] J. Onishi, A. Kawasaki, Y. Chen, and H. Ohashi. Lattice Boltzmann simulation of capillary interactions among colloidal particles. *Computers & Mathematics with Applications*, 55(7):1541–1553, 2008.
- [166] F. Günther, F. Janoschek, S. Frijters, and J. Harting. Lattice Boltzmann simulations of anisotropic particles at liquid interfaces. *Computers & Fluids*, 80:184–189, 2013.
- [167] S. Razavi, I. Kretzschmar, J. Koplik, and C. E. Colosqui. Nanoparticles at liquid interfaces: rotational dynamics and angular locking. *The Journal of chemical physics*, 140(1):014904, 2014.
- [168] J. de Graaf, M. Dijkstra, and R. van Roij. Adsorption Trajectories and Free-Energy Separatrixes for Colloidal Particles in Contact with a Liquid-Liquid Interface. page 14, 2010.
- [169] G. B. Davies, T. Krüger, P. V. Coveney, and J. Harting. Detachment energies of spheroidal particles from fluid-fluid interfaces. *The Journal of Chemical Physics*, 141(15):154902, 2014.

- [170] A. S. Joshi and Y. Sun. Wetting dynamics and particle deposition for an evaporating colloidal drop: A lattice Boltzmann study. *Physical Review E*, 82(4):041401, 2010.
- [171] G. B. Davies, T. Krüger, P. V. Coveney, J. Harting, and F. Bresme. Interface deformations affect the orientation transition of magnetic ellipsoidal particles adsorbed at fluid-fluid interfaces. *Soft matter*, 10(35):6742–8, 2014.
- [172] C. E. Colosqui, J. F. Morris, and J. Koplik. Colloidal Adsorption at Fluid Interfaces: Regime Crossover from Fast Relaxation to Physical Aging. *Physical Review Letters*, 111(2):028302, 2013.
- [173] H. Kramers. Brownian motion in a field of force and the diffusion model of chemical reactions. *Physica*, 7(4):284–304, 1940.
- [174] G. Kaufman, R. Boltynskiy, S. Nejati, A. R. Thiam, M. Loewenberg, E. R. Dufresne, and C. O. Osuji. Single-step microfluidic fabrication of soft monodisperse polyelectrolyte microcapsules by interfacial complexation. *Lab on a Chip*, 14(18):3494, 2014.
- [175] V. P. Gilcreest, K. A. Dawson, and A. V. Gorelov. Adsorption kinetics of NIPAM-based polymers at the air-water interface as studied by pendant drop and bubble tensiometry. *Journal of Physical Chemistry B*, 110(43):21903–21910, 2006.
- [176] D. Graham and M. Phillips. Proteins at liquid interfaces. *Journal of Colloid and Interface Science*, 70(3):403–414, 1979.
- [177] C. Monteux. Adsorption of soluble polymers at liquid interfaces and in foams. *Comptes Rendus Physique*, 15(8-9):775–785, 2014.
- [178] A. Nelson, D. Wang, K. Koynov, and L. Isa. A multiscale approach to the adsorption of core-shell nanoparticles at fluid interfaces. *Soft Matter*, 11(1):118–129, 2015.
- [179] F. Ortega, H. Ritacco, and R. G. Rubio. Interfacial microrheology: Particle tracking and related techniques. *Current Opinion in Colloid & Interface Science*, 15(4):237–245, 2010.
- [180] V. Prasad, S. A. Koehler, and E. R. Weeks. Two-Particle Microrheology of Quasi-2D Viscous Systems. *Physical Review Letters*, 97(17):176001, 2006.
- [181] G. Pesce, A. C. De Luca, G. Rusciano, P. A. Netti, S. Fusco, and A. Sasso. Microrheology of complex fluids using optical tweezers: a comparison with macrorheological measurements. *Journal of Optics A: Pure and Applied Optics*, 11(3):034016, 2009.
- [182] A. Yao, M. Tassieri, M. Padgett, and J. Cooper. Microrheology with optical tweezers. *Lab on a Chip*, 9(17):2568, 2009.
- [183] L. G. Wilson and W. C. K. Poon. Small-world rheology: an introduction to probe-based active microrheology. *Physical Chemistry Chemical Physics*, 13(22):10617, 2011.
- [184] M. Tassieri, F. D. Giudice, E. J. Robertson, N. Jain, B. Fries, R. Wilson, A. Glidle, F. Greco, P. A. Netti, P. L. Maffettone, T. Bicanic, and J. M. Cooper. Microrheology with Optical Tweezers: Measuring the relative viscosity of solutions 'at a glance'. *Scientific Reports*, 5:8831, 2015.
- [185] D. Mizuno, D. A. Head, F. C. MacKintosh, and C. F. Schmidt. Active and Passive Microrheology in Equilibrium and Nonequilibrium Systems. *Macromolecules*, 41(19):7194–7202, 2008.
- [186] C. Y. Park, H. D. Ou-Yang, and M. W. Kim. Interface shear microrheometer with an optically driven oscillating probe particle. *Review of Scientific Instruments*, 82(9):094702, 2011.

- [187] R. Shlomovitz, A. A. Evans, T. Boatwright, M. Dennin, and A. J. Levine. Measurement of Monolayer Viscosity Using Noncontact Microrheology. *Physical Review Letters*, 110(13):137802, 2013.
- [188] C. Y. Park and M. W. Kim. Dynamic Mechanical Properties of a Polyelectrolyte Adsorbed Insoluble Lipid Monolayer at the Air-Water Interface. *The Journal of Physical Chemistry B*, 119(16):5315–5320, 2015.
- [189] A. van Reenen, Y. Gao, A. H. Bos, A. M. de Jong, M. A. Hulsen, J. M. J. den Toonder, and M. W. J. Prins. Accurate quantification of magnetic particle properties by intra-pair magnetophoresis for nanobiotechnology. *Applied Physics Letters*, 103(4):043704, 2013.
- [190] A. S. Sergeeva, D. A. Gorin, and D. V. Volodkin. Polyelectrolyte Microcapsule Arrays: Preparation and Biomedical Applications. *BioNanoScience*, 4(1):1–14, 2014.
- [191] D. Blair and E. R. Dufresne. The Matlab Particle Tracking Code Repository. <http://site.physics.georgetown.edu/matlab/index.html>.
- [192] V. Pelletier, N. Gal, P. Fournier, and M. L. Kilfoil. Microrheology of Microtubule Solutions and Actin-Microtubule Composite Networks. *Physical Review Letters*, 102(18):188303, 2009.
- [193] J. Liu, M. L. Gardel, K. Kroy, E. Frey, B. D. Hoffman, J. C. Crocker, A. R. Bausch, and D. A. Weitz. Microrheology Probes Length Scale Dependent Rheology. *Physical Review Letters*, 96(11):118104, 2006.
- [194] X. J. A. Janssen, A. J. Schellekens, K. van Ommering, L. J. van IJendoorn, and M. W. J. Prins. Controlled torque on superparamagnetic beads for functional biosensors. *Biosensors and Bioelectronics*, 24(7):1937–1941, 2009.
- [195] J. Leach, H. Mushfique, S. Keen, R. Di Leonardo, G. Ruocco, J. M. Cooper, and M. J. Padgett. Comparison of Faxén’s correction for a microsphere translating or rotating near a surface. *Physical Review E*, 79(2):026301, 2009.
- [196] N. Wise, T. Grob, K. Morten, I. Thompson, and S. Sheard. Magnetophoretic velocities of superparamagnetic particles, agglomerates and complexes. *Journal of Magnetism and Magnetic Materials*, 384:328–334, 2015.
- [197] B. A. Noskov. Dilational surface rheology of polymer and polymer/surfactant solutions. *Current Opinion in Colloid & Interface Science*, 15(4):229–236, 2010.
- [198] B. P. Binks, L. Isa, and A. T. Tyowua. Direct Measurement of Contact Angles of Silica Particles in Relation to Double Inversion of Pickering Emulsions. *Langmuir*, 29(16):4923–4927, 2013.
- [199] A. Dörr and S. Hardt. Drag and diffusion coefficients of a spherical particle attached to a fluid interface. *arXiv:1502.05488*, pages 1–11, 2015.
- [200] D. Wang, S. Yordanov, H. M. Paroor, A. Mukhopadhyay, C. Y. Li, H.-J. Butt, and K. Koynov. Probing Diffusion of Single Nanoparticles at Water-Oil Interfaces. *Small*, 7(24):3502–3507, 2011.
- [201] A. F. H. Ward and L. Tordai. Time-Dependence of Boundary Tensions of Solutions I. The Role of Diffusion in Time-Effects. *The Journal of Chemical Physics*, 14(7):453, 1946.
- [202] R. A. L. Jones and R. W. Richards. *Polymers at Surfaces and Interfaces*. Cambridge University Press, Cambridge. ISBN 9780511623196, 1984.

- [203] F. Monroy, L. R. Arriaga, and D. Langevin. Langmuir polymer films: recent results and new perspectives. *Physical Chemistry Chemical Physics*, 14(42):14450, 2012.
- [204] D. Langevin. Surface shear rheology of monolayers at the surface of water. *Advances in Colloid and Interface Science*, 207(1):121–130, 2014.
- [205] M. A. Ray, N. Shewmon, S. Bhawalkar, L. Jia, Y. Yang, and E. S. Daniels. Submicrometer Surface Patterning Using Interfacial Colloidal Particle Self-Assembly. *Langmuir*, 25(13):7265–7270, 2009.
- [206] Y. Lin, H. Skaff, A. Böker, a. D. Dinsmore, T. Emrick, and T. P. Russell. Ultrathin Cross-Linked Nanoparticle Membranes. *Journal of the American Chemical Society*, 125(42):12690–12691, 2003.
- [207] G. M. Whitesides. Self-Assembly at All Scales. *Science*, 295(5564):2418–2421, 2002.
- [208] S. C. Glotzer and M. J. Solomon. Anisotropy of building blocks and their assembly into complex structures. *Nature Materials*, 6(7):557–562, 2007.
- [209] R. Zwanzig and R. D. Mountain. High-Frequency Elastic Moduli of Simple Fluids. *The Journal of Chemical Physics*, 43(12):4464, 1965.
- [210] K. Masschaele, B. J. Park, E. M. Furst, J. Fransaer, and J. Vermant. Finite Ion-Size Effects Dominate the Interaction between Charged Colloidal Particles at an Oil-Water Interface. *Physical Review Letters*, 105(4):048303, 2010.
- [211] S. Reynaert, P. Moldenaers, and J. Vermant. Control over Colloidal Aggregation in Monolayers of Latex Particles at the Oil-Water Interface. *Langmuir*, 22(11):4936–4945, 2006.
- [212] B. J. Park, J. P. Pantina, E. M. Furst, M. Oettel, S. Reynaert, and J. Vermant. Direct Measurements of the Effects of Salt and Surfactant on Interaction Forces between Colloidal Particles at Water-Oil Interfaces. *Langmuir*, 24(5):1686–1694, 2008.
- [213] S. Cappelli, A. M. de Jong, J. Baudry, and M. W. J. Prins. Interfacial rheometry of polymer at a water-oil interface by intra-pair magnetophoresis. *Soft Matter*, 12(25):5551–5562, 2016.
- [214] P. S. Grassia, E. J. Hinch, and L. C. Nitsche. Computer simulations of Brownian motion of complex systems. *Journal of Fluid Mechanics*, 282(-1):373, 1995.
- [215] B. Dünweg and W. Paul. Brownian dynamics simulations without Gaussian random numbers. *International Journal of Modern Physics C*, 02(03):817–827, 1991.
- [216] D. L. Ermak and J. a. McCammon. Brownian dynamics with hydrodynamic interactions. *The Journal of Chemical Physics*, 69(4):1352, 1978.
- [217] S. H. Northrup, S. A. Allison, and J. A. McCammon. Brownian dynamics simulation of diffusion-influenced bimolecular reactions. *The Journal of Chemical Physics*, 80(4):1517, 1984.
- [218] W. Chen, S. Tan, Z. Huang, T.-K. Ng, W. T. Ford, and P. Tong. Measured long-ranged attractive interaction between charged polystyrene latex spheres at a water-air interface. *Physical Review E*, 74(2):021406, 2006.
- [219] M. Schlosshauer and D. Baker. Realistic protein-protein association rates from a simple diffusional model neglecting long-range interactions, free energy barriers, and landscape ruggedness. *Protein Science*, 13(6):1660–1669, 2004.
- [220] D. L. Freeman. The influence of diffusion on surface reaction kinetics. *The Journal of Chemical Physics*, 78(10):6002, 1983.

- [221] B. Gutiérrez-Medina, J. O. L. Andreasson, W. J. Greenleaf, A. Laporta, and S. M. Block. An optical apparatus for rotation and trapping. *Methods in enzymology*, 475:377–404, 2010.
- [222] D. J. Johnson, N. J. Miles, and N. Hilal. Quantification of particle-bubble interactions using atomic force microscopy: A review. *Advances in colloid and interface science*, 127(2):67–81, 2006.
- [223] R. S. King, H. W. Blanch, and J. M. Prausnitz. Molecular thermodynamics of aqueous two-phase systems for bioseparations. *AIChE Journal*, 34(10):1585–1594, 1988.
- [224] H. Tavana, a. Jovic, B. Mosadegh, Q. Y. Lee, X. Liu, K. E. Luker, G. D. Luker, S. J. Weiss, and S. Takayama. Nanolitre liquid patterning in aqueous environments for spatially defined reagent delivery to mammalian cells. *Nature materials*, 8(9):736–741, 2009.
- [225] P. P. Mondal and A. Diaspro. *Fundamentals of Fluorescence Microscopy*, volume 9789400775. Springer Netherlands, Dordrecht. ISBN 978-94-007-7544-2, 2014.
- [226] P.-Å. Albertsson. Chromatography and Partition of Cells and Cell Fragments. *Nature*, 177(4513):771–774, 1956.
- [227] P.-Å. Albertsson, A. Cajarville, D. E. Brooks, and F. Tjerneld. Partition of proteins in aqueous polymer two-phase systems and the effect of molecular weight of the polymer. *Biochimica et Biophysica Acta (BBA) - General Subjects*, 926(1):87–93, 1987.
- [228] Y. Liu, R. Lipowsky, and R. Dimova. Concentration Dependence of the Interfacial Tension for Aqueous Two-Phase Polymer Solutions of Dextran and Polyethylene Glycol. *Langmuir*, 28(8):3831–3839, 2012.

Publications

Journal articles

- S. Cappelli**, A.M. de Jong, J. Baudry, M.W.J. Prins, Inter-particle capillary forces at a fluid-fluid interface with strong polymer-induced ageing, *submitted*.
- S. Cappelli**, A.M. de Jong, J. Baudry, M.W.J. Prins, Interfacial rheometry of polymer at a water-oil interface by Intra-Pair Magnetophoresis, *Soft Matter*, 12(25):5551-5562, 2016.
- S. Cappelli**, Q.Xie, J. Harting, A.M. de Jong, M.W.J. Prins, Dynamic wetting: status and perspective of single particle based experiments and simulations, *New Biotechnology*, 32(5):420-432, 2015.

Oral presentations

- S. Cappelli**, A.M. de Jong, J. Baudry, M.W.J. Prins, Interfacial microrheometry and inter-particle capillary forces at a fluid-fluid interface by intra-pair magnetophoresis, *6th International Colloids Conference*, Berlin, Germany, 19-22 June 2016
- S. Cappelli**, A.M. de Jong, M.W.J. Prins, Interaction of particles with fluid-fluid interfaces quantified using magnetic tweezers, *UK Colloids 2014*, London, United Kingdom, 6-9 July 2014.
- S. Cappelli**, A.M. de Jong, M.W.J. Prins, Interaction of particles with liquid-liquid interfaces quantified using magnetic tweezers, *MicroNanoConference 2013*, Hotel and Congressentrum the ReeHorst, Ede, The Netherlands, 11-12 December 2013.

Poster presentations (selection)

- S. Cappelli**, A.M. de Jong, J. Baudry, M.W.J. Prins, Microrheology of polymers at a fluid-fluid interface, *NanoCity 2015*, Amersfoort, The Netherlands, 5-6 October 2015 .
- S. Cappelli**, A.M. de Jong, J. Baudry, M.W.J. Prins, Interfacial rheometry of polymer at a water-oil interface by intra-pair magnetophoresis, *Annual Dutch meeting on Molecular and Cellular Biophysics*, Veldhoven, The Netherlands, 28-29 September 2015.
- S. Cappelli**, A.M. de Jong, M.W.J. Prins, Interaction between particles and liquid-liquid

interfaces studied using magnetic tweezers, *Novel Technologies for In-vitro Diagnostics (DIATECH 2014) International Conference*, Leuven, Belgium, 6-8 October 2014.

S. Cappelli, A.M.de Jong, M.W.J. Prins, Interaction between particles and liquid-liquid interfaces studied using magnetic tweezers, *Annual Dutch meeting on Molecular and Cellular Biophysics*, Veldhoven, The Netherlands, 29-30 September 2014.

S. Cappelli, A.M. de Jong, M.W.J. Prins, The interaction between particles and liquid-liquid interfaces studied using magnetic tweezers, *International Soft Matter conference 2013*, Rome, Italy, September 15-19.

R.C. den Dulk, **S. Cappelli**, K.A. Schmidt, G. Sabatte, S. Liebana, M.W.J. Prins, Magneto-capillary valve for integrated purification and enrichment of nucleic acids and proteins, *NanoBioTech-Montreux 2012 conference*, Montreux, Switzerland, 12-14 November 2012.

R.C. den Dulk, K.A. Schmidt, **S. Cappelli**, A.M. de Jong, M.W.J. Prins, Magneto-capillary valve for integrated biological sample preparation using magnetic microcarriers, *9th International Conference on the Scientific and Clinical Applications of Magnetic Carriers*, Minnesota, Minneapolis, USA, 22 - 26 May 2012.

Curriculum Vitae

Stefano Cappelli was born in Ravenna, Italy on the 8th of October, 1984. After finishing secondary school (Liceo Scientifico A. Oriani, Ravenna, Italy) in 2003, he went on to study Applied Physics at the University of Bologna and received his MSc degree with the highest honours ('cum laude') in Physics in 2011. He graduated under the supervision of Dr. Giuseppe Baldazzi and worked on the development and characterization of a Compton camera with innovative detectors for nuclear medicine and astrophysical applications.

In November 2011, he started working as a PhD student in the group Molecular Biosensors for Medical Diagnostics (MBx) at the Applied Physics department of Eindhoven University of Technology, The Netherlands. Under the supervision of Dr. Arthur de Jong and Prof. Menno Prins he conducted research work in the area of colloids and fluid-fluid interfaces, relevant for soft-matter materials and lab-on-a-chip biosensing technologies. His PhD work has been performed as a part of the BioMaX framework, a Marie Curie ITN (Initial Training Networks) project which aims to train the next generation of biomolecular researchers in the emerging field of new integrated molecular diagnostics for point-of-care testing. In 2013 he received the Onderwijsprijs from the student education organization (STOOR) as best supervisor for second year bachelor students. This thesis summarizes the main results of his work.

Acknowledgements

This very long journey has finally come to an end. I could not get through this odyssey without the help and support of many people. Finally, I can take this opportunity to express my gratitude to them.

First and foremost, I am deeply grateful to my supervisors, Menno and Arthur. Menno, thank you for giving me the opportunity to pursue my PhD in your group. I still remember that hot summer you called me by phone. You told me that this was going to be a hard challenge and that I would have to learn a lot of new things missing in my background. You were damn right! Arthur, Menno, thank you for guiding me through this path, always pushing me one step further, always with a positive outlook and passion, even when nothing was working. In these years you taught me so much and made me the scientist I am now. And thanks for being close and supportive, also in difficult times of my life. I will always look up to you, both as researchers and supervisors.

I would like to express my sincere gratitude to Jasper van der Gucht, Ilja Voets, Jens Harting and Jean Baudry for agreeing to be part of this committee and for evaluating and commenting this thesis. Jean, thank you for giving me the opportunity to visit your group. Jean, Jens, thanks for the fruitful collaboration of these years.

I'm particularly grateful to my former supervisor Giuseppe Baldazzi. Thank you Beppe for believing in me, you have been a source of inspiration, you gave me your passion and your perseverance to strive for success, despite all the obstacles.

During these years I found in the MBx group a wonderful place to work, full of smart and funny people, to which I owe this success, with all your help, your critical input and most importantly a lot of fun. Thank you Leo for the nice discussions about science and life. Thanks to the old glories of the group, Peter, Claudia, Emiel, Michael, Fabiola, Roland for all these wonderful years; thanks to all the new soon-to-be glories of the group, Christian, Max, Yuyang, Arpita, Matej and Adam, I hope you'll enjoy these years as I did. And thanks to the past glories of the group, Marjin, Loes, Matthias, Alexander, Konrad and Denis. Thank you Alexander for helping me getting started with my setup. Thank you Matthias for all the help you gave me. Konrad, Denis, despite the distance, it's always amazing to see each other. Thanks to all the students I supervised, Aart, Anne and Leroy, I hope you learned as much as I did from you.

Thanks to all the people from BioMaX, it was just amazing to meet you.

During these years I met a lot of wonderful people that made my stay in The Netherlands wonderful. Fabio, Gianmarco, you have been great house mates. Veronica, Luca,

thanks for these years. Thanks to the crazy group of Monkers, Michele, Irene, Sandra, Daniele, Jon, Ludovica, Federico, Simone and Alessandro. I couldn't get through the last stage of this PhD without you, releasing the stress with a good climb and having fun with a pizza at 21:59. Daniele, thanks for pushing me to get one step higher. Alessandro, thanks for all these years, from Hajraa to Monk, you have been and you are a great friend. Federico, Simone, what can I say of you...one very meticulous and organized, another one completely a mess, and wonderful together...your life! Valentina, you have always been there, I will remember all of our discussions, sharing our struggling about publications and the tough life of a PhD student. And most of all, as the good friend you are. Thanks for standing besides me in this very important day. Fabiola, we started this path together, how many times we shared the office late in the evenings, but finally we got it. Thanks for these amazing years and for standing besides me today (soon it will be your turn!). Prometheus, I still remember that first day, you were the first person I met here. We spent so much time together with a lot of good fun. You have been a great friend and house mate, although it took me several months to handle your crazy lamb! I will miss all these wonderful people that made me feel at home.

Thanks to all that group of crazy guys in Ravenna, that despite the distance you were close to me and made me miss home. Gigi, Maio, you were always there and ready to party. And Mazza, whenever you need a mate to see an amazing sunrise on the sea, count on me. A special thanks to the other group of crazy and wild animals from Sottomarino, Juri, Stefano, Erik, Giovanna, Ginger and Matteo, my happy island for a summer break and my second home. Raffa and Matteo, thanks for visiting me and for the greatest honour you could give me. I wish you all the happiness of this world! Ginger...you are just over the top! Pippio, a scassari! Thanks to my dearest friends, Max, Beltra and Davide. Donna volant, pericolo costante, amici manent. It was amazing to gather together after all these years, and it will be always like this, no matter how far we are. Thanks to Gevals, you always welcome me and it was so much fun to play with you. Max and Alice, thanks for coming to visit me several times. I'm proud of the choice you made, it takes a lot of courage to look for your happiness. I'm sure you will find it and I will come to visit you!

A special thanks to the people in Luxembourg. Andre, boia deh! Cusu, Robi, Sara, Simon, Maria Pia, Piero, tanta roba!!!

Mamma, Babbo, grazie per avere sempre creduto in me, per avermi dato la possibilità di seguire i miei sogni e raggiungere questo importantissimo traguardo. Questo é anche un vostro successo.

The list is still long, so I thank all the people that directly or indirectly helped me during these years. But before closing, I still have two very special thanks. The first one is for a group among the most amazing people I ever met in my life, Matteo, Filo, Juri and Marco², the Loggione. We spent together more than half of our life. You are amongst the smartest people I ever met and the dearest friends one could hope for, and a source of inspiration. No matter in which part of the world, you are always there. You are brothers to me.

The last thank is for Francesca. You have been always there. You supported me through all these years, and this success is also yours. I couldn't be more lucky and I'm proud to have you by my side, looking together for our future.